ISSN 2074-272X

науково-практичний журнал 2019/2

Електротехніка і Електромеханіка

Electrical Engineering & Electromechanics

Електротехніка. Визначні події. Славетні імена
Електричні машини та апарати
Електротехнічні комплекси та системи. Силова електроніка
Теоретична електротехніка та електрофізика
Техніка сильних електричних та магнітних полів. Кабельна техніка
Електричні станції, мережі і системи
Безпека електрообладнання
Ювілеї

З 2015 р. журнал індексується у міжнародній наукометричній базі Web of Science Core Collection: Emerging Sources Citation Index

«ELECTRICAL ENGINEERING & ELECTROMECHANICS»

SCIENTIFIC & PRACTICAL JOURNAL
Journal was founded in 2002
Founders:
National Technical University «Kharkiv Polytechnic Institute» (Kharkiv, Ukraine)
State Institution «Institute of Technical Problems of Magnetism of the NAS of Ukraine» (Kharkiv, Ukraine)

ISSUE 2/2019

TABLE OF CONTENTS

Editorial office address: Dept. of Electrical Apparatus, NTU «KhPI», Kyrpychova Str., 2, Kharkiv, 61002, Ukraine
phones: +380 57 7076281, +380 67 3594696, **e-mail:** a.m.grechko@gmail.com (**Grechko O.M.)**

ISSN (print) 2074-272X
ISSN (online) 2309-3404

Printed 17 April 2019. Format 60 x 90 ⅛. Paper – offset. Laser printing. Edition 200 copies.
Printed by Printing house «Madrid Ltd» (11, Maksymilianivska Str., Kharkiv, 61024, Ukraine)

UDC 629.7:930.1 **doi: 10.20998/2074-272X.2019.2.01**

M.I. Baranov

AN ANTHOLOGY OF THE DISTINGUISHED ACHIEVEMENTS IN SCIENCE AND TECHNIQUE. PART 48: AIRCRAFT DESIGNER ANDREY TUPOLEV AND HIS ACCOMPLISHMENTS IN AIRPLANE DESIGN

Purpose. ***Preparation of a short scientifically-historical essay about one of founders of world airplane design, prominent Soviet aircraft designer A.N. Tupolev.*** ***Methodology.*** ***Known scientific methods of collection, analysis and analytical treatment of scientific and technical information regarding becoming and development of Soviet and world aviation and resulted in scientific monographs, journals and internet-reports.*** ***Results.*** ***A short scientifically-historical essay is presented about a prominent Soviet aircraft designer Andrey Nikolaevich Tupolev, becoming in the 20th century one of founders of Soviet and world aviation. Basic scientific and technical achievements of A.N. Tupolev indicated in area of airplane design, bringing Soviet military and civil aviation around to extraordinary world heights. Basic tactical and technical descriptions are described regarding created under his scientific and technical guidance of such known types of civil airplanes as ANT-25, Tu-104, Tu-134, Tu-154 and Tu-114, and also military airplanes of type Tu-2, Tu-16 and Tu-95. Short information is resulted about flying descriptions of the modern Russian supersonic strategic bomber of type Tu-160, created in 1980-th in the design bureau name after A.N. Tupolev. It is marked that under guidance of A.N. Tupolev over 100 types of airplanes of the military and civil setting were developed in the former USSR, 70 from which are produced by aviation industry of country serially. It is indicated that Doctor of Technical Sciences, Academician of the Academy of Sciences of the USSR, Colonel-General-Engineer A.N. Tupolev was a founder known in the world of aviation scientific school, preparing many famous Russian aircraft designers. Information, touching handed him domestic and foreign governmental rewards and other authoritative signs of confession of prominent merits of great aircraft designer A.N. Tupolev world scientific and technical public is resulted in airplane design.*** ***Originality.*** ***Certain systematization is executed known from scientific publications and other scientific and technical materials media regarding becoming and development of Soviet and world aviation and considerable scientific and technical contribution to the military and civil airplane design of prominent Soviet aircraft designer A.N. Tupolev.*** ***Practical value.*** ***Scientific popularization and deepening for the students of higher schools, engineering, technical and scientific workers of scientific and technical knowledge in the field of history of becoming and development of Soviet and world airplane design, extending their scientific and technical range of interests and further development of scientific and technical progress in society.*** References 15, figures 12.

Key words: **aviation, prominent Soviet aircraft designer Andrey Tupolev, his basic achievements in airplane construction, scientifically-historical essay.**

Наведено короткий науково-історичний нарис про видатного радянського авіаконструктора Андрія Миколайовича Туполєва, що став одним з основоположників світового літакобудування. Описані основні науково-технічні досягнення А.М. Туполєва в галузі літакобудування, що привели радянську військову і цивільну авіацію на небачені світові висоти. Показано, що А.М. Туполєв є засновником відомої в світі авіаційної наукової школи, що виховала багато видних в колишньому СРСР авіаконструкторів. Під керівництвом великого авіаконструктора 20-го сторіччя А.М. Туполєва в СРСР було розроблено понад 100 типів літаків військового і цивільного призначення, 70 з яких виготовлялися авіаційною промисловістю країни серійно. Бібл. 15, рис. 12.

Ключові слова: **авіація, видатний радянський авіаконструктор Андрій Туполєв, його основні досягнення в літакобудуванні, науково-історичний нарис.**

Приведен краткий научно-исторический очерк о выдающемся советском авиаконструкторе Андрее Николаевиче Туполеве, ставшем одним из основоположников мирового самолетостроения. Описаны основные научно-технические достижения А.Н. Туполева в области самолетостроения, приведшие советскую военную и гражданскую авиацию на невиданные мировые высоты. Показано, что А.Н. Туполев является основателем известной в мире авиационной научной школы, воспитавшей многих видных в бывшем СССР авиаконструкторов. Под руководством великого авиаконструктора 20-го столетия А.Н. Туполева в СССР было разработано свыше 100 типов самолетов военного и гражданского назначения, 70 из которых изготавливались авиационной промышленностью страны серийно. Библ. 15, рис. 12.

Ключевые слова: **авиация, выдающийся советский авиаконструктор Андрей Туполев, его основные достижения в самолетостроении, научно-исторический очерк.**

Introduction. One of the pioneers of the Soviet helicopter industry, Academician of the Academy of Sciences of the USSR Boris Nikolayevich Yuriev believed [1]: «*... Studying the history of science and technology contributes to the development of engineers and scientists who get a broad view of the development of creative thought*». Applying this wise scientific position to such a high-tech and important area of modern engineering as aircraft design, let us turn to the outstanding scientific and technical achievements of one of the founders of world aviation, the famous Soviet aircraft designer, Academician of the Academy of Sciences of the USSR (since 1953) Andrey Nikolaevich Tupolev (Fig. 1) which worked in aircraft engineering almost at the same time as the outstanding Ukrainian-American aircraft designer I.I. Sikorsky [2].

The goal of the paper is preparation of a brief scientific and historical essay on one of the founders of the world aircraft design, an outstanding Soviet aircraft designer A.N. Tupolev.

1. The beginning of the life and career of A.N. Tupolev. He was born on November 10, 1888 in the Russian Empire (village of Pustomazovo, Tver province) in the family of a Russian provincial notary Nikolay Ivanovich Tupolev, who came from Siberian Cossacks

Fig. 1. Outstanding Soviet aircraft designer, three times Hero of Labor, Doctor of Technical Sciences, Academician of the Academy of Sciences of the USSR Andrey Nikolaevich Tupolev (November 10, 1888 - December 23, 1972) [3]

and studied law at St. Petersburg University (after the murder by the revolutionary populists of Tsar Alexander II he was expelled from St. Petersburg) [3]. According to his mother Anna Vasilyevna (nee Lisitsyna, who graduated from the Mariinsky Women Gymnasium in the city of Tver) he was by descent from the nobility. After graduating from the Tver gymnasium, Andrey Tupolev, showing interest in exact sciences and technology, in 1908 entered the Imperial Moscow Technical School (IMTS), which in Soviet times was called the N.E. Bauman Moscow Higher Technical School (MHTS) [3]. Later, he mentally recalled about the years of his youth [4, 5]: «*... We lived modestly. I had older brothers Sergey and Nikolay, and also sisters Natalya, Tatyana, Vera and Maria. Mother gave us all her strength, her whole soul. Our family was very big and friendly. Not patriarchal, but undoubtedly advanced*. « From October 1909, Professor Nikolay Zhukovsky, a famous Russian scientist, began to deliver lectures on aeronautics at IMTS. The acquaintance of Andrey Tupolev with N.Ye. Zhukovsky in the Aeronautical group at IMTS turned out to be fateful for him. According to A.N. Tupolev [5]: «*... From this moment on, my aviation life began*.» He quickly became one of N.Ye. Zhukovsky's active student, showing the ability of both the scientific researcher and aircraft designer. Because of the denunciation to the tsar police by the unknown person about his political unreliability in 1911, he had to leave IMTS for several years. Despite all the difficulties, in 1918 he defended with honor his diploma project at IMTS on the topic «*Experience of creating a hydroplane according to wind tunnel tests*» and became a mechanical engineer [5]. After completing his studies, he was hired as a teacher at IMTS. In the period 1919-1920 A.N. Tupolev gave lectures to students of IMTS on «Fundamentals of aerodynamic calculation», «Theories of airplanes» and «Theory of hydroplanes». He then went to work at the Central Aero-Hydrodynamic Institute (CAHI), which was headed by N.Ye. Zhukovsky. Here he took the position of Head of the Aviation Department, in which new Russian aircraft were investigated, developed and tested. In 1924, successful flight tests of the first in the USSR all-metal aircraft of type ANT-2 (Fig. 2), developed under the guidance of A.N. Tupolev [5] were carried out.

Fig. 2. One of the first all-metal Soviet propeller-piston aircrafts of type ANT-2 designed by the young aircraft designer A.N. Tupolev (1924) [5]

Thus, step by step, in CAHI, production and design teams were formed, aimed at creating in the USSR a new aviation technology, which the army and society as a whole needed.

2. The main achievements of the aircraft designer A.N. Tupolev in aircraft industry. A characteristic feature in the work of AN. Tupolev was that, relying on the personal experience of the aircraft designer, he included in his aircraft projects only the minimum amount of new, not sufficiently proven in flight work. In his design activities, he unswervingly used the principle of sequential aircraft design [5], according to which new aircraft designs were based on previously well-developed versions of aircraft designs in the «metal». With this approach, he ensured the reliability of the aircraft designs developed by him.

It is believed that one of the famous Soviet aircraft is an all-metal single-engine aircraft of type ANT-25 (Fig. 3) [5, 6]. The main designers of it were A.N. Tupolev and future outstanding Russian aircraft designer Pavel Osipovich Sukhoi (1933). This aircraft was intended to set world records in the USSR for a non-stop flight. The main tactical and technical characteristics of the aircraft of type ANT-25 [5]: flight range – 13000 km; ceiling (height) of air lift – 7850 m; maximum flight speed at an altitude – 246 km/h; maximum take-off weight – 11,500 kg; take-off weight without cargo – 4200 kg; wingspan – 34 m; wing area – 88.2 m^2; one piston engine of the ПД1-М34Р brand with a power of 900 hp; crew – 3 people. On this type of aircraft in 1936-1937 legendary non-stop air flights were made by the famous Soviet flight crew of V. Chkalov, G. Baidukov and A. Belyakov on the record long-distance routes Moscow – Franz-Joseph Land – Petropavlovsk-on-Kamchatka and Moscow – Portsland (USA) via the North Pole [5].

In the period 1922-1936 A.N. Tupolev as the chief designer of the CAHI Design Bureau for the design and production of all-metal aircrafts of various classes, was one of the founders of the CAHI scientific and technical base. In 1937, the aircraft designer A.N. Tupolev, due to contrived reasons of that cruel time (because of the accusation of sabotage and espionage in favor of France), was suspended from work at the CAHI Design Bureau and was unreasonably arrested. This was followed by the verdict of the Military Collegium of the Supreme Court of the USSR – deprivation of liberty for 15 years with a defeat for 5 years [3]. While in prison, he worked in a special Central Design Bureau-29 of the NKVD of the USSR (later this design bureau was called «Tupolevskaya Sharaga»). It is surprising that here A.N. Tupolev and his

design team was created one of the best in the period of the Second World War front-line bombers of the Tu-2 type (Fig. 4) [3].

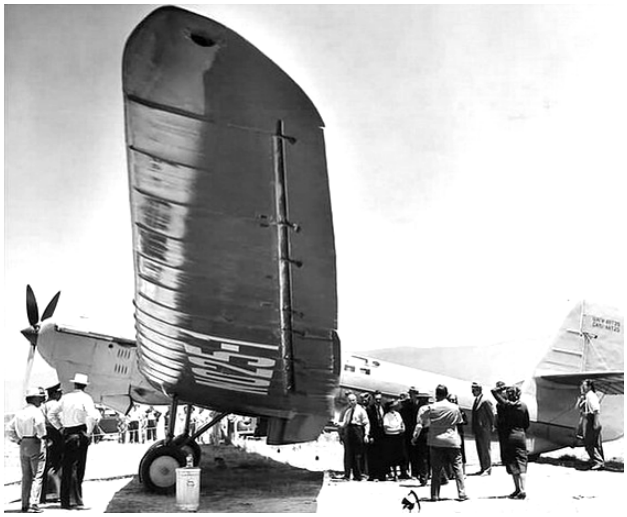

Fig. 3. Soviet screw single-engine long-range (record) aircraft ANT-25 developed by CAHI aircraft designers A.N. Tupolev and P.O. Sukhoi, in the USA (1937) [5]

Fig. 4. Soviet propeller twin-engine front dive bomber of Tu-2 type developed by A.N. Tupolev in the prison Central Design Bureau-29 of the NKVD of the USSR (1941) [5]

The main tactical and technical characteristics of the aircraft of type Tu-2 with two-tail unit [5]: flight range – 2020 km; maximum take-off weight – 11767 kg; take-off weight without combat cargo – 7601 kg; maximum flight speed at an altitude – 521 km/h; two piston air-cooled engines, brand АШ-82, with a power of 1,700 hp; lifting ceiling (height) – 9000 m; length – 14 m; crew – 3 people Tu-2 type front bomber made the first flight on January 29, 1941. The serial production of this aircraft began in 1942 and lasted until 1952. A total of 2649 units of this bomber were manufactured in the USSR [5]. This plane was one of the best machines of its time.

The first Soviet post-war carrier of nuclear weapons was a propeller piston four-engine strategic bomber of the Tu-4 type (1947), which was an exact copy of the American B-29 type bomber, from which the United States on the 6th and the 9th of August 1945 dropped on the Japanese cities of Hiroshima and Nagasaki, respectively, uranium and plutonium atomic bombs [5, 7]. By the end of the 1940s, it became clear to Soviet aircraft designers that the future of long-range bomber aircraft would belong to aircrafts with turboprop and turbojet engines. In this regard, for A.N. Tupolev and his Design Bureau the most important task of the urgent creation of a Soviet long-range missile carrier bomber was formulated by the directive bodies of the USSR. In 1953, this task was completed. In the USSR, the first jet strategic bomber of the Tu-16 type appeared (Fig. 5) [5, 6].

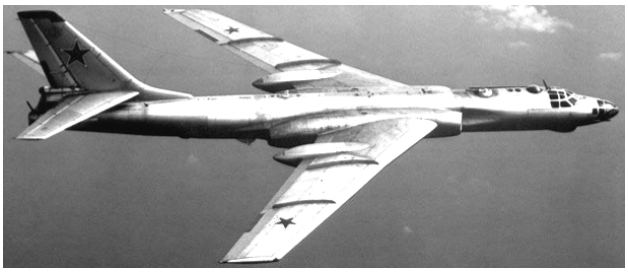

Fig. 5. Soviet jet twin-engine long-range missile-carrier bomber of the Tu-16 type («Russian badger» in the terminology of NATO countries) developed by A.N. Tupolev (1953, chief designer of the machine – D.S. Markov) [5]

Its creation is an unusual phenomenon not only in the Soviet, but also in the global aircraft industry. Combat aircrafts of the Tu-16 type with a minimum of operational modifications were used by the air forces of the USSR and Russia until 1994. They became one of the most «long-lived» military aircrafts in Soviet aviation. This was due to the exceptional reliability of their design and on-board equipment [9]. By the way, electrical equipment on Tu-16 aircraft was built using a single-wire circuit with a common «minus» on a metal case (board) made of a new at the time lightweight and durable Д16Т duralumin alloy. Four generators of the ГСР-18000 type (two for each engine) and two lead-acid batteries of the 12САМ-55 type (each battery consisted of two 6САМ-55 batteries connected in series) were used as DC sources. The plane used an electrical network with a voltage of 115 V and a frequency of 400 Hz, powered by two electric machine transducers of the ПО-4500 type [9]. It should be noted that in addition to these current sources, various electric power converters were additionally installed on various modifications of the Tu-16 to power the additional equipment installed on board. The combat aircraft of the Tu-16 type became a real pioneer in the class of heavy jet aircraft for Soviet aviation science. Only an American strategic bomber of type B-52 and a Soviet strategic bomber of type Tu-95, which will be discussed a little below, can be compared with it in terms of «longevity». Within 40 years of its combat «service», about 50 modifications of the Tu-16 type aircraft were created [9]. Its power plant contained two turbojet engines of the РД-3М brand with a thrust of 9,500 kgf each. The main tactical and technical characteristics of the aircraft Tu-16 [9]: flight range – 6350 km; maximum take-off weight – 79,000 kg; mass without fuel and cargo – 37,200 kg; maximum flight speed at an altitude – 1050 km / h; lifting ceiling (height) – 12,300 m; length – 34.8 m; wingspan – 33 m; wing area – 164.6 m^2; maximum fuel mass – 36,000 kg; crew – 6 people. According to its technical characteristics and layout, the Tu-16 combat aircraft was so successful that it allowed A.N. Tupolev and his Design Bureau without any problems, in a short time, create on its basis the first Soviet passenger jet airliner of the Tu-104 type (Fig. 6) [6, 9, 10].

Fig. 6. One of the first in the world Soviet jet multi-passenger aircraft of the Tu-104 type («Russian camel» in the terminology of the NATO countries) developed by A.N. Tupolev (1956) based on a Tu-16 type combat aircraft [6]

On July 17, 1955, the test pilot Yu. Alasheev lifted into the air a prototype of a civilian Tu-104 aircraft, and from next year the USSR began mass production of this machine at the Kharkiv aircraft factory [10]. In 1956, the USSR, thanks to the creation of a Tu-104 type aircraft, managed to hit the western world when, during the visit of its leader N.S. Khrushchev to England last with a government delegation flew to London on this airliner. The main tactical and technical characteristics of the aircraft Tu-104 with two turbojet engines AM-3 (with a load of 8750 kgf) [10]: maximum take-off weight – 74,500 kg; empty machine weight – 42,800 kg; payload – 9,000 kg; fuel reserve – 26,500 kg; maximum range with a commercial load – 2,120 km; maximum flight speed at an altitude – 950 km/h; lifting ceiling (height) – 11,500 m; the number of passengers on board – 50-110; length – 38.9 m; wingspan – 34.5 m; wing area – 174.4 m^2; crew – 5 people. The onboard equipment of the Tu-104 passenger aircraft was in many respects similar to the equipment of the Tu-16 combat aircraft. It consisted of [10]: autopilot АП-5-2 or АП-6; variometer ВАР-30-3; altimeter ВД-20; speed indicator КУС-1200; radio altimeter РВ-2; astrocompass АК-49; short-range radio navigation system РСБН-2; airborne radar РБП-4Г; radio compass АРК-5; gyrohalfcompas ГПК-52; remote gyromagnetic compass ДГМК-7; course-glide path system СП-50 «Mainland», course-glide path system ИЛС (course radio receiver КРП-Ф, glissad radio receiver ГРП-2, marker radio receiver МРП-48 or МРП-56П); communication radio station (receiver УС-9, transmitter 1-РСБ-70).

The appearance of the passenger plane Tu-104 allowed the USSR to reach the international level of air transportation as soon as possible. Aeroflot, a civilian user, carried international and domestic medium-haul flights on it. The operation of the Tu-104 type aircraft by Aeroflot was completed in December 1979. The experience of creating this passenger aircraft was used by A.N. Tupolev and his Design Bureau when designing a new Soviet airliner of the Tu-134 type (Fig. 7) [10].

The mid-range passenger aircraft of the Tu-134 type was a very successful long-lived airliner, which operates in Russia from 1967 to the present day (more than 50 years!) [10]. Note that before the creation of the Tu-134 A.N. Tupolev, appointed in 1956 as the General Designer of the Design Bureau-156 of the Ministry of Aviation Industry of the USSR, developed short-haul jet passenger aircrafts such as the Tu-110 (1957) and Tu-124 (1960), as well as a supersonic jet bomber of the Tu-22 type (1959) [5]. Then A.N. Tupolev and his colleagues at the Design Bureau actively continued work on the development of a turboprop strategic bomber of the Tu-95 type for long-range aviation (Fig. 8), which became a separate bright «page» in the scientific and technical biography of this scientist [11].

Fig. 7. Soviet mid-range twin-engine jet passenger aircraft of the Tu-134 type developed by A.N. Tupolev (1967) [6]

Fig. 8. Soviet turboprop four-engine strategic bomber of the Tu-95 type («Atomic Bear» in the terminology of NATO countries) developed by A.N. Tupolev and his fellow aircraft designers at the Design Bureau-156 (1956) [7, 8]

A surprising fact about aviation is the fact that a strategic bomber of the Tu-95 type (this «flying fortress» with several thermonuclear charges on board [7, 8]), developed and created under the guidance of A.N. Tupolev, more than 60 years ago, is still in the combat «ranks» of the Russian Air Force and provides its defenses in the airspace. Such examples of «longevity» in aviation technology are extremely few. In this regard, only our domestic passenger single-engine propeller airplane type AN-2 with a piston engine, developed in 1947 by the outstanding Ukrainian aircraft designer Oleg Konstantinovich Antonov [5], can compare with the military Tu-95.

We point out that in adulthood the main direction of the scientific and technical creativity of the aircraft designer A.N. Tupolev were heavy aircrafts with high payload. Taking the Tu-95 type combat aircraft as a basic design, in 1958 he created at his Design Bureau a unique passenger aircraft of the Tu-114 type (Fig. 9), well ahead of its time [5]. A reliable ultra-long-haul airbus won the leadership on long-haul lines for many years, having no analogues in the world in terms of economic efficiency.

During the years of operation, Tu-114 aircraft delivered 32 world records and there is no data in the column of flight incidents with these aircraft [5].

Fig. 9. Soviet long-distance (intercontinental) turboprop four-engine passenger aircraft of the type Tu-114 developed by A.N. Tupolev (1958) [6]

On December 31, 1968, the first in the world supersonic passenger aircraft of the Tu-144 type developed by A.N. Tupolev and his son A.A. Tupolev first flew [5]. Currently, this type of aircraft has been decommissioned in Russia due to a number of reasons.

In 1971, on the lines of the Soviet «Aeroflot», a medium-range jet three-engine passenger aircraft airbus Tu-154 appeared, which is still in the Russian flight system [11].

The personification of the Russian aviation power is currently the supersonic jet strategic bomber-missile carrier of the Tu-160 type (Fig. 10), developed in the 1980s in the Design Bureau named after A.N. Tupolev [12]. This aircraft is equipped with a variable sweep wing. It is able to carry cruise missiles with a thermonuclear charge. The aircraft of the Tu-160 type has been in service since 1984. A total of 35 such aircrafts were built. As of 2013, the Russian Air Force contained 16 Tu-160 type aircrafts [12]. It became Russia's response to the US military program AMSA within which the famous American strategic bomber of type B-1 «Lancer» was created [6, 12].

Fig. 10. Russian jet four-engine strategic bomber of the Tu-160 type («White Swan» in NATO countries terminology) developed by the Design Bureau named after A.N. Tupolev (1984, chief designer – V.I. Bliznyuk) [6]

The Tu-160 supersonic bomber carrier was launched into serial production in 1984 at the Kazan Aviation Plant. The long-range Tu-160 missile bomber is an expensive military product with unique technical characteristics. The cost of manufacturing one Tu-160 missile carrier is about USD 250 million. We indicate some tactical and technical characteristics of the Tu-160 with turbojet engines of the type HK-32 [12]: maximum range of flight is 12,300 km; maximum flight speed – 2,200 km/h; cruising flight speed – 960 km/h; machine length – 54 m; wingspan – 56 m. It is the only military product in Russia that has received its own name. These airplanes are named after famous Russian warriors (for example, «Ilya Muromets»), designers (for example, «Vitaly Kopylov»), pilots (for example, «Valery Chkalov») and others.

The great aviation designer of the 20th century, Doctor of Technical Sciences, Academician of the Academy of Sciences of the USSR, Colonel-General A.N. Tupolev established the world famous aviation scientific school, which brought up such prominent Russian aircraft designers as [5]: V.M. Petlyakov, P.O. Sukhoi, V.M. Myasishchev, A.I. Putilov, V.A. Chizhevsky, A.A. Arkhangelsky, M.L. Miles, A.P. Golubkov, I.F. Nezval, S.A. Lavochkin and A.A. Tupolev. He was the only aircraft designer in the USSR who solved the tasks of creating heavy subsonic and supersonic airplanes of various purposes [11].

3. The human qualities of the aircraft designer A.N. Tupolev. What kind of person in life was this outstanding Russian aircraft designer? Being a major scientist and designer, the head of a huge, many thousands team of engineers, technologists, test pilots, technicians and workers, Andrey Nikolaevich always remained a very simple and friendly person [5, 13]. He loved his family, valued his loved ones, adored nature, a group of friends and delicious food. In everyday life, he was extremely conservative: he preferred to wear old, but comfortable clothes. He loved to travel. In business trips abroad, he studied not only foreign science and technology, but also local nature, people and their customs. On vacation in the Moscow suburbs, he preferred hunting, fishing and playing volleyball. Before going to bed he regularly read fiction. His speech was short and capacious. His many phrases became aphorisms among colleagues. Andrey Nikolaevich maintained friendly relations with I.V. Kurchatov, A.P. Vinogradov, A.T. Tvardovsky, M.V. Keldysh, P.L. Kapitsa and many other prominent people of the time in which he lived and worked. Sergey Pavlovich Korolev, who had become an outstanding Soviet and world-renowned designer of rocket and space technology, often came to see him at work. Later S.P. Korolev in his memoirs about those meetings with A.N. Tupolev said that «*he studied with Andrey Nikolaevich style of work*» [5, 13]. By the way, under the guidance of Andrey Nikolaevich, Sergey Korolev completed his diploma project and became a mechanical engineer. Until his last days of life, he was interested in production issues at the Design Bureau. He was buried at the Novodevichy cemetery (Fig. 11) [3, 5].

In 2001, on one of the walls of the world-famous Moscow State Technical University (formerly MHTS) named after N.E. Bauman bronze memorial plaque (Fig. 12), installed in honor of his outstanding student appeared [15].

4. Awards and recognition signs of A.N. Tupolev. For his outstanding achievements in aircraft construction, Andrey Nikolayevich Tupolev was awarded three gold medals of the Hero of Labor «Sickle and Hammer» (1945, 1957, 1972), 14 Soviet (1933, 1936, 1944, 1945, 1947, 1949, 1953, 1957, 1958, 1968, 1971, 1972) and one foreign (1964) orders. He is the Laureate of five State Prizes

Fig. 11. The tombstone of the great aircraft designer of the 20th century, three times Hero of Labor A.N. Tupolev (Novodevichy cemetery, Moscow, 2012; sculptor – G. Toidze) [14]

Fig. 12. Bronze plaque in honor of A.N. Tupolev on the building of Moscow State Technical University named after N.E. Bauman, where A.N. Tupolev studied (opened on May 17, 2001; sculptor – G. Meshinev) [15]

of the USSR (1943, 1948, 1949, 1952, 1972) and one Lenin Prize of the USSR (1957). He became an honorary citizen of Paris (1964), New York (1964) and Zhukovsky (Moscow region, 1968). He was awarded the prize named after N.E. Zhukovsky of the Academy of Sciences of the USSR (1958), the gold medal of the International Aviation Federation of FAI (1958), the Leonardo da Vinci international award (1971) and the gold medal of the Society of the founders of French aviation (1971). He was elected Honorary Member of the Royal Aviation Society of Great Britain (1970) and the American Institute of Aeronautics and Astronautics (1971). His bronze bust of the Hero in the city of Kimry (Tver region, Russia) was installed. In the name of A.N. Tupolev the embankment in Moscow, streets in St. Petersburg, Kyiv, Ulyanovsk, Kimry and Zhukovsky were named. The name of the aircraft designer A.N. Tupolev is currently given to Russian Aviation Scientific-Technical Complex, Moscow, which is well-known in the world (the successor to the traditions of the legendary A.N. Tupolev Design Bureau). His name is given to the Kazan Aviation Institute. One of the islands of Russia in the Kara Sea was named after him [3, 5].

Conclusions. An outstanding aircraft designer of the 20th century, AN. Tupolev left a significant «trace» in the Russian and world aircraft design. Under his scientific and technical guidance, over 100 types of military and civil aircrafts were developed, 70 of which were mass-produced by the USSR aviation industry. He made a huge personal contribution to the defense of the Soviet country. In the national memory, Academician of the Academy of Sciences of the USSR A.N. Tupolev remains one of the creators of a wide range of aircrafts in the passenger aircraft fleet. Its turbojet passenger aircrafts, as well as heavy turboprop and turbojet strategic bombers, still «plow» world airspace and carry out civil and combat tasks assigned to them.

REFERENCES

1. Available at: http://olymp.aviaschool.net/lsra-xml/creator/debug/units/unit23.html (accessed 11 April 2016). (Rus).

2. Baranov M.I. An anthology of the distinguished achievements in science and technique. Part 47: Aircraft designer Igor Sikorsky and his accomplishments in design of airplanes and helicopters. *Electrical engineering & electromechanics*, 2019, no.1, pp. 3-8. **doi: 10.20998/2074-272X.2019.1.01.**

3. Available at: http://to-name.ru/biography/andrej-tupolev.htm (accessed 24 May 2016). (Rus).

4. Kerber L.L. *Tu – chelovek i samolet* [Tu – man and airplane]. Moscow, Soviet Russia Publ., 1973. 288 p. (Rus).

5. Available at: https://topwar.ru/22395-velikiy-aviakonstruktor-rossii.html (accessed 05 October 2017). (Rus).

6. Available at: http://olymp.aviaschool.net/lsra-xml/creator/debug/units/unit17.html (accessed 15 May 2017). (Rus).

7. Baranov M.I. An anthology of outstanding achievements in science and technology. Part 7: Nuclear and thermonuclear weapon creation. *Electrical engineering & electromechanics*, 2012, no.2, pp. 3-15. **doi: 10.20998/2074-272X.2012.2.01.**

8. Baranov M.I. *Antologiia vydaiushchikhsia dostizhenii v nauke i tekhnike: Monografiia v 3-h tomakh. Tom 1*. [An anthology of outstanding achievements in science and technology: Monographs in 3 vols. Vol.1]. Kharkov, NTMT Publ., 2011. 311 p. (Rus).

9. Available at: https://en.wikipedia.org/wiki/Tupolev_Tu-16 (accessed 19 June 2016).

10. Available at: https://en.wikipedia.org/wiki/Tupolev_Tu-104 (accessed 22 July 2016).

11. Available at: http://www.warheroes.ru/hero/hero.asp?Hero_id=10008# (accessed 05 May 2016). (Rus).

12. Available at: https://militaryarms.ru/voennaya-texnika/aviaciya/bombardirovshhik-tu-160 (accessed 04 June 2016). (Rus).

13. Bodrikhin N.G. *Tupolev (seriya ZHZL)* [Tupolev (Series of ZHZL)]. Moscow, Young Household Troops Publ., 2011. 456 p. (Rus).

14. Available at: http://www.warheroes.ru/hero/hero.asp?id=11105 (accessed 04 September 2017). (Rus).

15. Available at: http://www.warheroes.ru/hero/hero.asp?id=25194 (accessed 04 September 2017). (Rus).

Received 09.10.2018

M.I. Baranov, Doctor of Technical Science, Professor,
Scientific-&-Research Planning-&-Design Institute «Molniya»,
National Technical University «Kharkiv Polytechnic Institute»,
47, Shevchenko Str., Kharkiv, 61013, Ukraine,
phone +380 57 7076841,
e-mail: baranovmi@kpi.kharkov.ua

How to cite this article:
Baranov M.I. An anthology of the distinguished achievements in science and technique. Part 48: Aircraft designer Andrey Tupolev and his accomplishments in airplane design. *Electrical engineering & electromechanics*, 2019, no.2, pp. 3-8. **doi: 10.20998/2074-272X.2019.2.01.**

UDC 621.313.33:62–83–52 **doi: 10.20998/2074-272X.2019.2.02**

V.S. Malyar, A.V. Malyar, A.S. Andreishyn

A METHOD FOR CALCULATING MECHANICAL CHARACTERISTICS OF INDUCTION MOTORS WITH SQUIRREL-CAGE ROTOR

Purpose. Development of a method for calculating mechanical characteristics of induction motors, taking into consideration saturation of the magnetic path and displacement of the current in the rotor bars. Methodology. The algorithm is based on calculating the steady-state mode of induction motor operation for a set slip, described by a system of non-linear algebraic equations of electrical equilibrium, whereas the mechanical characteristic is evaluated as a set of steady-state modes using parameter continuation method. The idea of the steady-state mode calculation consists in determining vectors of currents and flux linkages of the motor circuits, using which makes it possible to evaluate the electromagnetic torque, active and reactive powers, etc. Results. The study resulted in the development of a method and algorithm for calculating static characteristics of induction motors, which allows looking into the effect of different laws of voltage regulation on the mechanical characteristics, depending on the frequency change. Originality. An algorithm for calculating mechanical characteristics of the squirrel-cage induction motor was developed based on the mathematical model of the induction motor in which electromagnetic parameters are calculated using real saturation curves for the main magnetic flux and leakage fluxes, and displacement of the current in the rotor bars is evaluated by presenting the rotor winding as a multi-layer structure. Applying the transformation of the electrical equilibrium equations into the orthogonal axes enabled a significant reduction of calculation volume without impairing the accuracy of the results. Practical value. The developed algorithm allows studying the effect of different laws of scalar regulation of the voltage on the mechanical characteristics of the induction motor in order to obtain the necessary torque-speed curves for their optimization. It can be used for programming frequency converters. References 10, figures 3.

Key words: **induction motor, squirrel-cage rotor, static characteristics, saturation, displacement of the current.**

Запропоновано алгоритм розрахунку механічних характеристик асинхронних двигунів з короткозамкненим ротором при різних частотах напруги живлення. В основу розрахунку покладено математичну модель асинхронного двигуна, в якій враховується насичення магнітопроводу і витіснення струму в стержнях короткозамкненого ротора. Електромагнітні процеси у двигуні описуються системою нелінійних рівнянь електричної рівноваги, записаної в перетворених до ортогональних осей координат, яка розв'язується ітераційним методом Ньютона разом з методом продовження по параметру. Для обчислення потокозчеплень контурів та диференціальних індуктивностей використовуються характеристики намагнічування основним магнітним потоком, а також потоками розсіювання статора і ротора. Для урахування витіснення струму в стержнях ротора короткозамкнена обмотка подається у вигляді багатошарової структури, утвореної розбиттям стержнів по висоті на кілька шарів. Бібл. 10, рис. 3.

Ключові слова: **асинхронний двигун, короткозамкнена обмотка, статичні характеристики, насичення, витіснення струму.**

Предложен алгоритм расчета механических характеристик асинхронных двигателей с короткозамкнутым ротором при разных частотах напряжения питания. В основу расчета положена математическая модель асинхронного двигателя, в которой учитывается, насыщение магнитопровода и вытеснение тока в стержнях короткозамкнутого ротора. Электромагнитные процессы в двигателе описываются системой нелинейных уравнений электрического равновесия, составленной в преобразованных к ортогональным осям координат, которая решается итерационным методом Ньютона вместе с методом продолжения по параметру. Для вычисления потокосцеплений контуров и дифференциальных индуктивностей используются характеристики намагничивания основным магнитным потоком, а также потоками рассеяния статора и ротора. Для учета вытеснения тока в стержнях ротора короткозамкнутая обмотка представляется в виде многослойной структуры, образованной разбитием стержней по высоте на несколько слоев. Библ. 10, рис. 3.

Ключевые слова: **асинхронный двигатель, короткозамкнутая обмотка, статические характеристики, насыщение, вытеснение тока.**

Introduction. In modern asynchronous electric drives, frequency converters are used to control the speed of rotor rotation. This method of regulation provides high technical and economic performance, since the frequency controlled electric drive opens up wide opportunities for the use of induction motors (IM) in qualitatively new technological processes and provides high energy efficiency. The development of reliable and high-quality microprocessor systems makes it possible to precisely control the operation of the electric drive in accordance with the requirements of a specific technological process, which not only ensures its quality, but also the economy of the electric power. The theoretical and practical aspects of frequency control are described in many fundamental publications [1-4], and features and analysis of scalar and vector control are presented in review papers [5, 6]. However, the problem of developing methods for studying the mechanical characteristics of IM with different laws of changing the supply voltage, despite the large number of publications, remains unresolved at the proper level.

As it is known, changing the frequency of supply voltage of the IM can smoothly adjust the angular speed of rotation of the stator magnetic field, and the slip of the rotor thus does not change. For electric drives with a small range of regulation and comparatively low dynamic properties, so-called scalar control is used [1, 4], which is relatively simple in realization. In contrast to the vector one, it is based on the use of modules of quantities that

determine the electromagnetic torque. Since the electromagnetic processes depend on the internal parameters of the IM, the inaccuracy of their determination leads to an inaccuracy in the determination of the electromagnetic torque and, as a consequence, significant deviations of the speed of rotation of the rotor from the given value [1]. This is due to the fact that in the existing control algorithms for frequency-regulated asynchronous electric drives, mathematical models of IM are used based on substitution circuits or linear differential equations [1-4], and the mechanical characteristics are calculated according to the Kloss formula, which is approximate. Changing the parameters of the squirrel-cage rotor, in particular the active resistance, is not taken into account or taken into account by the corresponding coefficients. The use of classical substitution circuits does not allow adequately to take into account all the factors influencing the processes in the motor when changing the frequency, and does not guarantee the reliability of the calculation results, especially for deep-slotted IMs. The problems of the adequacy of the results of mathematical modeling are not solved by substitution circuits with variable frequency dependent parameters, because as a result of the saturation of the magnetic core, flux linkage of the IM circuits and, therefore, electromagnetic parameters are nonlinearly dependent on all its currents and their frequency.

In order to control the operation of the IM, which operates in the frequency controlled electric drive system, it is necessary to know the values of its internal parameters, in particular the active and reactive stator and rotor resistance of the stator and rotor that are continuously changing. Undeniably, the most accurately they can be determined on the basis of solving the problem in field formulation [7, 8], however, such software requires a considerable amount of memory and time to calculate, and therefore can not meet the requirements for the speed of response of the frequency converter to the flow the process. The intermediate position is occupied by circuit methods for calculating electromagnetic parameters and active resistance. Therefore, the actual problem is the development of a mathematical model that allows one to calculate the mechanical characteristics taking into account the change in parameters due to the saturation of the magnetic core and the displacement of the current in the rods of the squirrel-cage winding as having a determining influence on the characteristics of the IM. In addition, for efficient frequency control of electric drive an important and determining factor is the speed and bulkiness of software for calculating the frequency characteristics of asynchronous electric drives, which are the basis of control algorithms.

The goal of the work is the development of a numerical method for calculating mechanical characteristics under different laws of changing the supply voltage of the IM and its frequency using a mathematical model based on the equation of the electromagnetic equilibrium of the motor circuits, which make it possible to take into account the saturation of the magnetic core and the displacement of the current in the rods of the squirrel-cage rotor.

Mathematical model. The object of the study is a IM with a squirrel-cage winding of a rotor, which is powered by a three-phase network with a symmetric voltage system. For the analysis of electromagnetic processes in the IM, a mathematical model is used built using orthogonal coordinate axes, which enables the analysis of processes by computer simulation, taking into account both saturation and displacement of current in the rods of a squirrel-cage winding of the rotor with a minimum amount of computations. To take into account the saturation, the magnetization characteristics of magnetization both by the main magnetic flux and the scattering fluxes are used, and to take account the displacement of the current, the rods together with the squirrel-cage rings are separated by height into n layers, resulting in n windings on the rotor that are covered by different magnetic scattering fluxes. The idea of such an approach is presented in [9]. As shown in [10], in practice $n \le 5$. The three-phase winding of the stator and a multiphase winding of the rotor are reduced to two-phase windings according to the generally accepted method.

Electromagnetic processes in the dynamic modes of the IM are described by a system of differential equations, which is reduced to algebraic systems in the system of orthogonal axes x, y under constant rotational speed. If the representational vector of the power supply voltage with the x-axis, are combined, which is commonly practiced, this system has the form

$$\begin{aligned}
&\omega_0\psi_{sy} - r_r i_{sx} + U_m = 0;\\
&-\omega_0\psi_{sx} - r_s i_{sy} = 0;\\
&s\omega_0\psi_{r1y} - r_1 i_{r1x} = 0;\\
&-s\omega_0\psi_{r1x} - r_1 i_{r1y} = 0;\\
&\cdots\\
&s\omega_0\psi_{rny} - r_n i_{rnx} = 0;\\
&-s\omega_0\psi_{rnx} - r_n i_{rny} = 0,
\end{aligned} \qquad (1)$$

where U_m is the amplitude value of the phase voltage; ψ_{sx}, ψ_{sy}, ψ_{r1x}, ψ_{r1y}, ..., ψ_{rnx}, ψ_{rny} are the flux linkages and currents i_{sx}, i_{sy}, i_{r1x}, i_{r1y},..., i_{rnx}, i_{rny} of the transformed stator and rotor circuits, respectively; r_s, r_{r1} ,…, r_{rn} are the active resistances of these circuits; ω is the angular frequency of the power supply voltage; s is the rotor slip.

The flux linkages of the circuits are determined on the basis of the use of the magnetization curves by the main magnetic flux ψ_μ and the scattering fluxes of the stator $\psi_{\sigma s}$ windings and the rotor $\psi_{\sigma r}$ windings

$$\psi_\mu = \psi_\mu(i_\mu), \quad \psi_{\sigma s} = \psi_{\sigma s}(i_s), \quad \psi_{\sigma r} = \psi_{\sigma r}(i_r).$$

where i_μ, i_s, i_r are the modules of the representational vectors of the corresponding currents: magnetization, stator and rotor

$$i_\mu = \sqrt{(i_{sx} + i_{rx})^2 + (i_{sy} + i_{ry})^2};$$

$$i_s = \sqrt{i_{sx}^2 + i_{sy}^2}; \quad i_r = \sqrt{i_{rx}^2 + i_{ry}^2}.$$

Since the rod is divided by height into n elements, the rotor currents are determined as the sum of currents in them

$$i_{rx}=\sum_{j=1}^{n} i_{rjx}\ ;\quad i_{ry}=\sum_{j=1}^{n} i_{rjy}\ .$$

The electromagnetic torque of the IM, in the coordinate axes *x*, *y*, is determined by the formula

$$M_e=1.5p_0\left(\psi_{sx}i_{sy}-\psi_{sy}i_{sx}\right),$$

where p_0 is the number of pairs of poles.

Active and reactive powers are determined by the formulas

$$P=1.5\left(u_{sx}i_{sx}-u_{sy}i_{sy}\right);\quad Q=1.5\left(u_{sy}i_{sx}-u_{sx}i_{sy}\right).$$

Algorithm for calculation of characteristics. The basis of the algorithm is the calculation of the steady state mode of operation of the IM for a given slip *s*, which is described by the system of algebraic equations (1), and the static characteristic is calculated as a set of steady state modes. The essence of the calculation of the steady state mode is to determine the vectors of currents and the flux densities of the circuit of the motor using which we can determine the electromagnetic torque, the active and reactive powers, and so on.

Having the given values of the power supply voltage of the stator winding and slip, the calculation of the steady state mode reduces to the solution of the system of algebraic equations (1). Due to the saturation of the magnetic core, the electromagnetic connections between its electrical circuits are nonlinear, hence the flux linkage of each circuit is nonlinearly dependent on the vector of currents

$$\vec{i}=\text{colon}\left(i_{sx},i_{sy},i_{r1x},i_{r1y},...,i_{rnx},i_{rny}\right),$$

which depend on the value of the supply voltage and are determined by the electromagnetic parameters of the IM.

One of the most effective methods for solving nonlinear systems of algebraic equations is Newton iteration method, according to which at each *k*-th step of the iteration the vector $\vec{i}$ is specified by formulas

$$\vec{i}^{(k+1)}=\vec{i}^{(k)}-\Delta\vec{i}^{(k)};\quad A\Delta\vec{i}^{(k)}=\vec{Q}^{(k)},\qquad(2)$$

where $\vec{Q}^{(k)}$ is the vector of the discrepancies of the system (1) at $\vec{i}=\vec{i}^{(k)}$; *A* is the Jacobi matrix, elements of which are differential inductances $L_{j,k}$ of circuits (own at $j=k$ and mutual at $j\neq k$) and their active resistances.

To ensure the convergence of the iterative process, it is necessary to obtain an initial approximation of the unknown vector, which is in the zone of attraction of the method. This problem is solved by a differential method, the essence of which in relation to the problem to be solved is as follows.

We introduce into the system (1) a scalar parameter ε by multiplying it by the voltage $u_{sx}=\varepsilon U_m$. As a result of the differentiation of the resulting nonlinear system by ε we obtain the differential equation in the form

$$A\frac{d\vec{i}}{d\varepsilon}=\vec{u}\ ,\qquad(3)$$

where $\vec{u}=\text{colon}\left(U_m,0,...,0\right)$.

Integration with the parameter ε in the range from $\varepsilon=0$ to $\varepsilon=1$ is equivalent to increasing the applied voltage from zero to the set value. Initial conditions (values of the vector $\vec{i}$) are zero, since for $\varepsilon=0$ the vector of the applied voltages is zero. At each step of integration, the vector $\vec{i}$ is clarified by Newton method. Gradual increase of the applied voltage makes it possible at each step to ensure the convergence of the iterative process, and therefore, after several steps of integration with the Euler method, obtain the value of the current vector $\vec{i}$ at a given value of the amplitudes of phase voltages U_m.

The obtained values are the initial conditions for the calculation of characteristics as coordinates dependencies on the slip.

Thus, the algorithm for calculating the starting static characteristic consists of two stages: the first one calculates the steady-state operation of the IM at the given values of slip and the voltage of the stator winding, and the second one is the calculation of the multidimensional static characteristic as the dependencies $\vec{i}=\vec{i}\left(s\right)$ of the coordinates of the vector of circuit currents from slip. In this case, the voltage and frequency are accepted unchanged, and the slip changes in the specified limits. In particular, to calculate the static mechanical characteristic of the IM at a given frequency of supply voltage, we need to set the slip value $s=1$ and according to the above algorithm to determine the value of the coordinates of the mode at a given value of the amplitude of the supply voltage, and then, gradually reducing the value of slip with step Δs to zero, by iterative method to calculate the multidimensional dependence $\vec{i}=\vec{i}\left(s\right)$, and hence $\vec{\psi}=\vec{\psi}\left(s\right)$as well as the electromagnetic torque $M=M\left(s\right)$.

On each step of integration, as well as iterative refinement of the vector $\vec{i}$ by the Newton method, it is necessary to determine the differential inductances of the circuits as nonlinear functions of the vector $\vec{i}$ of the currents.

Results of investigations. An example of the results of the calculation of the characteristics of two types of IM of the same power, which differ in the number of pairs of poles, one of which has a normal execution (4A160S4Y3, $P=15$ kW, $U=220$ V, $I=29.2$ A, $p_0=3$) and the second one has an increased starting torque (4AP160S4Y3, $P=15$ kW, $U=220$ V, $I=29.9$ A, $p_0=2$) due to the double cage of the rotor is shown in Fig. 1.

Fig. 2 shows the mechanical characteristics of the motors calculated at different supply voltage frequencies under voltage regulation according to the law $U_m/f=\text{const}$.

Analysis of the results of calculations (Fig. 1, 2) shows that the general view of the characteristics of the electromagnetic torque for IM with a different shape of the slots of the squirrel-cage winding of the rotor is significantly different, and the voltage reduction is proportional to the decrease in frequency does not ensure the immutability of the reloading capacity of the IM.

Shown in Fig. 2 characteristics of the electromagnetic torque correspond to the characteristics of the active power (Fig. 3).

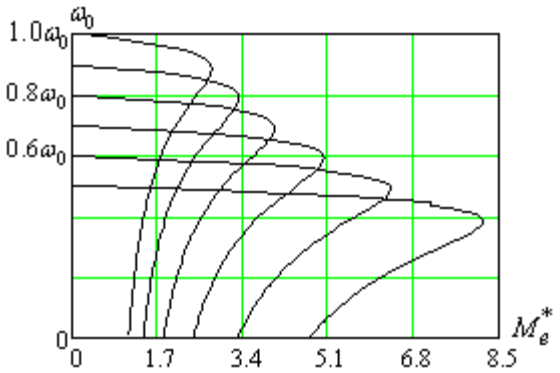

a

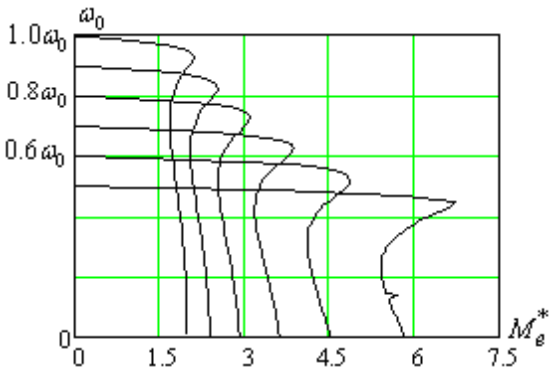

b

Fig. 1. Mechanical characteristics of motors 4A160S4Y3 (*a*) and 4AP160S4Y3 (*b*) calculated with constant amplitude of the supply voltage and its various frequencies *f*

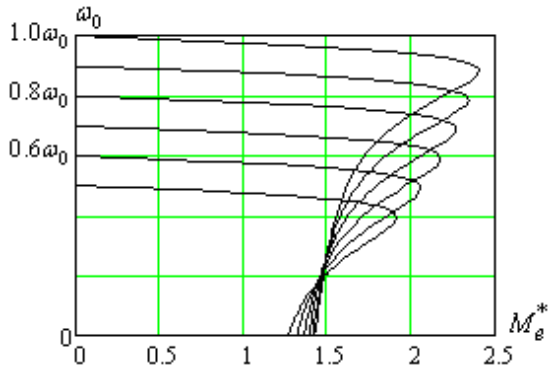

a

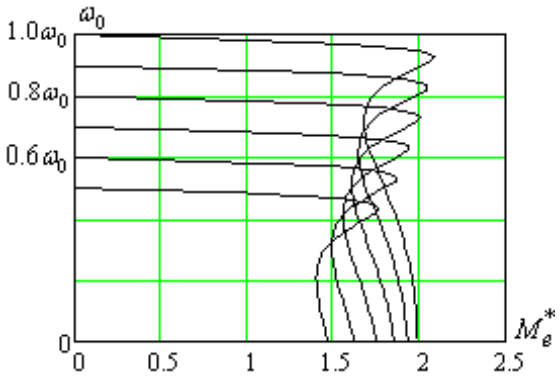

b

Fig. 2. Mechanical characteristics of motors 4A160S4Y3 (*a*) and 4AP160S4Y3 (*b*) calculated at different power supply voltage frequencies supply provided voltage regulation by law U_m/f = const

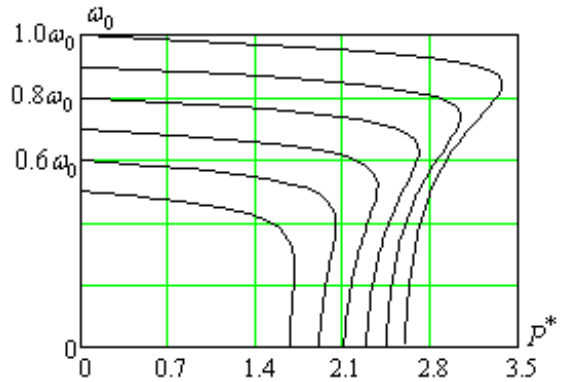

a

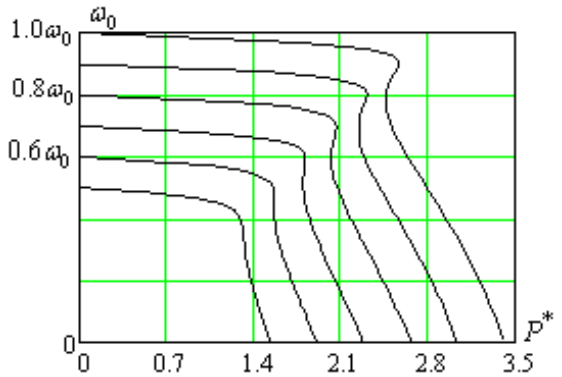

b

Fig. 3. Characteristics of the active power correspond to the mechanical characteristics shown in Fig. 2,*a*,*b*

Conclusions.

1. The proposed method of calculation enables by mathematical modeling methods to analyze the mechanical characteristics of induction motors with squirrel-cage rotor, taking into account saturation and displacement of currents in the rotor rods under different laws of voltage and frequency control in order to provide the necessary law for the change of electromagnetic torque.

2. The developed algorithm of calculation is based on the mathematical model of the IM, in which the real, calculated on the basis of the geometry of the IM magnetic core magnetization characteristic and the dividing along the depth of the slots of the rods of the squirrel-cage winding into elementary ones, which allows to adequately take into account saturation and displacement of current, which is provided the accuracy of the calculation results.

3. The developed mathematical model and the calculation algorithm created on its basis can be used for designing frequency regulated electric drives in order to form the necessary characteristics.

REFERENCES

1. Pivnyak G.G., Volkov A.V. *Sovremennye chastotno-reguliruemye asinkhronnye elektroprivody s shirotno-impul'snoi moduliatsiei* [Modern frequency controlled asynchronous electric drives with pulse width modulation]. Dnepropetrovsk, NGU Publ., 2006. 470 p. (Rus).

2. Novotny D.W., Lipo T.A. *Vector Control and Dynamics of AC Drives*. Clarendon Press Oxford, 2003. 440 p.

3. Pabitra Kumar Behera, Manoj Kumar Behera, Amit Kumar Sahoo. Speed Control of Induction Motor using Scalar Control

Technique. *International Journal of Computer Applications. Proceedings on International Conference on Emergent Trends in Computing and Communication ETCC*, 2014, no.1, pp. 37-39.
4. Aspalli M.S., Asha R., Hunagund P.V. Three phase induction motor drive using IGBTs and constant V/F method. *International Journal of Advanced Research in Electrical, Electronics and Instrumentation Engineering*, 2012, vol.1, iss.5, pp. 463-469.
5. Finch J.W., Giaouris D. Controlled AC Electrical Drives. *IEEE Transactions on Industrial Electronics*, 2008, vol.55, no.2, pp. 481-491. **doi: 10.1109/TIE.2007.911209**.
6. Boldea I. Control issues in adjustable speed drives. *IEEE Industrial Electronics Magazine*, 2008, vol.2, no.3, pp. 32-50. **doi: 10.1109/MIE.2008.928605.**
7. Vaskovskyi Yu.N., Gaydenko Yu.A., Tsivinskiy S.S. Integral characterization of electrical machines with electromagnetic field theory methods. *Electrical Engineering & Electromechanics*, 2006, no.1, pp.28-32. **doi: 10.2098/2074–272X.2016.01.05.**
8. Milykh V.I., Polyakova N.V. Determination of electromagnetic parameters of electric machines based on numerical calculations of magnetic field. *Electrical Engineering & Electromechanics*, 2006, no.2, pp.40-46. **doi: 10.2098/2074–272X.2016.02.09.**
9. Rogers G.J., Benaragama D.S. An induction motor model with deep-bar effect and leakage inductance saturation. *Archiv für Elektrotechnik*, 1978, vol.60, no.4, pp. 193-201. **doi: 10.1007/bf01595160**.
10. Stakhiv P., Malyar A. Influence of saturation and skin effect on current harmonic spectrum of asynchronous motor powered by thyristor voltage regulator. *Proceedings of the IVth International Workshop Computational Problems of Electrical Engineering*. Gdynia, Poland, June 1-3, 2005. pp. 58-60.

Received 08.11.2018

V.S. Malyar[1], *Doctor of Technical Science, Professor,*
A.V. Malyar[1], *Doctor of Technical Science, Professor,*
A.S. Andreishyn[1], *Postgraduate Student,*
[1] Lviv Polytechnic National University,
12, S. Bandera Str., Lviv, 79013, Ukraine,
phone +380 32 2582119,
e-mail: andrii.v.maliar@lpnu.ua

How to cite this article:
Malyar V.S., Malyar A.V., Andreishyn A.S. A method for calculating mechanical characteristics of induction motors with squirrel-cage rotor. *Electrical engineering & electromechanics*, 2019, no.2, pp. 9-13. **doi: 10.20998/2074-272X.2019.2.02.**

UDC 621.313.333 **doi: 10.20998/2074-272X.2019.2.03**

V.S. Petrushin, Y.R. Plotkin, R.N. Yenoktaiev, N.S. Prokopenko

RESEARCH OF DYNAMIC CHARACTERISTICS OF INDUCTION MOTORS IN ELECTRIC DRIVES WITH MATCHING TRANSFORMER AND REDUCER

Introduction. The variety of electric drives, the performance characteristics of which correspond to the set requirements of consumers while ensuring reliable and economical operation for a certain time resource, characterizes the variety of circuit solutions, including using matching transformers and reducers. Problem. The use of matching transformers and reducers units significantly changes the performance characteristics of the electric drive. Most articles are devoted to modeling an electric drive without such elements. It is advisable to consider simulations of electric drives using these elements. Methodology. In the models of matching transformers and reducers, the initial data are used, which determine both the functional properties and the mass and size parameters. The latter provide an opportunity to consider the economic aspects of the electric drive. For the correct calculation of the energy balance of the electric drive, the efficiency of the elements under consideration is taken into account. Results. The use of the developed algorithms for modeling the dynamic modes of two induction motors in electric drives operating on a specific load diagram, with the connection of a matching transformer and reducers, is considered. Dependencies of efficiency and power factor of motors have allowed to determine the medium cyclic energy indicators. The mass- size and cost indicators of variants of electric drives were found, which made it possible to calculate the average cyclic reduced costs of electric drives. Practical value. The possibility of choosing the best variant of the drive based on various indicators, including the minimum amount of energy losses per year, is substantiated. References 17, tables 2, figures 8.

Key words: **induction motor, load cyclogram, reducer, transformer, mathematical model, average cyclic criteria, energy indicators, reduced costs.**

Розглянуто використання розроблених алгоритмів для моделювання динамічних режимів двох асинхронних двигунів в електроприводах, що працюють на певну циклограму навантаження, при включенні узгоджувальних трансформатора і редуктора. Враховано мінливість параметрів схем заміщення двигунів, пов'язана зі зміною насичення магнітних кіл і витісненням струмів в обмотках роторів. Отримано і зіставлені динамічні характеристики струмів і потужностей, споживаних двигунами. Залежності ККД і коефіцієнта потужності двигунів дозволили визначити середньоциклічні енергетичні показники. Знайдено масогабаритні і вартісні показники варіантів електроприводів, що дало можливість, при відомих середньоциклічних енергетичних показниках приводів, розрахувати середньоциклічні приведені витрати електроприводів. Обґрунтовано можливість вибору кращого варіанту приводу за вищевказаними показниками, а також за мінімумом втрат електроенергії за рік. Бібл. 17, табл. 2, рис. 8.

Ключові слова: **асинхронний двигун, циклограма навантаження, редуктор, трансформатор, математична модель, середньоциклічні критерії, енергетичні показники, приведені витрати.**

Рассмотрено использование разработанных алгоритмов для моделирования динамических режимов двух асинхронных двигателей в электроприводах, работающих на определенную циклограмму нагрузки, при включении согласующих трансформатора и редуктора. Учтено непостоянство параметров схем замещения двигателей, связанное с изменением насыщения магнитных цепей и вытеснением токов в обмотках роторов. Получены и сопоставлены динамические характеристики токов и мощностей, потребляемых двигателями. Зависимости КПД и коэффициента мощности двигателей позволили определить среднециклические энергетические показатели. Найдены массогабаритные и стоимостные показатели вариантов электроприводов, что дало возможность, при известных среднециклических энергетических показателей приводов, рассчитать среднециклические приведенные затраты электроприводов. Обоснована возможность выбора лучшего варианта привода по вышеуказанным показателям, а также по минимуму потерь электроэнергии за год. Библ. 17, табл. 2, рис. 8.

Ключевые слова: **асинхронный двигатель, циклограмма нагрузки, редуктор, трансформатор, математическая модель, среднециклические критерии, энергетические показатели, приведенные затраты.**

Introduction. A variety of electric drives (ED), whose performance characteristics meet the specified requirements of consumers while ensuring reliable and economical operation for a certain time resource, characterizes the variety of circuit solutions, including using matching transformers and reducers. The value of the drive load may vary in time, which is characterized by the mode of operation described by the load cyclogram. Heating of the electric machine depends on the operation mode, i.e. on the ratio of the duration of periods of operation and pauses between them or periods of operation with full or partial load, on the frequency of switching on the machine and the nature of the flow of transients. Along with the standard modes of operation [1], non-standard ones are also possible [2, 3]. The standard ones are characterized by different time indicators (duration of switching on, duration of load, duration of operation, frequency of switching on, etc.).

The correct choice of electric drive should provide high energy performance during operation, indicating its rational use. When commensurate operation time of induction motors (IM) in steady and transient (start, transfer from one load to another) modes, transients have

a significant impact on the performance of electric drives. In some cases, IMs are operated in intermittent modes associated with alternating motor operation for loads of different values. Transients in IM were considered by a number of authors [2, 4]. At the same time, the rejection of the use of certain assumptions in the simulation of dynamic modes of IM allows us to refine the mathematical models (MM) [5].

The use of matching transformers and reducers significantly changes the performance characteristics of the ED. Most of the papers are devoted to ED modeling without such elements in both static and dynamic modes [2, 4-7]. In a number of works [8-11], the analysis is performed taking into account transformers and reducers. It is advisable to consider modeling ED using these elements.

The goal of the paper is to use the developed algorithms to simulate the dynamic modes of induction motors in electric drives with matching transformers and reducers and to substantiate the possibility of comparing the considered electric drives in terms of weight, cost, energy and cost parameters, as well as on the cost of electricity to choose a rational drive option.

Problem definition. All considered drives operate on a certain load cyclogram and provide almost the same number of revolutions on the mechanism. In the models of matching transformers and reducers, initial data are used, which determine both functional properties and weight, size and cost parameters. The latter provide an opportunity to consider the economic aspects of the ED. The functional ones are: for a reducer – a gear ratio (i_{red}), for a transformer – a transformation ratio (k_{tr}). The correctness of the calculation of the energy balance of the electric drive requires the use of the efficiency of the considered elements (η_{red}, η_{tr}). Modeling ED with the connection of reducers and transformers in static and dynamic modes, the rotational speed (n_{mech}) and torque (M_{mech}) on the drive mechanism, the power consumed by the drive (P_{ED}), the drive efficiency (η_{ED}), the power of the load mechanism (P_{mech}) are determined. In addition, it seems possible to calculate the weight, size, and cost parameters of the entire ED using any of the considered components.

Expressions that take into account the connection of the reducer and transformer in the ED when considering static modes, have the form:

$$n_{mech} = \frac{n}{i_{red}}, \tag{1}$$

$$M_{mech} = M_{IM} \cdot i_{red} \cdot \eta_{red}, \tag{2}$$

$$P_{mech} = P_{IM} \cdot \eta_{red}, \tag{3}$$

$$P_{ED} = P_1 + (1-\eta_{tr}) \cdot P_1, \tag{4}$$

$$\eta_{ED} = \eta_{IM} \cdot \eta_{tr} \cdot \eta_{red}, \tag{5}$$

$$U_2 = \frac{U_1}{k_{tr}}, \tag{6}$$

where n is the motor speed; M_{IM} is the torque on the motor shaft; P_{IM} is the useful mechanical power on the motor shaft; P_1 is the consumed active motor power; U_1 is the primary voltage of the transformer; U_2 is the secondary voltage of the transformer.

Mathematical models used to study transient electromagnetic and electromechanical processes in induction motors are based on systems of nonlinear differential equilibrium equations for voltages and currents in a system of transformed coordinates [6, 7]:

$$\begin{aligned}
&\frac{d}{dt}\Psi_{s\alpha} = u_{s\alpha}(t) - r_s d(t)\left[x_r(t)\Psi_{s\alpha}(t) - x_M(t)\Psi_{r\alpha}(t)\right],\\
&\frac{d}{dt}\Psi_{s\beta} = u_{s\beta}(t) - r_s d(t)\left[x_r(t)\Psi_{s\beta}(t) - x_M(t)\Psi_{r\beta}(t)\right],\\
&\frac{d}{dt}\Psi_{r\alpha} = [-p\omega_r \cdot \Psi_{r\beta}(t) - r_r(t)d(t)[x_s(t)\Psi_{r\alpha}(t) - \\
&\qquad - x_M(t)\Psi_{s\alpha}(t)],\\
&\frac{d}{dt}\Psi_{r\beta} = [p\omega_r \cdot \Psi_{r\beta}(t) - r_r(t)d(t)[x_s(t)\Psi_{r\beta}(t) - \\
&\qquad - x_M(t)\Psi_{s\beta}(t)],\\
&\frac{d\omega_r}{dt} = \frac{1}{J}\{\frac{3p}{2}d(t)x_M(t)[\Psi_{s\beta}(t)\Psi_{r\alpha}(t) - \Psi_{r\beta}(t)\Psi_{s\alpha}(t)] - \\
&\qquad - M_L(\omega_r)/(i_{red}\cdot\eta_{red})\},
\end{aligned} \tag{7}$$

where $\Psi_{s\alpha}(t)$, $\Psi_{s\beta}(t)$, $\Psi_{r\alpha}(t)$, and $\Psi_{r\beta}(t)$ are the flux linkages of the stator and rotor windings of the machine, respectively, along the axes α and β; ω_r is the motor angular rotation speed; p is the number of pairs of poles; J is the total moment of inertia of the drive, reduced to the motor shaft; $M_L(t)$ is the time dependence of the mechanism resistance; r_s, $r_r(t)$, $x_s(t)$, $x_r(t)$, $x_M(t)$ are the active resistances and the total reactances of the stator and rotor windings and the mutual induction resistance, and all of which, except for r_s, change at each integration step; $d(t)$ is the auxiliary variable $d(t) = [x_s(t)\cdot x_r(t) - (x_M(t))^2]^{-1}$; $u_{s\alpha}(t)$ and $u_{s\beta}(t)$ are the instantaneous values of the voltages along the α and β axes, which are determined by the voltage amplitude U_m and the angular position of the generalized voltage vector φ_1:

$$u_{s\alpha}(t) = U_m(t)\cdot\cos(\varphi_1), \quad u_{s\beta}(t) = U_m(t)\cdot\sin(\varphi_1). \tag{8}$$

The expressions connecting the instantaneous values of currents and flux linkages are as follows:

$$\begin{aligned}
i_{s\alpha}(t) &= d(t)\cdot\left[x_r(t)\Psi_{s\alpha}(t) - x_M(t)\Psi_{r\alpha}(t)\right],\\
i_{s\beta}(t) &= d(t)\cdot\left[x_r(t)\Psi_{s\beta}(t) - x_M(t)\Psi_{r\beta}(t)\right],
\end{aligned} \tag{9}$$

where $i_{s\alpha}$, $i_{s\beta}$ are the stator currents along the axes α and β. Instantaneous stator current value:

$$i_1(t) = \sqrt{\frac{1}{2}\cdot\left[i_{s\alpha}(t)^2 + i_{s\beta}(t)^2\right]}. \tag{10}$$

A mathematical model built on the basis of the above differential equations allows to calculate the rotational frequencies, currents in the phases of the windings, electromagnetic torques, losses.

In each of the equations, nonlinear coefficients take place – the motor parameters varying at each operating point, including due to the effects of saturation of the magnetic system and current displacement in the rotor winding [12, 13]. One of the approaches to the analysis of the dynamic characteristics of IM involves the preliminary determination of these factors for the necessary operating points. Therefore, before analyzing the transient process, the calculations of steady-state regimes are carried out in order to obtain the values of all the parameters of the equivalent circuit, taking into account the current displacement in the rotor winding and the magnetic core saturation for the necessary operating points. For this purpose, MMs of steady-state modes are used. When calculating the dynamic modes, the changes at each step of the system integration are taken into account, i.e. at certain points, the characteristics of the transition from one torque of load to another, the parameters of the equivalent circuit. When implementing this approach, an increase in the level of MM adequacy is provided.

In a number of publications [14-16], in contrast to the classical theory, according to which the values of powers are calculated as integral, instantaneous values of powers are used. Then the conditional active power consumed by the motor in dynamic modes under the condition of sinusoidal supply voltage is calculated through instantaneous values of voltages and currents:

$$p_1'(t) = \frac{3}{2} \cdot \left[u_{s\alpha}(t) \cdot i_{s\alpha}(t) + u_{s\beta}(t) \cdot i_{s\beta}(t) \right]. \quad (11)$$

The actual consumed active power p_1 is more than conditional one by the amount of the unaccounted losses (the main ones in the magnetic core $\Delta p_{st\ base}$, the additional ones in the magnetic core $\Delta p_{st\ add}$, mechanical ones Δp_{mech}, additional ones Δp_{mech}):

$$p_1(t) = p_1'(t) + \Delta p_{st\ base}(t) + \Delta p_{st\ add}(t) + \\ + \Delta p_{mech}(t) + \Delta p_{add}(t). \quad (12)$$

The power at the motor shaft can be determined through flux linkages and currents using the rotor speed value:

$$p_{IM}(t) = \omega_r \frac{3p}{2} \left[i_{r\beta}(t) \Psi_{r\alpha}(t) - i_{r\alpha}(t) \Psi_{r\beta}(t) \right] - \\ - \Delta p_{mech}(t) - \Delta p_{add}(t). \quad (13)$$

The instantaneous value of efficiency is determined by the ratio of the instantaneous values of useful power on the motor shaft p_{IM} to the consumed active power p_1.

As the drive selection criteria, the mass, dimensions, cost of the motor or drive, average cyclic reduced manufacturing and operating costs (RC_{mc}), average cyclic energy indicators (efficiency and power factor) can be used, or a generalized criterion can be applied, taking into account the above criteria as components. Conventionally, the criteria can be divided into two groups: weight and size and cost; energy and costly. Selection results vary with different criteria used or with their different components in the generalized criteria, and also depend on the assigned coefficients of significance of these components. When calculating the criteria, their values in transient operating modes can be taken into account. This approach allows to make a choice for both modes of operation, in which the duration of transient modes is much less than the duration of operation in steady-state modes, and for modes with commensurability of the above durations.

In the case of taking into account transients, the energy-cost group of criteria for the motor or drive is determined by:

$$\eta_{mc\,IM(ED)} = \frac{1}{t_{end} - t_{start}} \cdot \int_{t_{start}}^{t_{end}} \eta_{IM(ED)}(t)\ dt, \quad (14)$$

$$\cos\varphi_{mc\,IM(ED)} = \frac{1}{t_{end} - t_{start}} \cdot \int_{t_{start}}^{t_{end}} \cos\varphi_{IM(ED)}(t)\ dt, \quad (15)$$

$$RC_{mc\,IM(ED)} = \frac{1}{t_{end} - t_{start}} \cdot \int_{t_{start}}^{t_{end}} RC_{IM(ED)}(t)\ dt, \quad (16)$$

where t_{end} is the cycle end time; t_{end} is the cycle start time.

With a known full cost of the motor *cim* the value of the criterion is defined as:

$$RC_{IM} = (cim + C_{rIM})[1 + T_N(k_{de} + k_s)] + CL_{IM},$$

where C_{rIM} is the cost of expenses for reactive power compensation, UAH; CL_{IM} is the cost of electricity losses for the year, UAH; T_N is the standard payback period of the motor, years; k_{de} is the share of costs for depreciation; k_s is the share of maintenance costs for motor operation.

For common industrial IM, the following values are accepted: T_N = 5 years, k_{de} = 0.065, k_s = 0.069. Then $RC_{IM} = 1.67(cim + C_{rIM}) + CL_{IM}$, where $C_{rIM} = C_{cre}P_1(\mathrm{tg}\varphi_1 - -0.484)$ and $CL_{IM} = C_{cae}P_1(1.04 - \eta_{IM})$, C_{cae} is the coefficient taking into account the cost of active energy losses, which is a product of cost of 1 kW·h of electricity during the service life of the motor (0.05 USD per kW·h), the number of motor operation hours per year (2100), the number of years of operation before major repairs (5) and the ratio of the relative motor load (1.0), C_{cre} is the coefficient taking into account the cost of reactive energy compensation and representing the product of the cost of 1 kVAr of the reactive power of compensating devices (15 USD for 1 kVAr), the coefficient of motor participation in the maximum load of the system (0.25) and the ratio of the relative load. Similarly, at the known cost of the entire electric drive *ced*, the reduced costs of the drive RC_{ED} are determined.

If as a selection criterion to use such an energy indicator as efficiency, energy-saving operation of the motor will be provided.

Results of investigations. In accordance with the above-mentioned, the DIMDrive code, similar to the DIMASDrive software [17], was developed at the Department of Electric Machines of the Odessa National Polytechnic University. The code is based on system

principles, allowing to take into account the presence of certain possible components of the electric drive. In this regard, along with the IM models (for the steady state based on the T-shaped equivalent circuit, for the dynamic mode on the system of differential equations of a generalized machine), the load diagram $M(t)$ is included in the complex project model, and if necessary, models of transformer and reducer (between the motor and the load) matching voltage values of the network and the motor. Motor models involve the consideration of machines of various designs, degrees of protection, ventilation systems, types of rotors, etc. and take into account the change in the parameters of the equivalent circuit of the motor due to the saturation of the steel of the magnetic core and the displacement of currents in the motor windings, the presence of main and additional losses in steel in static and dynamic modes of the motor operation, the presence of higher spatial harmonics of the magnetic field. The analysis of electromagnetic, electromechanical, energy, thermal processes during the IM operation for various in value and mode of operation the load is provided. The code allows to implement a comprehensive analysis of the operation of IM, on the basis of which all the most important aspects of motor operation are considered.

The above software was used to simulate the operation of motors and electric drives in solution of this production problem.

The load is described by the following cyclogram: 2 s – 50 N·m, 1 s – 98 N·m. Four variants of electric drives are considered at supply voltage of 380 V and network frequency of 50 Hz which is reflected in Fig. 1.

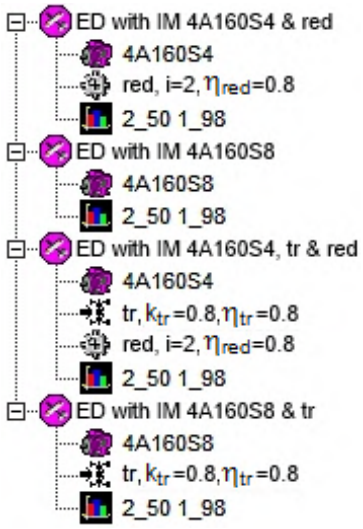

Fig. 1. Window of options of electric drives of the DIMDrive software

Motors 4A160S4 and 4A160S8 are used. In different variants there were different total moments of inertia, taking into account the moments of inertia of the motor and drive mechanism (ED with 4A160S4 – 0.3 kg·m^2, ED 4A160S8 – 0.5 kg·m^2). To ensure the same speed of rotation of the mechanism, the reducers are included in the variants with the 4A160S4 motor. Reducer parameters are shown in Fig. 2. For simplification the weight, size and cost parameters of the reducer are taken conditionally equal to 100.

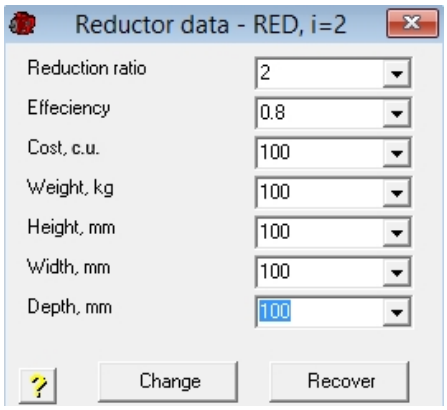

Fig. 2. Window of reducer parameters of the DIMDrive software

In two variants, a transformer was used at the drive input, the parameters of which are shown in Fig. 3. To simplify, the weight, size, and cost parameters of the transformer are taken conditionally equal to 100. To obtain $\cos\varphi_{mcED}$ values, the calculation transformer power factor is used (k_{ptrc} = 0.8):

$$\cos\varphi_{\mathrm{mc}ED} = \cos\varphi_{mcIM} \cdot k_{ptrc}. \qquad (17)$$

The performed thermal calculations (the maximum torque from the cyclogram for the steady state is set) showed the temperature of the motor stator winding exceeding the permissible value in the ED with IM 4A160S8 with transformer (Fig. 4). Therefore, this drive option is not considered further. The numbering of the characteristics corresponds to the variant numbering of the electric drives in Table 1, namely: 1 – ED with IM 4A160S4 with a reducer; 2 – ED with IM 4A160S8 without reducer and transformer; 3 – ED with IM 4A160S4 with reducer and transformer; 4 – ED with IM 4A160S8 with transformer.

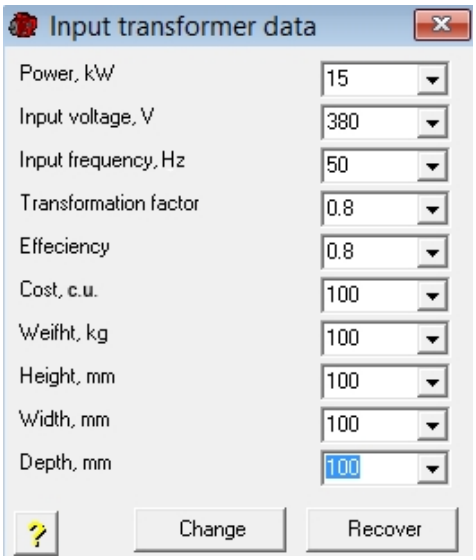

Fig. 3. Window of transformer parameters of the DIMDrive software

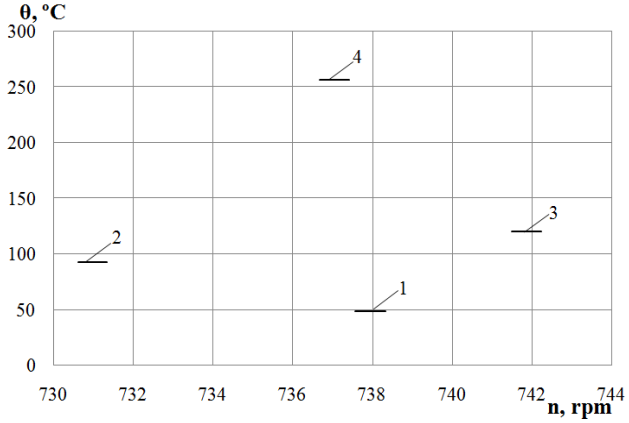

Fig. 4. Temperatures of motors' stator windings

Dynamic characteristics, which are dependencies of changes in electrical, energy values in time at the motor input, are presented in Fig. 5-8. The numbering of the characteristics corresponds to the variant numbering of the electric drives in Table 1. The code DIMDrive allows, when considering the dynamic characteristics, to exclude the starting mode from the presentation, which was done later. Similarly, the dynamic characteristics can be calculated at the input of the drive.

Table 1 shows the values of the indicators of the considered ED, which include the medium cyclic efficiency (η_{mc}), the power factor ($\cos\varphi_{mc}$), the reduced costs (RC_{mc}), as well as the weight, size, and cost parameters of both the motors and the drives.

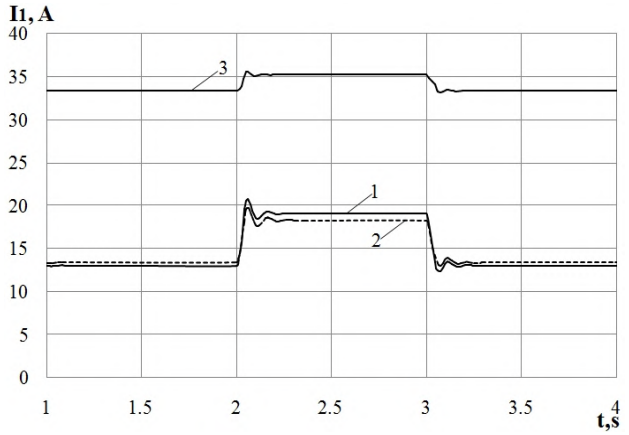

Fig. 5. Dependencies of currents consumed by motors

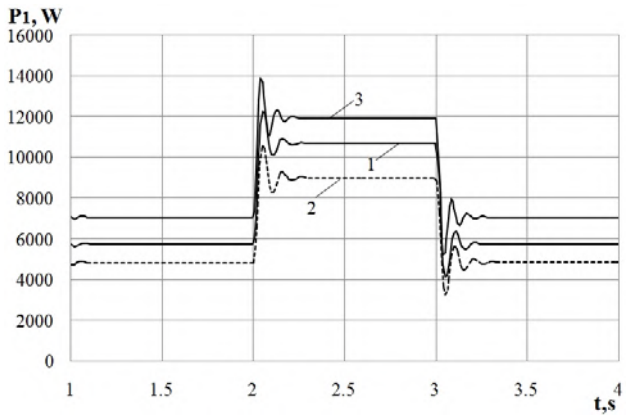

Fig. 6. Dependencies of active powers consumed by motors

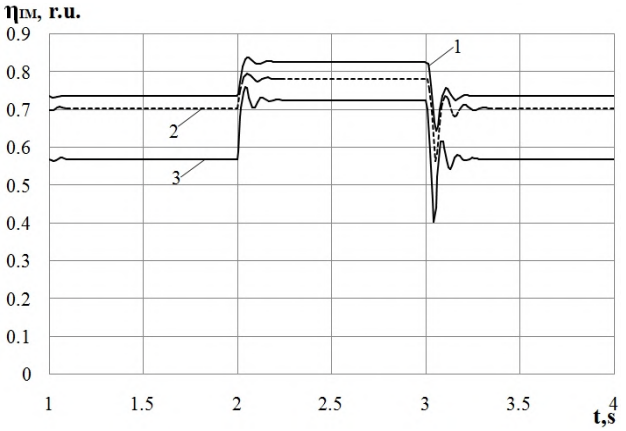

Fig. 7. Motors efficiency dependencies

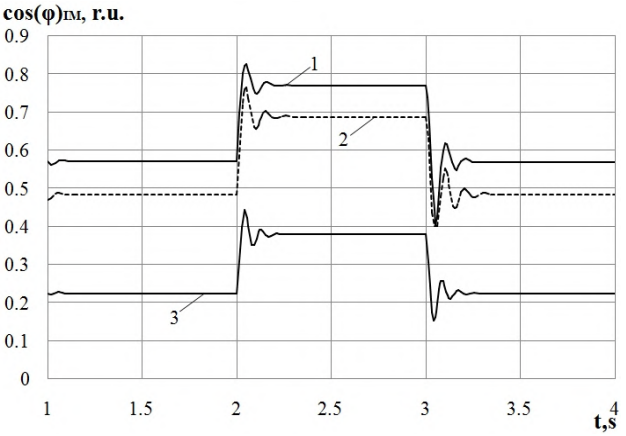

Fig. 8. Motors power factor dependencies

Table 1

Comparison of various ED indicators

Indicators and parameters / ED	No.1 – with 4A160S4 with reducer	No. 2 – with 4A160S8 without reducer and transformer	No. 3 – with 4A160S4 with reducer and transformer
η_{mc} IM, %	76.54	72.89	62.16
$\cos\varphi_{mc}$IM, r.u.	0.636	0.551	0.276
η_{mc} ED, %	61.23	72.89	39.78
$\cos\varphi_{mc}$ ED, r.u.	0.636	0.551	0.221
RC_{mc} IM, USD	2172	1980	3146
RC_{mc} ED, USD	2932	1980	5181
Mass of IM, kg	118.9	111.8	118.9
Volume of IM, dm^3	9.62	10.73	9.62
Cost of IM, USD	642	552	642
Mass of ED, kg	218.9	111.8	318.9
Volume of ED, dm^3	10.62	10.73	11.62
Cost of ED, USD	742	552	842

The calculation of the cost of active energy loss per year can be performed:

$$C_a = C \cdot T_{year} \cdot K_L \cdot P_{ED} \cdot (1 + 0.04 - \eta_{mcED}) / \eta_{mcED}, \quad (18)$$

where C = 0.05 USD is the price per 1 kW·h; T_{year} = 2100 is the number of hours of ED operaton in the year; K_L is the load factor (taken equal to 1.0); 0.04 is the relative value of losses in the consumer's distribution network.

Comparison of the considered ED variants at the cost of active energy losses for the year (Table 2) was made.

Table 2

Comparison of the cost of active energy losses of various ED

Indicators and parameters \ ED	No.1 – with 4A160S4 with reducer	No. 2 – with 4A160S8 without reducer and transformer	No. 3 – with 4A160S4 with reducer and transformer
η_{mc} ED, %	61.23	72.89	39.78
Cost of active energy losses per year, USD	541	279	1768

Conclusions

1. The DIMDrive code has been developed, which allows analyzing the dynamic modes of operation of induction motors, including in electric drive systems with matching transformers and reducers, and this is the basis for designing motors for various operating modes.

2. For comparison of the efficiency of the considered electric drives, the medium cyclic criteria of the energy and cost groups are proposed, which take into account the corresponding indicators in both the steady-state and the transient modes.

3. Of the three considered electric drives, ED with 4A160S8 motor without a reducer and a transformer has the advantage for the following reasons:

- the highest value of the medium cyclic efficiency of the electric drive;
- the lowest value of the medium cycle reduced costs of the electric drive;
- the lowest value of the cost of active energy losses per year.

4. If the medium cyclic power factor of the electric drive is used as the selection criterion, then the ED with the 4A160S4 motor with a reducer has an advantage.

REFERENCES

1. IEC 60034-1:2004. Rotating electrical machines – Part 1: Rating and performance.

2. Bespalov V.Y., Dunaykina E.A. Moshchinskii Y.A. *Nestatsionarnye teplovye raschety v elektricheskih mashinah* [Unsteady heat calculations in electrical machines]. Moscow, MEI Publ., 1987. 72 p. (Rus).

3. Dunaykina E.A. *Razrabotka modifikatsii asinkhronnykh dvigatelei edinoi serii 4A (H = 56-132 mm) dlia kratkovremennykh rezhimov*. Avtoref. diss. kand. tekhn. nauk [Development modifications asynchronous motors single series 4A (H = 56-132 mm) for the short-term operation. Abstracts of cand. tech. sci. diss.]. Moscow, 1986. 20 p. (Rus).

4. Nyein Nyein Soe, Thet Thet Han Yee, Soe Sandar Aung. Dynamic Modeling and Simulation of Three-phase Small Power Induction Motor. *World Academy of Science, Engineering and Technology*, 2008, no.42, pp. 421-424.

5. Verbovoi A.P., Verbovoi P.F. Problems of modeling of transient electromagnetic processes in asynchronous machines. *Technical electrodynamics. Thematic issue «Problems of modern electrical engineering»*, 2004, chapter 2, pp. 65-70. (Rus).

6. Kopylov I.P. *Matematicheskoe modelirovanie elektricheskih mashin* [Equipment of the electrode plants mathematical modeling of electrical machines]. Moscow, High School Publ., 1987. 248 p. (Rus).

7. Petrushin V.S. *Asinhronnye dvigateli v reguliruemom elektroprivode: Uchebnoe posobie* [Induction motors in adjustable electric: Textbook]. Odessa, Nauka i tehnika Publ., 2006. 320 p. (Rus).

8. Zhao C., Ren Z., Zhou X., Wen B. The Online Monitoring of the Dynamic Characteristics for an Induction Motor and Gearbox Transmission System. *Second International Conference on Innovative Computing, Informatio and Control (ICICIC 2007)*, Kumamoto, 2007. pp. 532-532. **doi: 10.1109/ICICIC.2007.582.**

9. Evon S., Schiferl R. Direct-drive induction motors: using an induction motor as an alternative to a motor with reducer. *IEEE Industry Applications Magazine*, 2005, vol.11, no.4, pp. 45-51. **doi: 10.1109/MIA.2005.1458276.**

10. Rojas-Moreno A. Parameter extraction of an induction motor with gearbox for dynamic simulation. *2016 IEEE ANDESCON*, pp. 1-4. **doi: 10.1109/ANDESCON.2016.7836207.**

11. Shwehdi M.H., Hye A., Quasem M.A. Economic analysis and evaluation of transformer and induction motor losses costs using PC software. *1993 (25th) Southeastern Symposium on System Theory*, pp. 63-67. **doi: 10.1109/SSST.1993.522743.**

12. Petrushin V.S., Ryabinin S.V., Yakimets A.M. Analysis of losses and thermal state of an asynchronous motor in frequency control. *Works of the Institute of Electrodynamics of the National Academy of Sciences of Ukraine*, 1999, no.1, pp. 31-36. (Rus).

13. Petrushin V.S., Bendahmane Boukhalfa, Yakimets A.M., Kalenik O.V. Influence of magnetic core steel saturation and rotor current displacement on dynamic characteristics of adjustable-speed induction motors. *Electrical Engineering & Electromechanics*, 2010, no.2, pp. 21-23. (Rus). **doi: 10.2098/2074–272X.2010.02.06.**

14. Tonkal V.E., Novoseltsev A.V., Denisiuk S.P. *Balans energii v silovykh tsepiakh* [Balance of energies in power circuits]. Kiev, Naukova dumka Publ., 1992. 312 p. (Rus).

15. Rodkin D.I. The balance of the components of the instantaneous power of polyharmonic signals. *Transactions of Kremenchuk Mykhailo Ostrohradskyi National University*, 2007, no.3(44), part 1, pp. 66-71. (Rus).

16. Orlovskii I.A. On the power in an electrical circuit with a valve. *Works of the Tavria State Agrotechnological University*, 2013, no.13, vol.4, pp. 141-150.

17. Petrushin V.S., Rjabinin S.V., Yakimets, A.M. *Programmnyj produkt «DIMASDrive». Programma analiza raboty, vybora i proektirovanija asinhronnyh korotkozamknutyh dvigatelej sistem reguliruemogo elektroprivoda* [Program performance analysis, selection and design of asynchronous cage motors controlled drive systems]. Patent UA, no.4065. (Ukr).

Received 29.08.2018

V.S. Petrushin[1], *Doctor of Technical Science, Professor,*
Y.R. Plotkin[2], *Candidate of Technical Science, Professor,*
R.N. Yenoktaiev[1], *Postgraduate Student,*
N.S. Prokopenko[1], *Master of Science,*

[1] Odessa National Polytechnic University,
1, Shevchenko Avenue, Odessa, 65044, Ukraine,
phone +380 48 7058494,
e-mail: victor_petrushin@ukr.net,
rostik-enok@ukr.net, nikita_prokopenko@yahoo.com
[2] HWR Berlin,
Alt Friedrichsfelde 60, 10315 Berlin, Germany,
phone +49 (0)30 30877-2443,
e-mail: juriy.plotkin@hwr-berlin.de

How to cite this article:
Petrushin V.S., Plotkin Y.R., Yenoktaiev R.N., Prokopenko N.S. Research of dynamic characteristics of induction motors in electric drives with matching transformer and reducer. *Electrical engineering & electromechanics*, 2019, no.2, pp. 14-20. **doi: 10.20998/2074-272X.2019.2.03.**

UDC 621.3.01 **doi: 10.20998/2074-272X.2019.2.04**

B.I. Kuznetsov, T.B. Nikitina, I.V. Bovdui, B.B. Kobilyanskiy

IMPROVING OF ELECTROMECHANICAL STABILIZATION SYSTEMS ACCURACY

Aim. ***Improving of accuracy parameters and reducing of sensitivity to changes of plant parameters for nonlinear robust tank main armament guidance and stabilization electromechanical systems based on synchronous motor with permanent magnets and vector control.*** ***Methodology.*** ***The method of multiobjective synthesis of nonlinear robust control by nonlinear tank main armament stabilization electromechanical system taking into account the elastic oscillations of the tank gun barrel as a discrete-continuous plant and with parametric uncertainty based on the multiobjective optimization. The target vector of robust control choice by solving the corresponding multicriterion nonlinear programming problem in which the calculation of the vectors of the objective function and constraints is algorithmic and associated with synthesis of nonlinear robust controllers and modeling of the synthesized system for various modes of operation of the system, with different input signals and for various values of the plant parameters. Synthesis of nonlinear robust controllers and non-linear robust observers reduces to solving the system of Hamilton-Jacobi-Isaacs equations.*** ***Results.*** ***The results of the synthesis of a nonlinear robust tank main armament guidance and stabilization electromechanical systems are presented. Comparison of the dynamic characteristics of the synthesized tank main armament stabilization electromechanical systems showed that the use of synthesized nonlinear robust controllers allowed to improve the accuracy parameters and reduce the sensitivity of the system to changes of plant parameters in comparison with the existing system.*** ***Originality.*** ***For the first time carried out the multiobjective synthesis of nonlinear robust tank main armament stabilization electromechanical systems.*** ***Practical value.*** ***Practical recommendations are given on reasonable choice of the gain matrix for the nonlinear feedbacks of the regulator and the nonlinear observer of the tank main armament stabilization electromechanical systems, which allows improving the dynamic characteristics and reducing the sensitivity of the system to plant parameters changing in comparison with the existing system.*** References 24, figures 1.

Key words: **tank main armament guidance and stabilization electromechanical systems, nonlinear robust control, multiobjective synthesis, dynamic characteristics.**

Цель. ***Повышение параметров точности и уменьшение чувствительности к изменениям параметров объекта управления нелинейной робастной электромеханической системы наведения и стабилизации танкового вооружения на основе синхронного двигателя с постоянными магнитами и векторного управления.*** ***Методология.*** ***Метод многокритериального синтеза нелинейных робастных регуляторов для управления нелинейной электромеханической системой стабилизации танкового вооружения с учетом упругих колебаний ствола танковой пушки как дискретно-континуального объекта управления с параметрической неопределенностью основан на выборе вектора цели робастного управления путем решения соответствующей задачи многокритериального нелинейного программирования, в которой вычисление векторов целевой функции и ограничений носит алгоритмический характер и связано с синтезом нелинейных робастных регуляторов и моделированием синтезированной системы для различных режимов работы системы, при различных входных сигналах и для различных значений параметров объекта управления. Синтез нелинейных робастных регуляторов и нелинейных робастных наблюдателей сводится к решению системы уравнений Гамильтона–Якоби–Айзекса.*** ***Результаты.*** ***Приводятся результаты синтеза нелинейной робастной электромеханической системы наведения и стабилизации танкового вооружения. Сравнение динамических характеристик синтезированной электромеханической системы наведения и стабилизации танкового вооружения показало, что применение синтезированных нелинейных робастных регуляторов позволяет повысить параметры точности и снизить чувствительность системы к изменению параметров объекта управления по сравнению с существующей системой.*** ***Оригинальность.*** ***Впервые проведен многокритериальный синтез нелинейной робастной электромеханической системы наведения и стабилизации танкового вооружения.*** ***Практическая ценность.*** ***Приводятся практические рекомендации по обоснованному выбору матриц коэффициентов усиления нелинейных обратных связей регулятора и нелинейного наблюдателя электромеханической системы стабилизации танкового вооружения, что позволяет улучшить динамические характеристики и снизить чувствительность системы к изменению параметров объекта управления по сравнению с существующей системой.*** Библ. 24, рис. 1.

Ключевые слова: **электромеханической системы наведения и стабилизации танкового вооружения, нелинейная робастное управление, многокритериальный синтез, динамические характеристики.**

Introduction. Ukraine is a tank country, which has plants for the production and repair of tanks and tank equipment. Ukrainian tanks have rather high tactical technical characteristics and are well bought by many foreign countries [1]. Most tanks of the Ukrainian armed forces are T-64 tanks which was developed in the 60s and which need to be modernized. Ukrainian «Bulat» T-64BM tank is the result of a deep modernization of the T-64 tank [2]. It was developed by the A.A. Morozov Kharkiv Machine Building Design Bureau. The upgraded «Bulat» T-64BM tank is equipped with a modern command and control system with a livelihood that provides the shooting of the gunner and the commander with a high probability falling from the first shot [2]. It should be noted that the cost of the «Oplot» tank production is equivalent to the cost of upgrading ten T-64 tanks to the «Bulat» T-64BM tank level [3]; therefore, the modernization of T-64 tanks is also reasonable from an economic point of view.

The basis of combat in modern conditions is shooting on the move at high speed and maneuverability of tank movement [1, 2], therefore all modern tanks of the world are equipped with stabilizers of tank armament, which allow to conduct aimed fire on the move [4–8]. The likelihood of fire damage to the target at maximum speeds of movement, high maneuverability and effective engagement of the tank from the fire damage of the

enemy is largely determined by the accuracy of maintaining a given direction of tank weapons on the target with intense disturbing influences from the tank hull [1, 2]. Therefore, the issues of further improving the accuracy of stabilization of main tank armament are a real problem, both in the development of new systems of tank weapons and in the modernization of existing systems that are in use [1-3].

One of the areas of modernization of the T-64 tank is to improve the accuracy of control of the main armament to increase the likelihood of target destruction. The guidance and stabilization system for the main armament of the T-64 tank contains a DC electric drive with an electric machine power amplifier in the azimuth (turret) axis of the tank turret and an electro-hydraulic drive of the tank gun in the in the elevation (gun) axis [1]. To improve the accuracy of controlling the main armament of «Leopard» 2A5/6, «Merkava» Mk-3, «Abrams» M1 tanks modern AC electric drives are being developed to replace existing electro-hydraulic and DC electric drives [10]. The «VNII «Signal»« scientific and industrial production unit developed and conducted experimental studies of 2E58 Electric Gun and Turret Drive Stabilization System with AC electric drive based on a synchronous motor with permanent magnets (PMSM) and vector control (VC) to replace existing DC drives and electro-hydraulic drives of main tank armament guidance and stabilization systems [11, 12]. Such an AC electric drive allows for higher speeds and accelerations of the tank turret and gun compared with existing electro-hydraulic drives and DC drives to improve the accuracy of the guidance and stabilization system. Experimental studies of such AC electric drives for controlling the turret and gun of the T-72 tank made it possible to improve the transfer speed by up to 1.5 times (up to 45 *degrees/sec*) and also to improve the smoothness of the drives at low speeds [10].

Note that the American firm «HR Textron», the Israeli firm «Elbit» based on the developed system for the «Merkava» Mk3 tank, the European concern «EADS» and others offer a fully electric guidance and stabilization system (Electric Gun and Turret Drive Stabilization System) by the main armament for the modernization of Ukrainian tanks [10].

As numerous tests and analysis of test results have shown, that the accuracy of firing on the move is significantly affected by the tank gun barrel elastic oscillations [2, 8]. «Bulat» T-64BM tank gun 2A46-2 barrel undamped oscillations frequency experimentally determined and is equal 10.14 *Hz* [8], which holds back the improve by the tank tower and gun guidance and stabilization systems accuracy.

Mathematical model of the tank gun as a plant, taking into account the gun barrel elastic oscillations as a discrete-continuous plant developed in the [8]. The gun barrel is considered as an elastic beam in the form of a distributed load, rigidly fixed in the breech. But this model does not take into account the turret imbalance, which leads to the removal of the turret with gun from the target direction. Note that the Ukrainian tanks turret unbalance moment reaches 40 k$N{\cdot}m$ against 1–1.5 k$N{\cdot}m$ at the foreign tanks turret [11].

The problem of parametric synthesis of guidance and stabilization systems, taking into account the elasticity of the tank gun barrel also is given in the [8]. However, these systems use the classical structure of regulators with feedbacks from electric angle gyros sensor and electric rate gyros sensor on the gun in the elevation (gun) axis and the turret in the azimuth (turret) axis, which limits the possibilities of obtaining high accuracy of the system.

On the other hand, the emergence of modern micro gyros and high-speed computing means allows us to reduce the weight and dimensions of the control system and implement more complex control algorithm.

The goal of this work is to improve of the accuracy parameters and reduce of sensitivity to changes of plant parameters for electromechanical tank armament stabilization systems with synchronous motor with permanent magnets and vector control based on multiobjective synthesis of nonlinear robust control.

Problem statement. Consider the mathematical models of the electromechanical gun stabilization system taking into account the gun barrel elastic elements oscillations as a discrete-continuous plant [8]. Model consists of an elevation (gun) axis model and an azimuth (turret) axis model. Imagine a gun model in the form of a solid body and an elastic element. In addition to rotation relative to the axis, the gun performs elastic oscillations. Denote by the $\varphi(t)$ – elevation angle and $\psi(t)$ – azimuth angle of gun and turret rotation as the solid body, $y_G(x, t)$ and $y_T(x, t)$ – the deviation of the points of the rod from its undeformed state in elevation and azimuth axes. For the gun and turret dynamics, the torques applied to the solid body equals the actuator torques $T_{AG}(t)$, $T_{AT}(t)$ plus the disturbance torques $T_{DG}(t)$, $T_{DT}(t)$ acting on the gun and turret, minus the turnnion friction torques. $T_{FG}(t)$, $T_{FT}(t)$. The disturbance torques $T_{DG}(t)$, $T_{DT}(t)$ acts relative to the elevation and azimuth axes of rotation of gun and turret as solid body, and the distributed forces $F_{0G}(x, t)$, $F_{0T}(x, t)$ acts along the length of the tank gun barrel as elastic element in elevation and azimuth axes.

The equations of plant movement relative to its elevation and azimuth axes of rotation can be written as follows

$$J_{0G}\frac{d^2\varphi(t)}{dt^2}(t)-\int_r^{r+l} m_1(x)\frac{\partial^2 y_G(x,t)}{\partial t^2}dx = T_{AG}(t)+ \\ +T_{DG}(t)-T_{FG}(t); \quad (1)$$

$$J_{0T}\frac{d^2\psi(t)}{dt^2}(t)-\int_r^{r+l} m_1(x)\frac{\partial^2 y_T(x,t)}{\partial t^2}dx = T_{AT}(t)+ \\ +T_{DT}(t)-T_{FT}(t), \quad (2)$$

where J_{0G}, J_{0T} – moment of inertia of gun and turret as the solid body relative to the elevation and azimuth rotation axes; $m_1(x)$ – the mass of the rod, which is connected with the running weight of the rod $m(x)$ in the ratio $m_1(x) = m(x)(x + r)$, in which r – the distance of the point of attachment of the rod to the axis of the gun gate.

This equations (1), (2) describes the free movement of the electromechanical system as a discrete-continuous plant, in which J_{0G}, J_{0T} has the characterization of the

electromechanical system as a solid body, and $m_1(x)$ characterizes the mutual influence of the motion of the solid body and the oscillations of the elastic bar as a plant mechanical part with distributed parameters. The functions $y_G(x, t)$, $y_T(x, t)$ in (1), (2) satisfies of the elastic beam oscillation equations

$$m_1(x)\frac{d^2\varphi(t)}{d^2t}+m(x)\frac{\partial^2 y_G(x,t)}{\partial t^2}+EI(x)\frac{\partial^4 y_G(x,t)}{\partial x^4}+ \\ +\xi EI(x)\frac{\partial^5 y_G(x,t)}{\partial x^4\partial t}=F_{0G}(x,t); \quad (3)$$

$$m_1(x)\frac{d^2\psi(t)}{d^2t}+m(x)\frac{\partial^2 y_T(x,t)}{\partial t^2}+EI(x)\frac{\partial^4 y_T(x,t)}{\partial x^4}+ \\ +\xi EI(x)\frac{\partial^5 y_T(x,t)}{\partial x^4\partial t}=F_{0T}(x,t), \quad (4)$$

where $EI(x)$ and ξ – tank gun barrel distributed rigidity and internal damping coefficient; $F_{0G}(x, t)$, $F_{0T}(x, t)$ – external disturbance distributed over the tank gun barrel due to hull oscillations in elevation and azimuth axes.

We represent in equation (3), (4) the functions $y_G(x,t)$, $y_T(x, t)$ in the form of the following series

$$y_G(x,t)=\sum_{i=1}^{n}\gamma_{iG}(x)W_{iG}(t); \quad (5)$$

$$y_T(x,t)=\sum_{i=1}^{n}\gamma_{iT}(x)W_{iT}(t), \quad (6)$$

where n – the number of forms of plant elastic oscillations taken into account.

The equations obtained from (1)–(6) describe the motion of an electromechanical system as a discrete-continuous plant under the action of an actuator torques $T_{AG}(t)$, $T_{AT}(t)$, disturbance torques $T_{DG}(t)$, $T_{DT}(t)$, turning friction torques $T_{FG}(t)$, $T_{FT}(t)$, as well as the length distribution of the tank gun barrel of external perturbations $F_{0G}(x, t)$, $F_{0T}(x, t)$ which is due to hull oscillations in elevation and azimuth axes;

$$J_{0G}\frac{d^2\varphi(t)}{dt^2}-\sum_{i=1}^{n}\frac{d^2W_{iG}(t)}{dt^2}\int_{r}^{r+l}m_1(x)\gamma_{iG}(x)dx= \\ =T_{AG}(t)+T_{DG}(t)-T_{FG}(t); \quad (7)$$

$$J_{0T}\frac{d^2\psi(t)}{dt^2}-\sum_{i=1}^{n}\frac{d^2W_{iT}(t)}{dt^2}\int_{r}^{r+l}m_1(x)\gamma_{iT}(x)dx= \\ =T_{AT}(t)+T_{DT}(t)-T_{FT}(t); \quad (8)$$

$$m_1(x)\frac{d^2\varphi(t)}{dt^2}+m(x)\sum_{i=1}^{n}\gamma_{iG}(x)\frac{d^2W_{iG}(t)}{dt^2}+ \\ ++EI(x)\sum_{i=1}^{n}\frac{\partial^4\gamma_{iG}(x)}{\partial x^4}W_{iG}(t)+ \\ +\xi EI(x)\sum_{i=1}^{n}\frac{\partial^4\gamma_{iG}(x)}{\partial x^4}\frac{dW_{iG}(x)}{dt}=F_{0G}(x,t); \quad (9)$$

$$m_1(x)\frac{d^2\psi(t)}{dt^2}+m(x)\sum_{i=1}^{n}\gamma_{iT}(x)\frac{d^2W_{iT}(t)}{dt^2}+EI(x)\sum_{i=1}^{n}\frac{\partial^4\gamma_{iT}(x)}{\partial x^4}\dots \\ \dots W_{iT}(t)+\xi EI(x)\sum_{i=1}^{n}\frac{\partial^4\gamma_{iT}(x)}{\partial x^4}\frac{dW_{iT}(x)}{dt}=F_{0T}(x,t). \quad (10)$$

The control precision is largely determined only by the first form of tank gun barrel elastic oscillation. Taking into account only the first basic form of elastic oscillations in expression (5), (6) the function is represented

$$y_G(x,t)=\gamma_{0G}(x)W_{0G}(t); \quad (11)$$

$$y_T(x,t)=\gamma_{0T}(x)W_{0T}(t). \quad (12)$$

Then the equations of the dynamics of the electromechanical system as a discrete-continuous plant (7)–(12) in elevation and azimuth axes will take the following form

$$J_{0G}\frac{d^2\varphi(t)}{dt^2}-a_{0G}\frac{d^2W_{0G}(t)}{dt^2}=T_{AG}(t)+T_{DG}(t)-T_{FG}(t); \quad (13)$$

$$J_{0T}\frac{d^2\psi(t)}{dt^2}-a_{0T}\frac{d^2W_{0T}(t)}{dt^2}=T_{AT}(t)+T_{DT}(t)-T_{FT}(t); \quad (14)$$

$$a_{0G}\frac{d^2\varphi(t)}{dt^2}+c_{0G}\frac{d^2W_{0G}(t)}{dt^2}+\xi_G\,b_{0G}\frac{dW_{0G}(t)}{dt}+\dots \\ +b_{0G}W_{0G}(t)=f_{0G}(t); \quad (15)$$

$$a_{0T}\frac{d^2\psi(t)}{dt^2}+c_{0T}\frac{d^2W_{0T}(t)}{dt^2}+\xi_T\,b_{0T}\frac{dW_{0T}(t)}{dt}+\dots \\ +b_{0T}W_{0T}(t)=f_{0T}(t). \quad (16)$$

Coefficients a_{0G}, a_{0T}, c_{0G}, c_{0T} and b_{0G}, b_{0T} in equations (13)–(15) are obtained by substituting expression (5), (6) into equation (8), (9) multiplying both parts of the resulting equation by $\gamma_{0G}(x)$, $\gamma_{0T}(x)$ and integrating both parts of the equation in the range from r to $(r + l)$.

In the elevation and azimuth axes there are two types of external disturbance. The first type of external disturbance is related to the hull longitudinal angular oscillations. These disturbances cause a disturbance torques that acts on the gun and turret

$$M_{DG}=\mu_0\frac{d\varphi_H(t)}{dt}; \quad (17)$$

$$M_{DT}=\mu_0\frac{d\psi_H(t)}{dt}, \quad (18)$$

where μ_0 – constant coefficient, which is determined experimentally; $d\varphi_H(t)/dt$ and $d\psi_H(t)/dt$ – hull angular rate in elevation and azimuth axes.

The second type of external perturbation is associated with hull accelerations relative to its elevation axis. These accelerations, being annexed to the distributed masses of the gun, cause its elastic fluctuations. Distributed forces applied to the gun and turret and included in the equation of its elastic oscillations are determined by the following dependencies

$$F_{0G}(x,t)=m(x)\frac{d^2z_G(t)}{dt^2}; \quad (19)$$

$$F_{0T}(x,t)=m(x)\frac{d^2z_T(t)}{dt^2}, \quad (20)$$

where $m(x)$ – the weight of the gun elastic part; $d^2z_G(t)/dt^2$ and $d^2z_T(t)/dt^2$ – hull acceleration relative to its elevation and azimuth axes. Then we will get

$$f_{0G}(t)=\frac{d^2z_G(t)}{dt^2}\int_r^{r+l} m(x)\gamma_{1G}(x)dx=k_{zG}\frac{d^2z_G(t)}{dt^2}; \quad (21)$$

$$f_{0T}(t)=\frac{d^2z_T(t)}{dt^2}\int_r^{r+l} m(x)\gamma_{1T}(x)dx=k_{zT}\frac{d^2z_T(t)}{dt^2}. \quad (22)$$

External perturbations acting on the hull in the elevation and azimuth axes are to a large extent determined by the longitudinal angles and hull vertical and horizontal fluctuations. Note that using equations (16), (18) and (20), disturbing moments due to the tank turret imbalance are also taken into account. Using equations (15), (17) and (19), disturbing moments due to the tank gun imbalance are also taken into account.

With direct torque control (DTC) by a synchronous motors with permanent magnets (PMSM) [13] actuator torques $T_{AG}(t)$, $T_{AT}(t)$ motion equations can be written as follows [14, 15]

$$\tau\frac{dT_{AG}(t)}{dt}+T_{AG}(t)=K_{AG}U_{AG}(t); \quad (23)$$

$$\tau\frac{dT_{AT}(t)}{dt}+T_{AT}(t)=K_{AT}U_{AT}(t), \quad (24)$$

where $U_{AG}(t)$, $U_{AT}(t)$ – inputs control, τ – equivalent constant times and K_{AG}, K_{AT} – contour gains of DTC.

Method of synthesis. Let us write down the original turret and gun model (13) – (22) of the electromechanical system as a discrete-continuous plant taking into account the moles of the executive motors (23), (24), hull suspension effects and sensors as plant of robust control system with a state vector $x(t)$ in the standard form of a state equation

$$\frac{dx(t)}{dt}=f(x(t),u(t),\omega(t),\eta(t)), \quad (25)$$

where $u(t)$ is the control, $\omega(t)$ and $\eta(t)$ are the vectors of the external signal and parametric perturbations, f – is a nonlinear function.

The mathematical model (25) takes into account the nonlinear frictional dependencies on the shafts of the drive motor, the rotating parts of the reducer and the gun and turret, the gear gap between the teeth of the driving and driven gears, the constraints for control, current, torque and motor rate, as well as the plant moment of inertia.

In particular, the model of turnnion friction torques $T_F(t)$ of drive motor, reducer and plant adopted in the following form[7]:

$$T_F=\begin{cases} T, \text{ if } |T|\le T_s \text{ and } |\omega|<0.001; \\ \left(T_k+(T_s-T_k)\cdot e^{-(\omega/\omega_s)^{\delta}}\right)\cdot \text{sign}(\omega)+\nu\cdot\omega, \text{ if } |\omega|\ge 0.001, \end{cases}$$

where T_F – the moment of friction; T – the moment applied to the shaft that is cracking; T_s – moment of friction of rest (static friction); T_k – the moment of kinetic friction.

Measured output vector of the initial system

$$y(t)=Y(x(t),\omega(t),u(t)) \quad (26)$$

is formed by different sensors which measured the angular, rate and acceleration of turret, gun and hull in elevation and azimuth axes and placed at the turret, gun and at the hull [7].

The task of synthesis is the determination of such a regulator [16, 17] which, based on the measured output (26) forming control $u(t)$ using a dynamic system described by the difference state equation and output

$$\frac{d\xi(t)}{dt}=f(\xi(t),u(t),\omega(t),\eta(t))+\sum_{i=1}^{3}G_i(y(t)- \quad (27)$$
$$-Y(\xi(t),\omega(t),u(t));$$

$$u(t)=\sum_{i=1}^{3}U_i(\xi(t),y(t)), \quad (28)$$

where i is the order of the forms G_i and U_i.

The synthesis of the regulator (28) is reduced to determining the matrix of the forms of the regulator gain U_i by minimizing the norm of the target vector

$$z(x(t),u(t),\eta(t))=\sum_{i=2}^{4}Z_i(x(t),u(t),\eta(t)) \quad (29)$$

on control vector of $u(t)$ and maximization of the same norm on a of plant uncertain vector $\eta(t)$ for the worst case disturbance.

The synthesis of the observer (27) is reduced [18] to determining the observer gain coefficients G_i by minimization of the error vector of the recovery of the state vector $x(t)$ of the initial system (25) and maximization of the same norm of the error vector along the plant uncertainty vector $\eta(t)$ and the vector of external signal influences $\omega(t)$, which also corresponds to the worst case disturbance.

Matrices of the regulator U_i and observer G_i gain coefficients are found from approximate solutions of the Hamilton-Jacobi-Isaacs equations [18, 19], in which the matrices of linear forms being found from the four Riccati equations solutions. This approach corresponds to the standard 4-Riccati approach to the synthesis of linear robust or anisotropic regulators [19].

To determine the regulator (28) for plant (25) with target vector (29) consider Hamiltonian function

$$H(x(t),u(t),\eta(t))=+V_x^T(x(t),u(t),\eta(t))f(x(t),\ldots$$
$$\ldots u(t),\eta(t))+z^T(x(t),u(t),\eta(t))z(x(t),u(t),\eta(t))-\ldots \quad (30)$$
$$-\frac{1}{\gamma^2}\eta^T(t)\eta(t),$$

here V_x are partial derivatives with respect to the state vector $x(t)$ of the infinite-horizon performance functional (Lyapunov function), γ – weighting coefficient which determines the conservatism degree of the synthesized robust regulator

To determine the robust regulator (28) it is necessary to find the minimum norm of the target vector (29) along the control vector u_k and the maximum of this norm along the external perturbations vector η_k, which reduces to solving the minimax extremal problem of Hamiltonian function [16]

$$H^*(x(t)) = \min_{u(t)} \max_{\eta(t)} \{H(x(t), u(t), \eta(t))\}. \quad (31)$$

The necessary conditions for the extremum of the Hamiltonian function (31) both in the control vector u_k and in the external perturbation vector η_k are these equations

$$H_u\left(x(t), u^*(x(t)), \eta^*(x(t))\right) = 0; \quad (32)$$

$$H_\eta\left(x(t), u^*(x(t)), \eta^*(x(t))\right) = 0, \quad (33)$$

which are Hamilton-Jacobi-Isaacs equations. Here H_u and H_η are the partial derivatives of the Hamiltonian function with respect to the control vector $u(t)$ and with respect to the external perturbations vector $\eta(t)$.

Note that these equations (32), (33) are also necessary conditions for optimizing a dynamic game, in which the first player – the regulator which minimizes the target vector, and the second player – external disturbances which maximizes the same target vector.

The difficulty of obtaining a nonlinear control law is due to the fact that the difference Hamilton-Jacobi-Isaacs equations (32), (33) is a nonlinear partial differential equation. In this paper we use an approximate solution of the Hamilton-Jacobi-Isaacs equation (32), (33) assuming the analytical dependences of the nonlinearities of the original system (25), (26), (29) in the form of the corresponding series [19]. Then the linear approximation of the Hamilton-Jacobi-Isaac equation (32), (33) are the algebraic Riccati equations

$$A^T P + PA + P\left[\frac{1}{\gamma^2} B_\eta B_\eta^T - B_u B_u^T\right] P + C_z^T C_z = 0, \quad (34)$$

here, the matrices A, B_η, B_u, C_z in (34) are the corresponding matrices of the linear system obtained by linearizing the original nonlinear system (25), (26), (29).

Similarly matrices of the observer G_i gain coefficients (27) are found from approximate solutions of the Hamilton-Jacobi-Isaacs equations [18].

Feed forward control synthesis. When the tank was moving, the error of the stabilization system of tank armaments was caused by the action of disturbance torques $T_{DG}(t)$, $T_{DT}(t)$ that acts on the turret in the azimuth axis and on the gun in elevation axis from the side of the tank hull. Sensors that measure the hull angular position, hull angular rate, hull acceleration, etc in elevation and azimuth axes are mounted on the tank hull. These sensors can be used to observer disturbance torques $T_{DG}(t)$, $T_{DT}(t)$ and their derivatives and implement open-loop control to improve the accuracy of the tank weapon stabilization systems when firing on the move. We introduce the state vectors $x_{dG}(t)$, $x_{dT}(t)$ of the of external perturbation models, the components of which is the disturbance torques $T_{DG}(t)$, $T_{DT}(t)$ that acts on the turret in the azimuth axis and on the gun in elevation axis and its derivatives. We write the mathematical models of external disturbances in the following form

$$\frac{dx_{dG}(t)}{dt} = f_{dG}\left(x_{dG}(t), \omega_{dG}(t), \eta_{dG}(t)\right); \quad (35)$$

$$\frac{dx_{dT}(t)}{dt} = f_{dT}\left(x_{dT}(t), \omega_{dT}(t), \eta_{dT}(t)\right), \quad (36)$$

where $\omega_{dG}(t)$, $\omega_{dT}(t)$, $\eta_{dG}(t)$, $\eta_{dT}(t)$ are the vectors of the external signal and parametric perturbations [7, 8], f_{dG}, f_{dT} – are a nonlinear functions.

To realize the quasi invariant feed forward control by these disturbance torques $T_{DG}(t)$, $T_{DT}(t)$ in the plant model (25) also introduced the external disturbance models (35), (36).

Then with the help of the observer (27) the external disturbances torques $T_{DG}(t)$, $T_{DT}(t)$ and its derivatives also are observed [20] by measurement signals (26). Then the quasi-invariant feed forward control by external disturbances (35), (36) realize in form (28) by observer external disturbance state variables (27).

Multiobjective synthesis of nonlinear robust control. For tank main armament guidance and stabilization systems sufficiently stringent requirements are set for the performance indicators in various modes. In the guidance mode it is necessary to control by the gun rate and turret rate. In the stabilization mode it is necessary to control by the gun position and turret position. We bring a part of such performance indicators [7, 8]. Time of working out of a given angle of error. Acceleration time to rated speed and deceleration time to full stop. An error in working out a harmonic signal of a specified amplitude and frequency. Stabilization error when moving along a normalized path with a random profile change with a given speed. Maximum speed of guidance. Minimum speed of guidance. Failure of guidance at minimum speed. Naturally, this should take into account the voltage and current limitations of the anchor chain of the drive motor, as well as the speed of rotation of the drive motor.

Dynamic characteristics of synthesized system including a nonlinear plant (25) that is closed by a robust controller (26), (27) are determined by the control system model of the system (25), the parameters of the measuring devices (26) and the target vector (29). For the correct definition of the target vector (29), we introduce the vector of the unknown parameters $\chi = \{Z_i(x_k, u_k, \eta_k)\}$, the components of which are the required weight matrices of the norm $Z_i(x_k, u_k, \eta_k)$. We introduce the vector of the objective function

$$F(\chi) = [F_1(\chi), F_2(\chi) ... F_m(\chi)]^T, \quad (37)$$

in which the components $F_i(\chi)$ are direct quality indicators that are presented to the system in various modes of its operation such as the time of the first coordination, the time of regulation, overshooting, etc [7, 8].

To calculate the vectors objective function (37) and constraints on state variables and control, the initial nonlinear system (25), (26) is modeled by a closed synthesized nonlinear regulator (27), (28) in various modes of operation, with different input signals and for various values of the plant parameters [8]. This (37) multiobjective nonlinear programming problem [22, 23] is solved on the basis of multi-swarm stochastic multi-agent optimization algorithms from Pareto optimal solutions [22, 23].

Computer simulation results. Comprehensive research of dynamic characteristics and sensitivity to the plant parameters change of the electromechanical tank armament stabilization systems with synchronous motor

with permanent magnets taking into account the gun barrel elastic oscillations as a discrete-continuous plant with parametric uncertainty [8] with synthesized nonlinear robust regulators were conducted. As an example Fig. 1 shows state variables random processes implementation of the synthesized electromechanical tank gun stabilization systems in the elevation axis when the tank moves at a speed of 8 $m{\cdot}s^{-1}$ along a standard tank route. On Fig. 1 shows such state variables of a closed system: *a*) the angle $\varphi(t)$ of deviation between the axis of the object and the given direction, and *b*) its derivative $d\varphi(t)/dt$; *c*) the value of the function $W_{0G}(t)$ in the representation $y_G(x, t)$ of the function, which characterizes the deviation of the tank barrel axis points from its state in the elevation axis, which is not deformed, and *d*) actuator torque $T_{AG}(t)$.

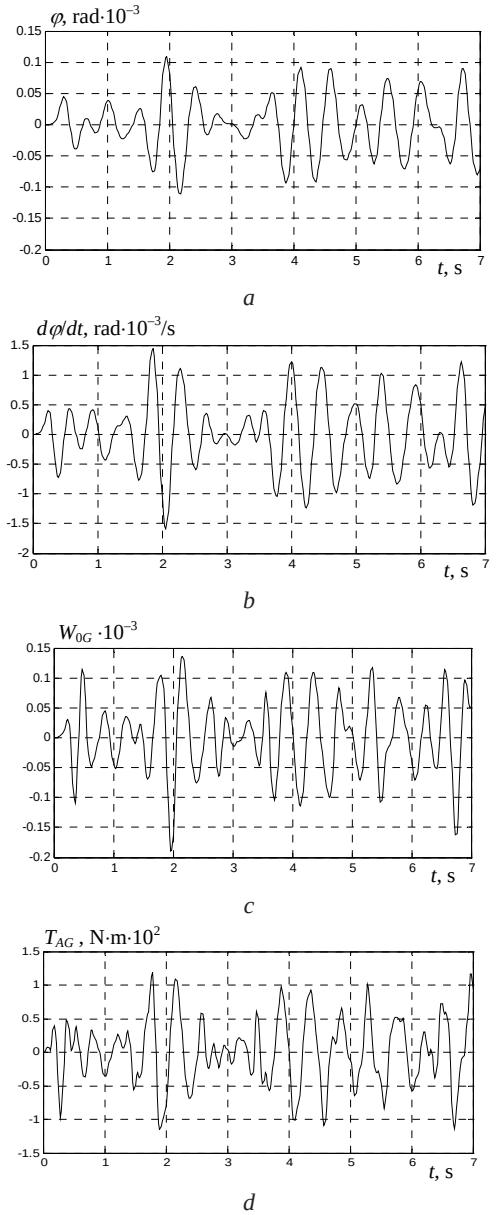

Fig. 1. State variables random processes implementation of the synthesized electromechanical tank gun stabilization systems in the elevation axis

As can be seen from Fig. 1.*d*, the actuator torques $T_{AG}(t)$ acting on the gun reaches 100 $N{\cdot}m$. The magnitude of disturbance torques $T_{DG}(t)$ acting on the gun, depends on the tank speed and the quality of the road surface. When moving along a mid-intersected area, these disturbance torques $T_{DG}(t)$ reach values 800 $N{\cdot}m$ [8]. With an increase the tank movement speed, the action of external disturbances gun weakens. This is explained by the fact that in the 4–6 $m{\cdot}s^{-1}$ movement speeds range, the resonant properties of the tank training system are manifested, and at speeds exceeding 8 $m{\cdot}s^{-1}$, the tank overcomes small effects, almost not responding to them. At the same time, with increased of the tank movement speed, the average frequency of oscillations of the function $F_{0G}(x, t)$ in (19) significantly increases, which reduces the accuracy of aimed shooting on the move.

As can be seen from this figure, the error of stabilization of a given angle of a tank gun is about 0.1 m*rad*, which is about 1.7 times less than the error of a system with a typical proportional-differential controller [2, 10] and corresponds to the «Leclerc» tank weapons stabilization system accuracy [10, 24].

During the simulation of the dynamic characteristics of the synthesized electromechanical tank armament stabilization systems, it was found that the use of nonlinear robust control made it possible to reduce the time spent on working out the initial angular mismatch of 0.1 *rad* between guns and targets directions. When the plant inertia moment was changed by 30 %, the mining time was changed by less than 10 % while maintaining the level of overregulation, while in the system with a typical regulator, the mining time was changed to 30 % with a significant change in the system overshoot. Thus, the use of nonlinear robust controllers also made it possible to reduce the sensitivity of the system to changes in the parameters of the control object as compared to the existing system.

Conclusions.

1. For the first time the method of multiobjective synthesis of nonlinear robust control by electromechanical tank armament stabilization systems with synchronous motor with permanent magnets taking into account the gun barrel elastic oscillations as a discrete-continuous plant and tank turret imbalance and with parametric uncertainty is developed.

2. Synthesis of nonlinear robust regulators and nonlinear robust observers reduces to solving the system of Hamilton-Jacobi-Isaacs equations. Robust control target vector is determined by solving the multi criterion nonlinear programming problem in which the components of the vectors of the objective function are direct quality indicators that are presented to the system in various modes of its operation.

3. Based on the computer model dynamic characteristics analysis of the synthesized electromechanical tank armament stabilization systems with synchronous motor with permanent magnets as a discrete-continuous plant shown that the use of synthesized nonlinear robust regulators made it possible to reduce by 1.7 times the error of stabilization of a given angular position of a tank gun when moving the tank, reduce by 1.8–2 times the time spent working off the initial angular misalignment of

0.1 *rad* between the gun and target directions, reduce by 20 % the system sensitivity to plant parameters changes in comparison with the existing system with standard proportional-differential regulator.

4. The results of the synthesis of electromechanical tank armament stabilization systems with synchronous motor with permanent magnets are recommended for use in the modernization of the T-64 tanks family.

REFERENCES

1. Chernyshev V.L., Tarasenko A.A., Ragulin S.V. Comparative evaluation of tactical and technical and structural parameters of T-64B tanks (BM «Bulat») and Leopard-2A4. Available at: http://btvt.narod.ru/raznoe/bulat-leo2.htm (accessed 05 May 2018). (Rus).

2. Koshelev V.V., Lavrishchev B.P., Sokolov V.Ya., Potemkin E.K., Prutkov V.N. Accuracy of complexes of tank-army armament according to military test data. *Bulletin of armored vehicles*, 1985, no.4, pp. 58-24. (Rus).

3. Features of the upgraded tanks T-64BV of Armed Forces of Ukraine. Available at: https://diana-mihailova.livejournal.com/2524539.html (accessed 14 July 2018). (Rus).

4. M1 Abrams Main Battle Tank 1982-1992. New Vanguard 2. – Osprey Publishing (UC), 1993. 49 p.

5. Challenger 2 Main Battle Tank 1987-2006. New Vanguard 112. – Osprey Publishing (UC), 2006. 49 p.

6. Merkava – A History of Israel's Main Battle Tank. Marsh Gelbart. Tankograd Publishing-Vertag Jochen Vollert, Germany, 2005. 175 p.

7. Closed-loop optimization program for the M60A1 tank gun stabilization system. W. Binroth, Rock Island Arsenal, 1975. 251 p.

8. Aleksandrov E., Bogaenko I., Kuznetsov B. *Parametric synthesis of tank weapon stabilization systems*. Kyiv, Tehnika Publ., 1997. 112 p. (Rus).

9. *All Electric Combat Vehicles (AECV) for Future Applications*. Report of The Research and Technology Organization (RTO) of NATO Applied Vehicle Technology Panel (AVT) Task Group AVT-047 (WG-015), 2004. 234 p.

10. Eliseev A.D. Main directions of development of modern tank armament stabilizers. *News of the Tula state university. Technical sciences*, 2012, iss.11, part 2, pp. 3-9. (Rus).

11. Shamarih O.V. Electromechanical stablizers of tank armaments. *Bulletin of armored vehicles*, 1985, no.1, pp. 23-26.

12. Kozyrev V.V. Ways and prospects for improving the stabilizers of tank-water weapons. *Defense equipment*, 2005, no.2-3, pp. 65-71.

13. Peresada S., Kovbasa S., Korol S., Zhelinskyi N. Feedback linearizing field-oriented control of induction generator: theory and experiments. *Technical Electrodynamics*, 2017, no.2, pp. 48-56. (Rus). **doi: 10.15407/techned2017.02.048.**

14. Buriakovskyi S., Maslii A., Maslii A. Determining parameters of electric drive of a sleeper-type turnout based on electromagnet and linear inductor electric motor. *Eastern-European Journal of Enterprise Technologies*, 2016, vol.4, no.1(82), pp. 32-41. (Rus). **doi: 10.15587/1729-4061.2016.75860**.

15. Rozov V.Yu., Reutskyi S.Yu., Pelevin D.Ye., Pyliugina O.Yu. The magnetic field of transmission lines and the methods of its mitigation to a safe level. *Technical Electrodynamics*, 2013, no. 2, pp. 3-9. (Rus).

16. William McEneaney M. *Max-plus methods for nonlinear control and estimation*. BirkhaËuser Boston Basel Berlin, 2006. 256 p.

17. Wilson Rugh J. *Nonlinear System Theory. The Volterra. Wiener Approach*. The Johns Hopkins University Press, 2002. 330 p.

18. Tolochko O. Analysis of observed-based control systems with unmeasured disturbance. *2017 IEEE First Ukraine Conference on Electrical and Computer Engineering (UKRCON)*, May 2017. **doi: 10.1109/ukrcon.2017.8100402**.

19. Kuznetsov B.I., Nikitina T.B., Tatarchenko M.O., Khomenko V.V. Multicriterion anisotropic regulators synthesis by multimass electromechanical systems. *Technical Electrodynamics*, 2014, no.4, pp. 105-107. (Rus).

20. Galchenko V.Ya., Yakimov A.N. A Turmitobionic Method for the Solution of Magnetic Defectometry Problems in Structural-Parametric Optimization Formulation. *Russian Journal of Nondestructive Testing*, 2014, vol.50, no.2, pp. 59-71. **doi: 10.1134/s106183091402003x**.

21. Xin-She Yang, Cui Zhihua, Xiao Renbin, Amir Hossein Gandomi, Mehmet Karamanoglu. *Swarm Intelligence and Bio-Inspired Computation: Theory and Applications*. Elsevier Inc., 2013. 450 p. **doi: 10.1016/C2012-0-02754-8**.

22. Gal'chenko V.Y., Yakimov A.N., Ostapushchenko D.L. Pareto-optimal parametric synthesis of axisymmetric magnetic systems with allowance for nonlinear properties of the ferromagnet. *Technical Physics*, 2012, vol.57, no.7, pp. 893-899. **doi: 10.1134/s1063784212070110**.

23. Shoham Y., Leyton-Brown K. *Multiagent Systems: Algorithmic, Game-Theoretic, and Logical Foundations*. Cambridge University Press, 2009. 504 p. **doi: 10.1017/CBO9780511811654.**

24. Gun turret drives: Electric stabilization systems for military ground vehicles. Available at: https://www.jenoptik.com/products/defense-and-security/stabilization-systems/gun-turret-drives (accessed 11 August 2018).

Received 27.11.2018

B.I. Kuznetsov[1], *Doctor of Technical Science, Professor,*
T.B. Nikitina[2], *Doctor of Technical Science, Professor,*
I.V. Bovdui[1], *Candidate of Technical Science,*
B.B. Kobilyanskiy[1], *Candidate of Technical Science, Associate Professor,*
[1] State Institution «Institute of Technical Problems of Magnetism of the NAS of Ukraine»,
19, Industrialna Str., Kharkiv, 61106, Ukraine,
phone +380 50 5766900,
e-mail: kuznetsov.boris.i@gmail.com
[2] Kharkov National Automobile and Highway University,
25, Yaroslava Mudroho Str., Kharkov, 61002, Ukraine,
e-mail: tatjana55555@gmail.com

How to cite this article:
Kuznetsov B.I., Nikitina T.B., Bovdui I.V., Kobilyanskiy B.B. Improving of electromechanical stabilization systems accuracy. *Electrical engineering & electromechanics*, 2019, no.2, pp. 21-27. **doi: 10.20998/2074-272X.2019.2.04.**

UDC 620.179.147:519.853.6 **doi: 10.20998/2074-272X.2019.2.05**

V.Ya. Halchenko, R.V. Trembovetska, V.V. Tychkov

DEVELOPMENT OF EXCITATION STRUCTURE RBF-METAMODELS OF MOVING CONCENTRIC EDDY CURRENT PROBE

Introduction. *The work is devoted to metamodels creation of surface circular concentric eddy current probe.* ***Formulation of the problem.*** *In the problem of surface circular concentric eddy current probe synthesis in the general formulation, apriori given desired eddy currents density distribution in the control zone was used. The realization of the optimal synthesis problem involves a multiple solution to the analysis problem for each current structure of numerical calculations excitation, which are very costly in terms of computational and time costs, which makes it impossible to solve the synthesis problem in the classical formulation. By solving the critical resource intensiveness problem, there is the surrogate optimization technology using of that uses the surface circular concentric eddy current probe metamodel, which is much simpler in realization and is an approximation of the exact electrodynamic model.* ***Goal.*** *Creation of surface circular concentric eddy current probe RBF-metamodels, which can be used to calculate eddy currents density distribution in the control zone and suitable for use in optimal synthesis problems.* ***Method.*** *To develop an approximation model, a mathematical apparatus for artificial neural networks, namely, RBF–networks, has been used, whose accuracy has been increased with the help of the neural networks committee. Correction of errors in the committee was reduced by applying the bagging procedure. During the network training the regularization technique is used, which avoids re-learning the neural network. The computer experiment plan was performed using the Sobol LPτ–sequences. The obtained multivariable regression model quality evaluation was performed by checking the response surface reproducibility correctness in the entire region of variables variation.* ***Results.*** *The modelling of eddy currents density distribution calculations on exact electrodynamic mathematical models in the experimental plan points are carried out. For the immovable and moving surface circular concentric eddy current probe, RBF–metamodels were constructed with varying spatial coordinates and radius.* ***Scientific novelty.*** *Software was developed for eddy currents density distribution calculation in the surface circular concentric eddy current probe control zone taking into account the speed effect on exact electrodynamic mathematical models and for forming experiment plan points using the Sobol LPτ–sequences. The geometric surface circular concentric eddy current probe excitation structures models with homogeneous sensitivity for their optimal synthesis taking into account the speed effect are proposed. Improved computing technology for constructing metamodels. The RBF-metamodels of the surface circular concentric eddy current probe are built and based on the speed effect.* ***Practical significance.*** *The work results can be used in the surface circular concentric eddy current probe synthesis with an apriori given eddy currents density distribution in the control zone.* References 22, tables 6, figures 8.

Key words: **surface eddy current probe, eddy currents density distribution, excitation structure, mathematical model, optimal synthesis, computer experiment plan, LPτ–sequence, RBF–metamodel, neural networks committee**.

Розроблено програмне забезпечення для розрахунку розподілу густини вихрових струмів в зоні контролю накладного вихрострумового перетворювача із врахуванням ефекту швидкості за «точними» електродинамічними математичними моделями. Розроблено програмне забезпечення для формування точок плану експерименту із використанням ЛП$_\tau$–послідовностей, що дозволило здійснювати відбір планів з рівномірним заповненням точками гіперпростору пошуку. Для нерухомого та рухомого накладних вихрострумових перетворювачів створено нейромережеві метамоделі на радіально-базисній функції Гауса. Оцінено адекватність та інформативність отриманих метамоделей накладних вихрострумових перетворювачів. Результати дослідження можуть бути використані при синтезі рухомих накладних вихрострумових перетворювачів із апріорі заданим розподілом густини вихрових струмів в зоні контролю. Бібл. 22, табл. 6, рис. 8.

Ключові слова: **накладний вихрострумовий перетворювач, розподіл густини вихрових струмів, структура збудження, математична модель, оптимальний синтез, комп'ютерний план експерименту, ЛП$_\tau$–послідовність, RBF–метамодель, комітет нейронних мереж.**

Разработано программное обеспечение для расчета распределения плотности вихревых токов в зоне контроля накладного вихретокового преобразователя с учетом эффекта скорости по «точным» электродинамическим математическим моделям. Разработано программное обеспечение для формирования точек плана эксперимента с использованием ЛПτ-последовательностей, что позволило осуществлять отбор планов с равномерным заполнением точками гиперпространства поиска. Для неподвижного и движущегося накладных вихретоковых преобразователей созданы нейросетевые метамодели на радиально-базисной функции Гаусса. Оценены адекватность и информативность полученных метамоделей накладных вихретоковых преобразователей. Результаты исследования могут быть использованы при синтезе движущихся накладных вихретоковых преобразователей с априори заданным распределением плотности вихревых токов в зоне контроля. Библ. 22, табл. 6, рис. 8.

Ключевые слова: **накладной вихретоковый преобразователь, распределение плотности вихревых токов, структура возбуждения, математическая модель, оптимальный синтез, компьютерный план эксперимента, ЛПτ–последовательность, RBF–метамодель, комитет нейронных сетей**.

Introduction. The eddy current control method and the devices on its basis are widely used to determine the parameters of various objects of control (OC): imperfect material defects, control of the dimensions of the OC and vibration parameters, quality control of thermal and chemical-thermal processing of parts, the state of surface layers after machining, the presence of residual mechanical stresses, the reconstruction of the distribution of electrical conductivity and the magnetic permeability within the objects, and others.

Along with the significant advantages of the eddy current control method, there are some disadvantages, for example, the ability to control only the conductive objects, the relatively small depth of the eddy currents penetration, the heterogeneous sensitivity of the probes of classical design.

The typical surf ace eddy current probes (SECP) are characterized by a characteristic distribution of the eddy currents density (ECD) in the OC, which depends on the geometrical, electromagnetic parameters and the relative position of its exciting coil relative to the controlled surface. In SECP, the ECD is maximal in the surface layer of the conductive object and decreases at the removal from the excitation coil windings along the surface (Fig. 1,*a*) and in deeper layers according to the exponential law. That is, in such a heterogeneous distribution of the ECD (Fig. 1,*a*), the relative position of the SECP with respect to the OC significantly influences the sensitivity of the method. In the defectoscopy, for example, in the case where a surface fracture of a finite length is located under the geometric center of the excitation coil, the sensitivity will be close to zero (Fig. 1,*c*), the minimum sensitivity is observed for the case of the location of the surface crack in parallel to the vortex currents (Fig. 1,*d*) and the maximum one – if the crack is perpendicular to the direction of eddy currents (Fig. 1,*e*).

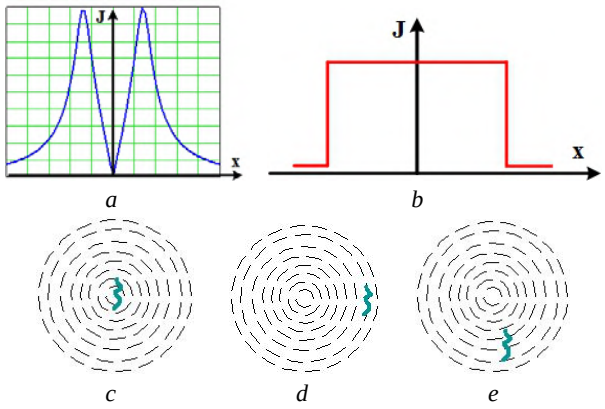

Fig. 1. Features of the SECP: distribution of ECD, inherent in classical designs of probes (*a*); uniform distribution of ECD (*b*); sensitivity close to zero (*c*); minimum sensitivity (*d*); maximum sensitivity (*e*)

In order to reduce the effect of the dependence of the sensitivity of the probes to the defect, regardless of its location in the control zone, it is desirable to have the distribution of the ECD in it homogeneous (Fig. 1,*b*). The problem arises of the creation of the SECP with homogeneous sensitivity, and, consequently, a homogeneous distribution of the ECD in the control zone of the object. This problem can be solved within the framework of optimal synthesis as a result of determining the rational structure of the excitation system of the SECP with the corresponding parameters that provide the necessary distribution of the ECD. It is also important to achieve homogeneous sensitivity of the SECP which are not only stationary relative to the OC or move at a low speed, when the effect of the transfer currents can be neglected, but also for mobile probes.

Literature review. In [1], the problems of linear synthesis of a fixed SECP are considered, where the dependence of the output signal on the gap or the specific electrical conductivity of the investigated object is taken as the initial data. In order to solve an incorrect synthesis problem, the method of regularization is applied, i.e. certain restrictions were introduced on the desired functions. In [2] the questions of linear synthesis of a fixed SECP are considered. The plane of the control zone is parallel to the working face of the probe, where a given magnetic field structure was created. In [3] an algorithm for nonlinear synthesis of magnetic fields of excitation of a fixed SECP with a predefined configuration is presented. The solution of the problem is obtained by minimizing the average stepped approximation of the minimax functional, which provides the minimum deviation of the desired distribution of the electromagnetic field from the given one. In the paper [4] a structural-parametric synthesis of the excitation system of a fixed SECP is performed. The searched parameters are the number of sections, their radii and coordinates. The search for an optimal solution is performed using a genetic algorithm. The optimum values of the parameters of the coil sections, as well as the most constructively simple excitation system that provide the given distribution of the probe field in space, are obtained. Significant improvement of the quality of the generated field of the synthesized magnetic system, the essential simplification of the structure by the number of sections and the reduction of the length of the system, as well as reduced number of turns in sections at the same values of currents have been achieved. In [5] a methodology for optimizing the design of a coil of an eddy current probe (ECP) is proposed, which allows maximum approximation to the ideal excitation field in the multi-purpose statement of the problem. The research presents a method for optimizing the design of the excitation system to obtain a tangential and uniform distribution of multilinear eddy currents. In [6], a method for optimizing the parameters of an excitation coil was developed by solving a multi-parameter multi-purpose optimization problem. The imitation modeling of the behavior of an infinite coil with a tangential uniform field on the surface of the OC is carried out. As a result, a non-uniform multilayer design of the ECP coil has been obtained, which provides a uniform field of excitation. In [7], a genetic algorithm for solving the optimization problem of selecting the parameters of the ECP excitation field was used. For the excitation coil of the probe, the optimal values of frequency and size are obtained.

Thus, previously published studies devoted to the questions of synthesis of ECP [1-7] with a given configuration of the probe field in the control zone, considered the fixed OC and did not take into account the reaction of the conductive medium. It was enough to create a system of excitation of the SECP with a uniform distribution of the electromagnetic field, which was guaranteed to ensure a uniform distribution of the ECD in the OC. The account of the speed effect involves the synthesis of a homogeneous distribution of the ECD in the environment of the OC, which is a fundamental difference from the results of previous studies and can not be carried out by the means previously proposed.

The goal and objectives of the study. *The object of the study* is the processes of eddy current control of the

quality of objects. *The subject of research* is a mobile circular SECP with a homogeneous distribution of the ECD in the control zone. *The goal of the work* is to create a RBF-metamodel for a mobile concentric circular SECP that can be used to calculate the distribution of the ECD in the control area and be suitable for use in optimal synthesis problems.

Mathematical model of the mobile SECP. As the initial input data for designing in the problem of synthesis of the SECP in the general formulation a priori given the desired distribution of the ECD $J_{reference}$ in the control zone is used. For the purpose of some simplification of the problem, we restrict ourselves first by obtaining this distribution of the ECD on the surface of the OC, specifying certain values of the ECD in the set of N control points Q.

The structure of the excitation of the SECP consists of a system of M coils of varying height of position z_{0k}, $k = 1…M$ of the corresponding coil relative to the OC and radii r_k. The circuit of their connection is counter or coherent, and the supply current I can be the same or different for each of the coils. As an option of the structure of excitation, Fig. 2,*a* shows a system of concentric coils with different radii which is located at the same height z_0 over OC. Fig. 2,*b* shows the excitation system of coils of different radii, which are located at the same height, with the centers of the coils shifted, that is, the coils are not concentric. Fig. 2,*c* shows a system of coils with different radii, which are located at different heights and with the displacement of the centers of one relative to the other.

In [8-13] a mathematical model of a single excitation coil of the SECP was developed, which allows to determine the distribution of the ECD in the OC, which we agree to call «accurate». For this, the following assumptions were made: the medium is linear, homogeneous, isotropic; the OC is mobile, conductive, of infinite width and length and has a finite thickness d; the coil is excited by alternating current I of frequency ω; the conductor of the coil is represented as infinitely thin; the electrical conductivity σ, the relative magnetic permeability μ_r and the speed of the probe $\vec{\upsilon} = (\upsilon_x, \upsilon_y, 0)$ are constant. In accordance with this mathematical model, three calculated areas are considered in which the complex values of magnetic flux density are determined:

- in the area $0 < z < z_0$

$$\vec{B}_1 = \vec{B}_i + \vec{B}_r,$$
$$\vec{B}_i = \operatorname{rot}\vec{A}_i, \quad \vec{A}_i = \frac{\mu_0}{4\pi}\int_l \frac{\vec{J}\,\mathrm{d}l}{R}, \qquad (1)$$
$$\Delta\vec{B}_r = 0, \quad \operatorname{rot}\vec{B}_r = 0,$$

where $\vec{B}_i$ describes the own magnetic field of a turn of length l and current density $\vec{J}$, and $\vec{B}_r$ is the magnetic field of eddy currents induced in the medium of the OC;

- in the area $-d < z < 0$

$$\Delta\vec{B}_2 - \sigma\cdot\mu\cdot\mu_0\cdot\left(\upsilon_x\cdot\frac{\partial\vec{B}_2}{\partial x} + \upsilon_y\cdot\frac{\partial\vec{B}_2}{\partial y}\right) - j\cdot\omega\cdot\sigma\cdot\mu\cdot\mu_0\cdot\vec{B}_2 = 0, \qquad (2)$$

$\operatorname{div}\vec{B}_2 = 0$;

- in the area $z < -d$

$$\Delta\vec{B}_3 = 0, \ \operatorname{rot}\vec{B}_3 = 0. \qquad (3)$$

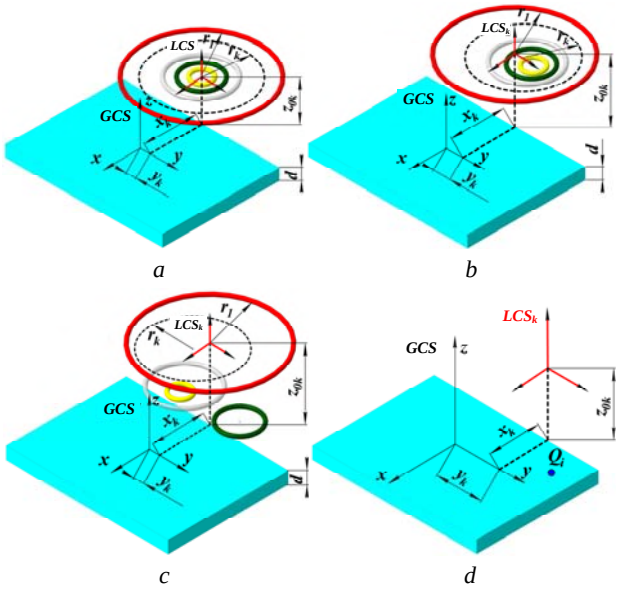

Fig. 2. Geometric models of SECP excitation structures: a system of concentric coils, where the coils are located at the same height z_0 (*a*); a system of coils where the coils are located at one height z_0, the centers of the coils shifted (*b*); a system of coils, where the coils are located at different heights, the centers of the coils shifted (*c*); general location of global and local coordinate systems of coils (*d*)

The solution of the system of equations (1)-(3) in conjunction with the conditions of continuity of the tangential component of the magnetic field strength and the normal component of magnetic flux density on the boundaries of the media interfaces $z = 0$ and $z = -d$, allows to obtain the distribution of components of the magnetic flux density in the medium of the OC:

$$B_{2x} = \frac{\mu_0\cdot\mu_r\cdot I}{8\cdot\pi^2}\cdot\int_{-\infty}^{\infty}\int_{-\infty}^{\infty}\frac{\xi}{\eta\cdot\left(1-e^{2\cdot\gamma\cdot d}\right)}\times$$
$$\times\left[\left\{-(1+\lambda_0)\cdot e^{2\cdot\gamma\cdot d} + \nu_0\cdot e^{\left(\gamma-\sqrt{\xi^2+\eta^2}\right)\cdot d}\right\}\cdot e^{\gamma\cdot z} + \right. \qquad (4)$$
$$\left. + \left\{1+\lambda_0 - \nu_0\cdot e^{\left(\gamma-\sqrt{\xi^2+\eta^2}\right)\cdot d}\right\}\cdot e^{-\gamma\cdot z}\right]\times$$
$$\times e^{-z_0\cdot\sqrt{\xi^2+\eta^2}}\cdot S(\xi,\eta)\cdot e^{-j(x\cdot\xi+y\cdot\eta)}\,d\xi\,d\eta;$$

$$B_{2y} = \frac{\mu_0\cdot\mu_r\cdot I}{8\cdot\pi^2}\cdot\int_{-\infty}^{\infty}\int_{-\infty}^{\infty}\frac{1}{\left(1-e^{2\cdot\gamma\cdot d}\right)}\times$$
$$\times\left[\left\{-(1+\lambda_0)\cdot e^{2\cdot\gamma\cdot d} + \nu_0\cdot e^{\left(\gamma-\sqrt{\xi^2+\eta^2}\right)\cdot d}\right\}\cdot e^{\gamma\cdot z} + \right. \qquad (5)$$
$$\left. + \left\{1+\lambda_0 - \nu_0\cdot e^{\left(\gamma-\sqrt{\xi^2+\eta^2}\right)\cdot d}\right\}\cdot e^{-\gamma\cdot z}\right]\times$$
$$\times e^{-z_0\cdot\sqrt{\xi^2+\eta^2}}\cdot S(\xi,\eta)\cdot e^{-j(x\cdot\xi+y\cdot\eta)}\,d\xi\,d\eta;$$

$$B_{2z} = j \cdot \frac{\mu_0 \cdot \mu_r \cdot I}{8 \cdot \pi^2} \cdot \int_{-\infty}^{\infty} \int_{-\infty}^{\infty} \frac{\xi^2 + \eta^2}{\eta \cdot \gamma \cdot \left(1 - e^{2 \cdot \gamma \cdot d}\right)} \times$$
$$\times \left[\left\{ -\left(1 + \lambda_0\right) \cdot e^{2 \cdot \gamma \cdot d} + \nu_0 \cdot e^{\left(\gamma - \sqrt{\xi^2 + \eta^2}\right) \cdot d} \right\} \cdot e^{\gamma \cdot z} - \right.$$
$$\left. - \left\{ 1 + \lambda_0 - \nu_0 \cdot e^{\left(\gamma - \sqrt{\xi^2 + \eta^2}\right) \cdot d} \right\} \cdot e^{-\gamma \cdot z} \right] \times \quad (6)$$
$$\times e^{-z_0 \cdot \sqrt{\xi^2 + \eta^2}} \cdot S(\xi, \eta) \cdot e^{-j(x \cdot \xi + y \cdot \eta)} d\xi d\eta,$$

where B_{2x}, B_{2y}, B_{2z} are the components of the magnetic flux density by spatial coordinates; $S(\xi,\eta)$ is the function of the shape of the coil,

$$S(\xi, \eta) = -j \cdot \frac{2 \cdot \pi \cdot r \cdot \eta}{\sqrt{\xi^2 + \eta^2}} \cdot J_1\left(r \cdot \sqrt{\xi^2 + \eta^2}\right);$$

$$\gamma = \sqrt{\begin{matrix} \xi^2 + \eta^2 - j \cdot \sigma \cdot \mu_0 \cdot \mu_r \cdot \left(\upsilon_x \cdot \xi + \upsilon_y \cdot \eta\right) + \\ + j \cdot \omega \cdot \sigma \cdot \mu_0 \cdot \mu_r \end{matrix}};$$

$$\lambda_0 = \frac{\left\{\gamma^2 - \mu_r^2 \cdot \left(\xi^2 + \eta^2\right)\right\} \cdot \left(1 - e^{-2 \cdot \gamma \cdot d}\right)}{\left(\gamma + \mu_r \cdot \sqrt{\xi^2 + \eta^2}\right)^2 - \left(\gamma - \mu_r \cdot \sqrt{\xi^2 + \eta^2}\right)^2 \cdot e^{-2 \cdot \gamma \cdot d}};$$

$$\nu_0 = \frac{4 \cdot \mu_r \cdot \gamma \cdot \sqrt{\xi^2 + \eta^2} \cdot e^{\left(\sqrt{\xi^2 + \eta^2} - \gamma\right) \cdot d}}{\left(\gamma + \mu_r \cdot \sqrt{\xi^2 + \eta^2}\right)^2 - \left(\gamma - \mu_r \cdot \sqrt{\xi^2 + \eta^2}\right)^2 \cdot e^{-2 \cdot \gamma \cdot d}},$$

where υ_x, υ_y are the components of the velocity of the circular SECP relative to the OC; d is the OC thickness; ξ, η are the variables of integration.

These expressions are adequate in the local coordinate system (LCS), where the origin of the coordinates coincides with the center of the turn. Multiple non-proper integrals of the first kind, which they contain, are calculated numerically by the truncation method.

Expressions (4) – (6) allow to obtain an «exact» mathematical model of the distribution of the ECD in the OC for the circular SECP. The components of the ECD by spatial coordinates x, y, z are respectively determined by the formulas:

$$J_x = \frac{1}{\mu_0 \cdot \mu_r} \cdot \left[\frac{\partial B_{2z}}{\partial y} - \frac{\partial B_{2y}}{\partial z} \right];$$
$$J_y = \frac{1}{\mu_0 \cdot \mu_r} \cdot \left[\frac{\partial B_{2x}}{\partial z} - \frac{\partial B_{2z}}{\partial x} \right]; \quad (7)$$
$$J_z = \frac{1}{\mu_0 \cdot \mu_r} \cdot \left[\frac{\partial B_{2y}}{\partial x} - \frac{\partial B_{2x}}{\partial y} \right].$$

The coordinates of the control points Q_i, $i = 1…N$ are specified in the global coordinate system (GCS), then they are recalculated to the k-th LCS. In the LCS, the ECD calculation is performed at each control point, and then the resulting values are obtained as a superposition at each point $i = 1…N$ from all M coils (Fig. 2,*d*).

In the general case, the objective function for the problem of optimal synthesis in the classical formulation has the form:

$$F_{target} = \sum_{i=1}^{N} \left(\sum_{k=1}^{M} J_{ik} - J_{reference} \right)^2 \rightarrow \min, \quad (8)$$

where $J_{reference}$ is the desired value of the eddy current currents at the control point; J_{ik} is the density of the eddy current in the control point of the OC with the number i, created by the k-th coil of the excitation system of the SECP; N is the number of control points in the area; M is the number of coils in the system of excitation of the circular SECP. As a result of the synthesis, the spatial configuration and geometric parameters of the structure of excitation of the SECP are obtained, which collectively provide the implementation of the required characteristics. The realization of the problem of optimal synthesis involves a multiple solution to the problem of analysis for each current structure of excitation by numerical calculations. In [14, 15] it is established that calculations on these expressions are very costly in terms of computational and time costs, which makes it impossible to solve the problem of synthesis.

One of the solutions of the problem of critical resource intensity is the use of surrogate optimization technologies [16, 17] and stochastic meta-heuristic optimization [18, 19]. That is, for the purpose of formulating the goal function within the framework of the optimal synthesis problem, a SECP metamodel can be used, which is much simpler in implementation and less resource-intensive [14, 15] and is an approximation of the «exact» electrodynamic model.

To achieve this goal, the following tasks were solved: creation of software for calculating the distribution of the ECD in the control zone of the SECP taking into account the effect of speed by «exact» electrodynamic mathematical models; creation of software for forming points of an experiment plan using the Sobol LPτ–sequences to select the most perfect experimental plans individually for the approximated surfaces of the response; to create geometrical models of excitation structures of circular SECPs with homogeneous sensitivity for their optimal synthesis taking into account the effect of speed; to improve the computational method of constructing metamodels of objects that are characterized by considerable computational resource intensities in the simulation of physical processes; to create RBF-metamodels of the concentric circular SECP (fixed one and taking into account the effect of speed).

To calculate the «exact» electrodynamic mathematical models (4) – (7), software was developed in the MathCAD 15 package.

The calculation of the distribution of the ECD for the turn of the excitation coil of the circular shape in order

to visualize it was performed for the case of variation of the two parameters $J = f(x, y)$ (Fig. 2,*a*) and the other fixed ones by the formulas (4) – (7) of the «exact» mathematical models with the following input data: for the case of a fixed SECP –x = 0…30 mm, y = 0…30 mm, r = 5 mm; for the case of a moving SECP – υ = (40; 0; 0) m/s; x = –30…30 mm, y = 0…30 mm, r = 5, 10, 15 mm; thickness of the conductive material d = 10 mm; height of the placement turn of the coil over OC z_0 = 3 mm; frequency f = 100 Hz; electrophysical parameters of the material $\sigma = 3.745 \cdot 10^7$ S/m, μ_r = 1, current I = 1 A.

Fig. 3,*a*-*h* show the 3D distribution of the ECD and the level lines for some excitation coil turns radiuses. For example, Fig. 3,*a*,*b* show the simulation results for a fixed SECP, and Fig. 3,*c*-*h* present the results of calculating the distribution of the ECD taking into account the effect of speed.

The computational complexity of a one-time calculation of the ECD distribution by an «exact» mathematical model with variations of only two spatial coordinates $J = f(x, y)$ at r = const is sufficiently large and ranges from 5 to 8 hours.

Main points and development of metamodels. In [14, 17], the authors proposed a general computational method for constructing metamodels using modern achievements in the field of artificial intelligence and the theory of experiment planning. A number of examples have proved the effectiveness of its use. Neural networks have been used to construct a substitute model, which provide the ability to quickly and easily calculate the output of the network, even with a sufficiently large number of neurons in hidden layers. In [15, 16] some features of the application of this technology in relation to the problems of the synthesis of the SECP are considered. Below, attention is focused on the details of the construction of metamodels of the circular SECP with certain structures of the excitation system, namely, the variant illustrated in Fig. 2,*a*, that is, approximation $\hat{J} = f(x, y, r)$.

In contrast to the previous studies of authors, increasing the accuracy of the neural network solution of approximation problems was achieved with the help of the neural networks committee [20]. The committee makes the final decision using separate solutions of several neural networks, that is, the method of bagging. Thus, the bagging committee is used to reduce the correlation of neural network errors. This methodology involves training neural networks on bootstrap-samples, which represent a set of elements with repetitions from a previous training set of data. Bagging provides the most effectiveness in the case of a fairly large number of input training data. Thus, for the construction of an approximation model, the mathematical apparatus of artificial neural networks was used namely the bagging committee of RBF-networks with the Gaussian activation core function.

The creation of a metamodel involves the construction of a computer experiment plan, at which points the distribution of the ECD is calculated by the «exact» mathematical model, the construction of an approximation model and validation of the model.

The experiment plan is implemented with the help of uniform computer filling by the points of the 3D search space, namely, using the Sobol LPτ–sequences [21]. The points of the experiment plan are generated using LPτ–sequences (ζ_1, ζ_2, ζ_4) and their total number is: for the case of a fixed SECP – N = 2048 and N = 3315 – for a moving SECP. For each section of the surface by the radius there is approximately N_{cut} = 146 and N_{cut} = 255 points, respectively.

The obtained ECD values at the points of the plan are used as the initial data for the implementation of the next stage – construction of the metamodel. The number of points of calculation essentially depends on the symmetry of the distribution of the ECD relative to the coordinate axes (Fig. 3), so for the fixed SECP the points of the plan are given in the I quadrant, and for the moving one – in the I and II quadrants.

Fig. 4 is presented in order to provide a visual representation of the experiment plan. Fig. 4,*a* shows the location of the points of LPτ–sequences for their small number N = 250 in the 3D space k = 3, and Fig. 4,*b* shows the location of the indicated points in subspaces of smaller dimension k = 2 for the combined factors (ξ_1, ξ_2, ξ_4). Fig. 4,*c*-*f* present a 3D distribution of points for fixed radii 1, 5, 10 and 15 mm when generating them according to this plan.

For realization of the second stage the heuristic method of constructing metamodels with the help of neural networks is used. The construction of the RBF-metamodels is accomplished with the help of an automatic strategy and multiple sub-samples.

In the automatic mode, the samples are formed by random division in the ratio: 70 % – training, 15 % – control, 15 % – test, where the test population was used for cross-checking.

In the second series of constructing metamodels, using the method of multiple sub-samples, a bagging algorithm was used in which 20 repetitive samples were generated based on the training set and training was performed based on these bootstrap-samples of the 20 neural networks. Elements not included in the next sample are used as a test set for the corresponding neural network. For neural networks, the problem of «retraining» is inherent, which is associated with the number of neurons in the hidden layer. During the training of the network the technique of regularization is used, which avoids retraining the neural network. Unsuccessful versions of networks with productivity less than 90 % were filtered off. All other networks were evaluated by subjective analysis of histograms of residues, scattering diagrams and numerical values of indicators: determination coefficient R^2 (performance), the ratio of standard deviations of forecast error and training data *S.D.ratio*, the average relative value of the model error *MAPE*, the residual median square MS_R.

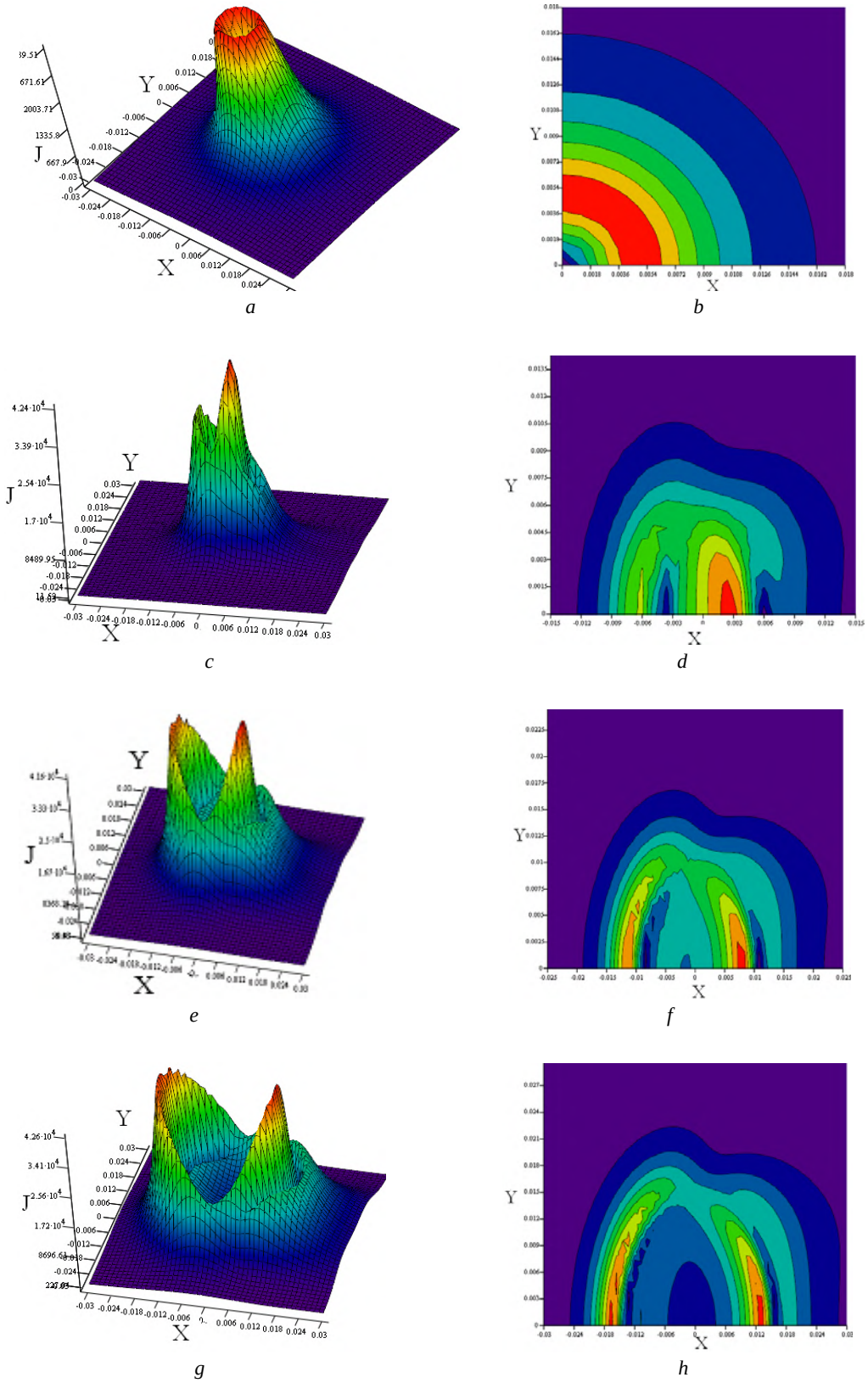

Fig. 3. Exact function of the ECD distribution on the surface of the OC in the control zone 30×30 mm: fixed SECP, excitation coil r = 5 mm (*a*, *b*); movable SECP, excitation coil r = 5 mm (*c*, *d*); movable SECP, excitation coil r = 10 mm (*e*, *f*); movable SECP, excitation coil r = 15 mm (*g*, *h*)

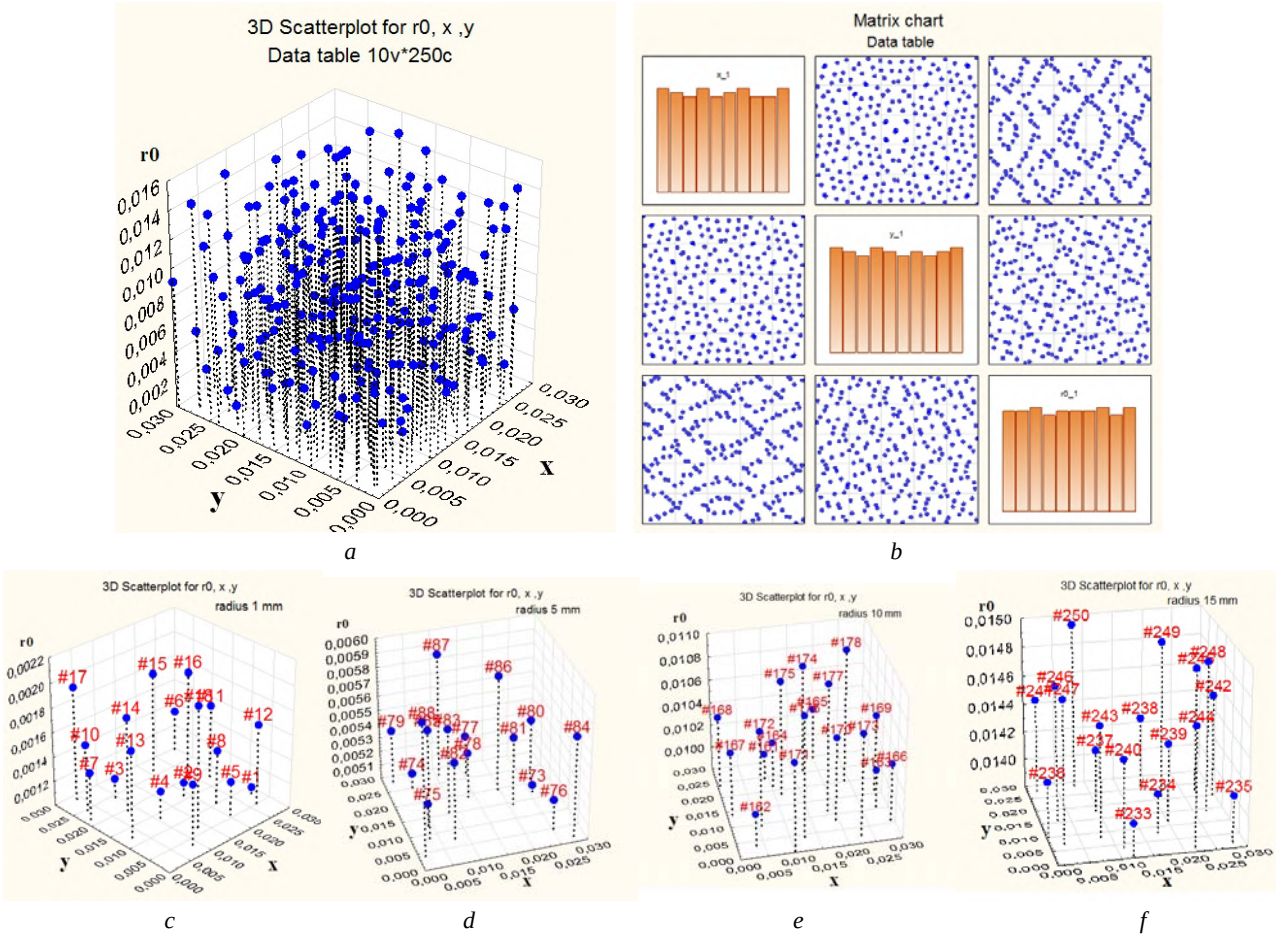

Fig. 4. Locations of the points of LPτ-sequences (ξ_1, ξ_2, ξ_4) in the 3D factor space: for r = 1 ... 15 mm, number of points N = 250 (*a*); matrix representation of sequences (ξ_1, ξ_2, ξ_4) in 2D projections (*b*); for a radius of an excitation coil of 1 mm (*c*); for a radius of 5 mm (*d*); for a radius of 10 mm (*e*); for a radius of 15 mm (*f*)

To construct a metamodel of a fixed SECP with variation of three parameters within x = 0 ... 30 mm; y = 0 ... 30 mm; r = 1 ... 15 mm almost 320 RBF-neuron networks are created for the plan N = 2048 with the number of hidden neurons from 280 to 350, of which the best (Table 1) are selected for the indicated indicators. Networks with a productivity of more than 0.9 were used together, organizing a networks committee.

To improve accuracy, as a rule to make a decision the average value of the networks included in the committee is used. For the neural networks committee, in Fig. 5,*b*,*d*,*f* lines of the level of the surface of the response are presented in the previously determined ranges of variations of variables reproduced at 2048 points of the training sample. Each section of the surface in the radius accounts for about 145 points. Table 2 shows the results of the approximation of the ECD distribution by the created committee for radii 5, 10, 15 mm.

To construct the metamodel of the SECP taking into account of the effect of speed υ = (40; 0; 0) m/s and variation of three parameters within x = –30…30 mm; y = 0…24 mm; r = 2…15 mm, almost 95 RBF-neuron networks were created for the plan N = 3315 with the number of hidden neurons from 200 to 700, of which the best (Table 3, 4) were selected for the indicated indicators.

For the neural networks committee, Fig. 6,*b*,*d*,*f* show lines of the level of the surface of the response, reproduced at 3315 points of the training sample. In each section of the surface in a radius in this plan is 255 points.

Table 1

The best RBF-metamodels for a fixed SECP

No.	Neural network	R^2 for training, control and test samples	S.D.ratio	MAPE, %	MS_R
1	RBF-3-282-1(156)	0.9949; 0.9946; 0.993	0.086	22.6	0.00057
2	RBF-3-293-1(218)	0.993; 0.994; 0.994	0.0904	27.9	0.000614
3	RBF-3-293-1(219)	0.994; 0.992; 0.989	0.0939	28.6	0.000674
4	RBF-3-300-1(254)	0.9949; 0.993; 0.989	0.0891	26.8	0.000631
5	RBF-3-322-1(284)	0.995; 0.992; 0.988	0.09	22.9	0.000613
6	RBF-3-343-1(307)	0.996; 0.993; 0.996	0.0739	22.1	0.000424

Table 2

Results of approximation of the ECD distribution by the networks committee for a fixed SECP

Radius, mm	S.D.ratio	MAPE, %	MS_R
5	0.164	13.08	0.000506
10	0.061	5.89	0.000316
15	0.083	6.43	0.000947

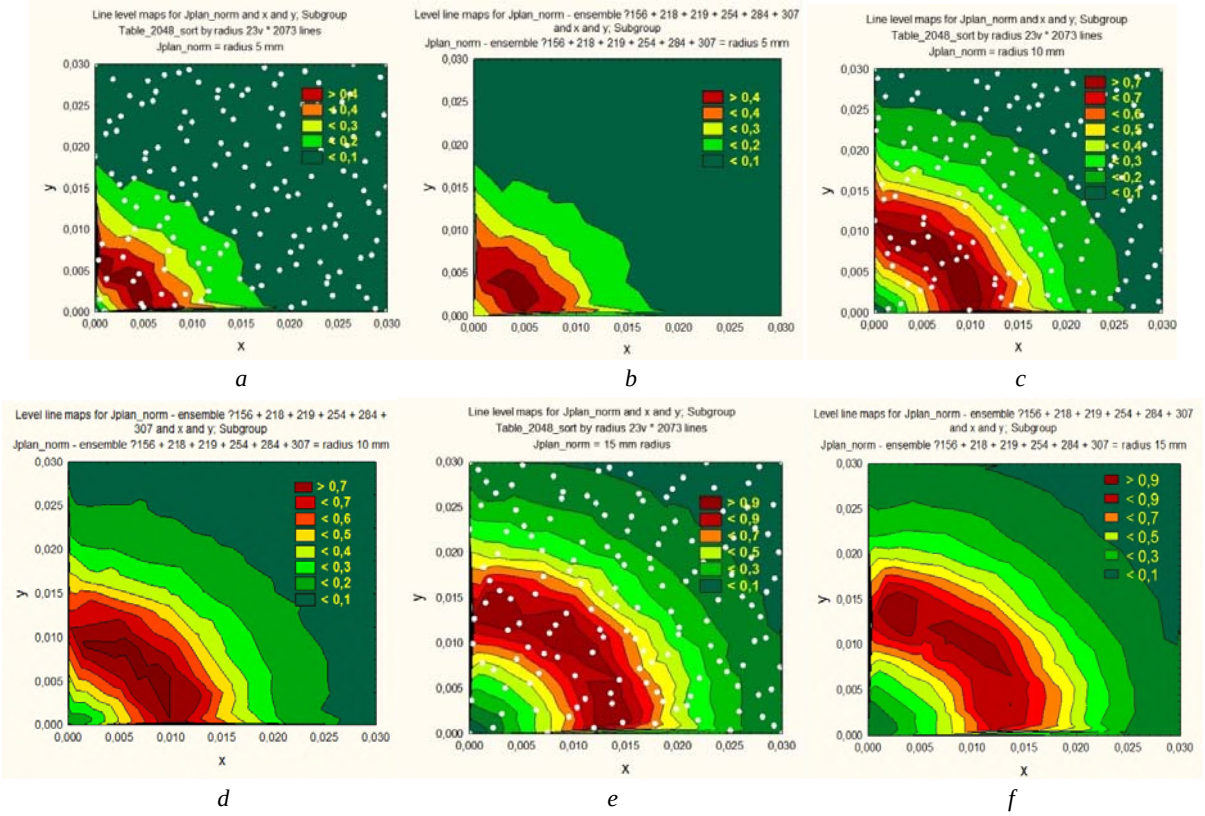

Fig. 5. Lines of the level of the surface of the response of a fixed SECP: the plan of experiment N = 145, applied on the lines of the level of the «exact» model, for the sections of the surface of radii r = 5, 10, 15 mm respectively (*a*, *c*, *e*); the surface of the response, reproduced at the points of the training sample using the networks committee (*b*, *d*, *f*)

Table 3

The best RBF-metamodels for a movable SECP

No.	Neural network	R^2 for training, control and test samples	S.D.ratio	MAPE, %	MS_R
1	RBF-3-610-1(2)	0.944; 0.933; 0.926	0.278	46	0.00458
2	RBF-3-620-1(8)	0.958; 0.942; 0.935	0.263	41.2	0.00355
3	RBF-3-627-1(15)	0.96; 0.941; 0.918	0.272	44.1	0.00367
4	RBF-3-635-1(28)	0.96; 0.947; 0.933	0.265	37.74	0.00345
5	RBF-3-635-1(29)	0.96; 0.949; 0.924	0.261	38.3	0.00349
6	RBF-3-665-1(31)	0.958 0.95; 0.938	0.261	39.2	0.00347
7	RBF-3-665-1(34)	0.96; 0.948; 0.937	0.262	32.9	0.00341

Table 4

Results of approximation of the ECD distribution by the networks committee for a movable SECP

Radius, mm	S.D.ratio	MAPE, %	MS_R
5	0.242	31	0.001151
10	0.293	23	0.002382
15	0.381	21.7	0.008434

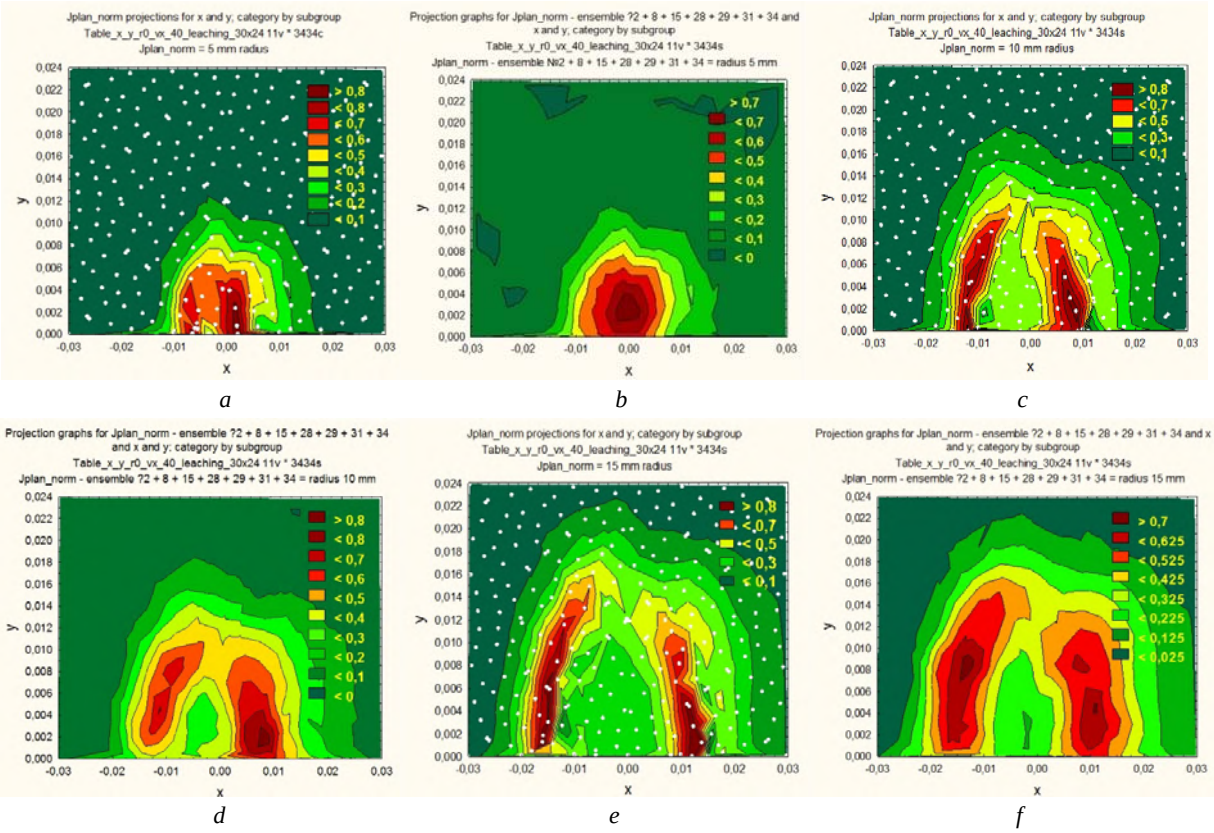

a *b* *c*

d *e* *f*

Fig. 6. Lines of the level of the surface of the response of a movable SECP: the plan of experiment $N = 255$, applied on the lines of the level of the «exact» model, for the sections of the surface of radii $r = 5$, 10, 15 mm respectively (*a, c, e*); the surface of the response, reproduced at the points of the training sample by the networks committee (*b, d, f*)

Validation and verification of SECP metamodels. One of the criteria for the quality of a multivariate regression model is to verify the correctness of the reproducibility of the response surface using the resulting mathematical model throughout the modeling area. Fig. 7 shows the results of the reproduction of the response surface for a fixed SECP obtained with the help of the neural networks committee, executed in the entire range of variation of variables at a considerably increased number of points 7154. In this case, the sections of the surface with radii 5, 10, 15 mm accounted for 511 points.

At the stage of reproduction of the response surface, the adequacy of the obtained metamodel is evaluated according to the indicators: the sum of the squares corresponding to the regression, the remnants, the total; middle squares; dispersion of reproducibility, adequacy, general; standard error of reproducibility estimation, estimation of adequacy, overall; determination factor; ratio of standard deviations; average relative value of model error (or average error of approximation) [22]. The estimation of these indicators is summarized in Table 5.

Fig. 8 shows the result of the reproduction of the response surface received by the neural networks committee for a moving SECP, executed throughout the range of variation of variables at 6643 points. On the sections of the surface of radii 5, 10, 15 mm in this example there are 511 points.

For the created neural networks committee, the indicators characterizing the adequacy and informativeness of the metamodel are estimated, the results of which are summarized in Table 6.

Table 5

Verification of the adequacy and informativeness of the metamodel of a fixed SECP

Dispersion components ($N = 7154$):		Sum of squares	Middle square	Dispersion	Standard estimation error
regression		$SS_D = 369.265$	$MS_D = 123.088$	$\sigma^2_D = 0.051537$	$S_D = 0.227018$
remnants		$SS_R = 1.91$	$MS_R = 0.000266$	$\sigma^2_R = 0.000266$	$S_R = 0.016325$
general		$SS_T = 374.088$	$MS_T = 0.052221$	$\sigma^2_T = 0.052210$	$S_T = 0.228496$
Fisher criterion $F^{\text{experimental}}_{\nu_D;\nu_R} > F^{\text{table value}}_{\alpha;\nu_D;\nu_R}$		$F^{\text{experimental}}_{3;7150} = 193.74$; $F^{\text{table value}}_{0,05;3;7150} = 2.6079$			
determination factor R^2		0.9945			
average error of approximation, MAPE, %	$r = 5$ mm	16.56 %			
	$r = 10$ mm	5.92 %			
	$r = 15$ mm	5.41 %			
ratio of standard deviations S.D.ratio		0.071445			

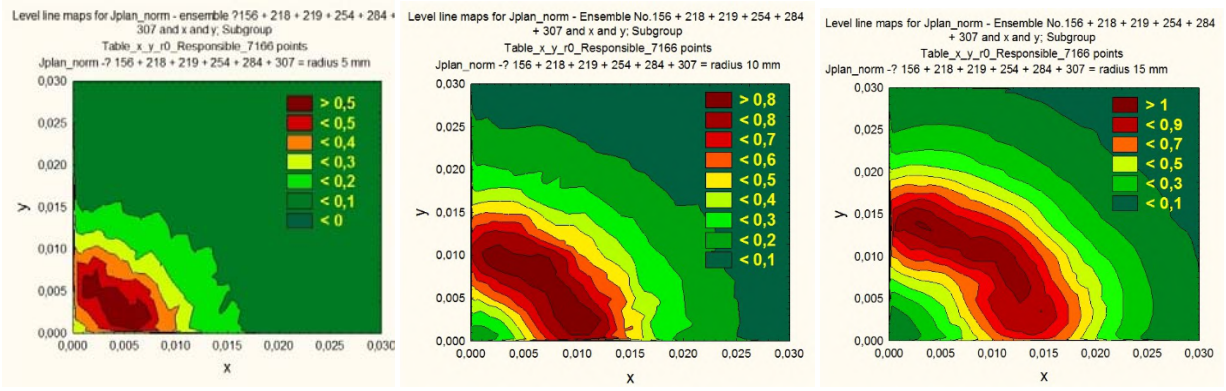

a *b* *c*

Fig. 7. Reproduction of the response surface with the help of the neural networks committee for a fixed SECP. Level lines reproduced at N = 511 points for sections of the surface with radii 5, 10, 15 mm respectively (*a*, *b*, *c*)

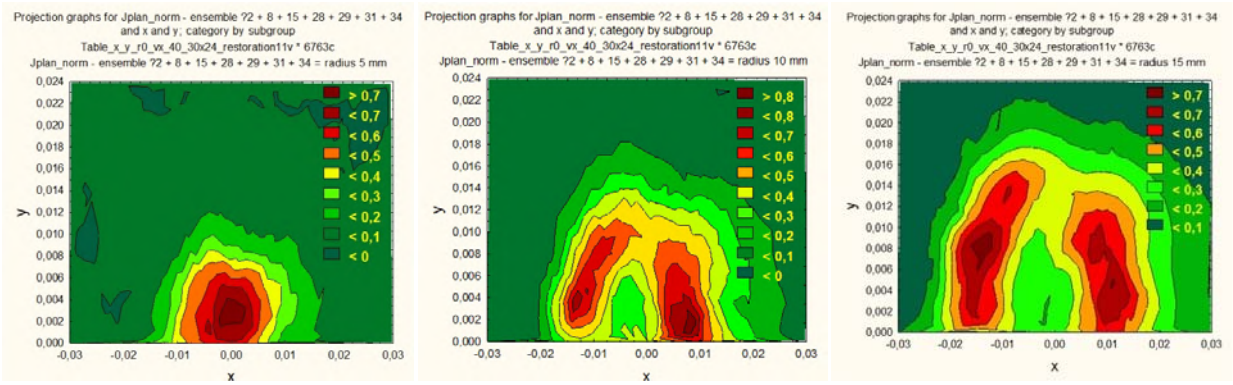

a *b* *c*

Fig. 8. Reproduction of the response surface with the help of the neural networks committee for a movable SECP. Level lines reproduced at N = 511 points for sections of the surface with radii 5, 10, 15 mm respectively (*a*, *b*, *c*)

Table 6

Verification of the adequacy and informativeness of the metamodel of a movable SECP

Dispersion components (N = 6643)		Sum of squares	Middle square	Dispersion	Standard estimation error
regression		SS_D = 244.1923	MS_D = 81.397	σ^2_D = 0.036111	S_D = 0.190030
remnants		SS_R = 27.5733	MS_R = 0.004077	σ^2_R = 0.004077	S_R = 0.06385
general		SS_T = 278.9221	MS_T = 0.041248	σ^2_T = 0.041248	S_T = 0.203097
Fisher criterion $F^{\text{experimental}}_{\nu_D;\nu_R} > F^{\text{table value}}_{\alpha;\nu_D;\nu_R}$		$F^{\text{experimental}}_{3;6639}$ = 8.857; $F^{\text{table value}}_{0,05;3;6639}$ = 2.6079			
determination factor R^2		0.901353			
average error of approximation, MAPE, %	r = 5 mm	40.38 %			
	r = 10 mm	23.54 %			
	r = 15 mm	24.79 %			
ratio of standard deviations S.D.ratio		0.314381			

The results of the study can be used in the synthesis of mobile SECP with a priori set ECD distribution in the control zone.

Conclusions.

1. For the first time, RBF-metamodels of a concentric circular SECP (both fixed one and taking into account the speed effect) are created.

2. Based on modern computer methods of planning the experiment, artificial intelligence and data analysis, the computational technique of constructing metamodels characterized by a lower computational resource intensity during simulation is improved.

3. For the first time, geometric models of excitation structures of circular SECPs with uniformity of sensitivity for their optimal synthesis taking into account the effect of speed are proposed.

4. The task of creating software for calculating the ECD distribution in the control zone of the SECP taking into account the effect of speed by «exact» electrodynamic mathematical models is solved. The task of creating software for forming points of an experiment plan using the Sobol LPτ–sequences is solved, which made it possible to select the most perfect experiment plans individually for the approximated surfaces of the response.

REFERENCES

1. Stelblev Yu.I. Synthesis of the given characteristics of eddy current converters. *Defectoscopy*, 1984, no.11, pp. 12-20. (Rus).

2. Stelblev Yu.I. Synthesis of eddy current transformers with a given structure of the excitatory field in the control zone. *Defectoscopy*, 1986, no.4, pp. 58-64. (Rus).

3. Halchenko V.Ya., Pavlov O.K., Vorobyov M.O. Nonlinear synthesis of magnetic fields of excitation of eddy-current converters of flaw detectors. *Methods and instruments of quality control*, 2002, no.8, pp. 3-5. (Ukr).

4. Gal'chenko V.Ya., Vorob'ev M.A. Structural Synthesis of Attachable Eddy-Current Probes with a Given Distribution of the Probing Field in the Test Zone. *Russian Journal of Nondestructive Testing*, 2005, vol.41, no.1, pp. 29-33. **doi: 10.1007/s11181-005-0124-7.**

5. Su Z., Ye C., Tamburrino A., Udpa L., Udpa S. Optimization of coil design for eddy current testing of multi-layer structures. *International Journal of Applied Electromagnetics and Mechanics*, 2016, vol.52, no.1-2, pp. 315-322. **doi: 10.3233/JAE-162030.**

6. Su Z., Efremov A., Safdarnejad M., Tamburrino A., Udpa L., Udpa S.S. Optimization of coil design for near uniform interrogating field generation. *AIP Conference Proceedings*, 2015, vol.1650, no.1, pp. 405-413. **doi: 10.1063/1.4914636.**

7. Stawicki K., Gratkowski S. Optimization of Exciter Coils in Eddy Current Transducer for Testing Thick Conducting Plates. *International Symposium on Electromagnetic Fields in Electrical Engineering; Electromagnetic fields in mechatronics, electrical and electronic engineering: ISEF'05*; 2005; Baiona, Spain in studies in applied electromagnetics and mechanics; 27; Oxford, Amsterdam, IOS Press, 2006. pp. 497-502.

8. Itaya T., Ishida K., Kubota Y., Tanaka A., Takehira N. Visualization of eddy current distributions for arbitrarily shaped coils parallel to a moving conductor slab. *Progress In Electromagnetics Research M*, 2016, vol.47, pp. 1-12. **doi: 10.2528/PIERM16011204.**

9. Itaya T., Miki T., Takehira N., Tanaka A., Ishida K. Eddy current distribution for a rectangular coil arranged parallel to a moving conductor slab. *IET Science, Measurement & Technology*, 2012, vol.6, no.2, pp. 43-51. **doi: 10.1049/iet-smt.2011.0015.**

10. Ishida K., Itaya T., Tanaka A., Takehira N. Magnetic Field Analysis of an Arbitrary Shaped Coil Using Shape Functions. *IEEE Transactions on Magnetics*, 2009, vol.45, no.1, pp. 104-112. **doi: 10.1109/TMAG.2008.2005119**.

11. Panas S., Kriezis E.E. Eddy current distribution due to a rectangular current frame moving above a conducting slab. *Archiv für Elektrotechnik*, 1986, vol.69, no.3, pp. 185-191. **doi: 10.1007/BF01574623**.

12. Thollon F., Lebrun B., Burais N., Jayet Y. Numerical and experimental study of eddy current probes in NDT of structures with deep flaws. *NDT & E International*, 1995, vol.28, no.2, pp. 97-102. **doi: 10.1016/0963-8695(94)00010-h.**

13. Theodoulidis T., Bowler J.R. Interaction of an Eddy-Current Coil With a Right-Angled Conductive Wedge. *IEEE Transactions on Magnetics*, 2010, vol.46, no.4, pp. 1034-1042. **doi: 10.1109/TMAG.2009.2036724.**

14. Trembovetska R.V., Halchenko V.Ya., Tychkov V.V. The MLP-Metamodels Application In The Surrogate Optimization Tasks. *Young Scientist*, 2018, vol.6, no.2, pp. 32-39. (Ukr).

15. Halchenko V.Ya., Trembovetska R.V., Tychkov V.V. Neural network metamodel of a cylindrical overhead eddy current converter as a component of surrogate optimal synthesis. *Bulletin of Kherson National Technical University*, 2018, no.3(66), vol.1, pp. 32-38. (Ukr).

16. Galchenko V.Ya., Trembovetska R.V., Tychkov V.V. Application of metamodels for solving problems of synthesis of eddy current converters with a homogeneous distribution of current density in the control zone. *Zbirnik tez dopovidej XVII Mizhnarodnoï naukovo-tehnichnoï konferenciï «Priladobuduvannja: stan i perspektivi»* [Materials of the XVII Int. Sci.-Pract. Conf. «Instrumentation: state and prospects»]. Kyiv, NTUU «KPI», 15-16 May, 2018, pp. 146-147. (Ukr).

17. Halchenko V.Y., Trembovetska R.V., Tychkov V.V. The neurocomputing using of the development metamodels stage in the optimal surrogate antennas synthesis process. *Visnyk NTUU KPI Seriia – Radiotekhnika Radioaparatobuduvannia*, 2018, no.74, pp. 60-72. **doi: 10.20535/radap.2018.74.60-72.**

18. Kuznetsov B.I., Nikitina T.B., Tatarchenko M.O., Khomenko V.V. Multicriterion anisotropic regulators synthesis by multimass electromechanical systems. *Tekhnichna Elektrodynamika*, 2014, no.4, pp. 105-107. (Rus).

19. Kuznetsov B.I., Nikitina T.B., Voloshko A.V., Bovdyj I.V., Vinichenko E.V., Kobilyanskiy B.B. Single-circuit active screening of magnetic field generated by several overhead transmission lines in residential area. *Electrical engineering & electromechanics*, 2018, no.1, pp. 41-45. **doi: 10.20998/2074-272X.2018.1.06**.

20. Haykin Simon. *Neironnye seti: polnyi kurs* [Neural Networks: A Complete Course]. Moscow, Williams Publ. House, 2006. 1104 p. (Rus).

21. Sobol I.M., Statnikov R.B. *Vybor optimal'nyh parametrov v zadachah so mnogimi kriterijami* [Choosing Optimal Parameters in Problems with Many Criteria]. Moscow, Drofa Publ., 2006. 175 p. (Rus).

22. Radchenko S.G. *Metodologija regressionnogo analiza: monografija* [Methodology of regression analysis: monograph]. Kyiv, Korniychuk Publ., 2011. 376 p. (Rus).

Received 08.10.2018

V.Ya. Halchenko[1], *Doctor of Technical Science, Professor,*
R.V. Trembovetska[1], *Candidate of Technical Science, Associate Professor,*
V.V. Tychkov[1], *Candidate of Technical Science, Associate Professor,*
[1] Cherkasy State Technological University,
460, Shevchenko Blvd., Cherkasy, 18006, Ukraine,
e-mail: halchvl@gmail.com

How to cite this article:
Halchenko V.Ya., Trembovetska R.V., Tychkov V.V. Development of excitation structure RBF-metamodels of moving concentric eddy current probe. *Electrical engineering & electromechanics*, 2019, no.2, pp. 28-38. **doi: 10.20998/2074-272X.2019.2.05.**

UDC 621.3.022: 621.315.3: 537.311.8 **doi: 10.20998/2074-272X.2019.2.06**

M.I. Baranov

CALCULATION AND EXPERIMENTAL DETERMINATION OF CRITICAL SECTIONS OF ELECTRIC WIRES AND CABLES IN THE CIRCUITS OF DEVICES OF HIGH-VOLTAGE HIGH-CURRENT PULSE TECHNIQUE

Purpose. *Implementation of calculation and experimental determinations of critical sections and current densities in electric wires and cables of circuits of devices of high-voltage high-current impulse technique (HHIT), characterized flowing of pulse current $i_p(t)$ with different amplitude-temporal parameters (ATPs).* ***Methodology.*** *Electrophysics bases of technique of high-voltage and large pulse currents, theoretical bases of electrical engineering, bases of electrical power energy, technique of high electric and magnetic fields, and also measuring technique.* ***Results.*** *The results of the developed electrical engineering approach are resulted in calculation choice on the condition of electric explosion (EE) in atmospheric air of current-carrying parts of cable-conductor products of critical sections of S_{CCi} of the uninsulated wires, and also the insulated wires and cables with polyvinyl chloride (PVC), rubber (R) and polyethylene (PET) insulation with copper (aluminum) cores (shells) on which in the circuits of HHIT the pulse axial-flow current $i_p(t)$ flows with arbitrary ATPs. On the basis of this approach the results of choice of critical sections S_{CCi} are shown for the indicated electric wires (cables) of power circuits of HHIT with pulse current, ATPs of which with amplitudes of I_{mp}=(0.1-1000) kA change on a aperiodic law or law of attenuation of sine wave in nano-, micro- and millisecond temporal ranges. The results of calculation estimation of critical amplitudes of current densities δ_{CCi} of -pulses of current $i_p(t)$ of the examined temporal shapes are presented in the indicated electric wires and cables of circuits of HHIT. By a calculation way it is set that critical amplitudes of current densities δ_{CCi} of pulse current $i_p(t)$ for its indicated temporal shapes in the copper (aluminum) cores of the uninsulated wires and insulated wires and cables with copper (aluminum) cores (shells), PVC, R and PET insulation for nanosecond range are numerically 1176 (878) kA/mm^2, for the microsecond range 64 (48) kA/mm^2 and for the millisecond range 1.29 (0.97) kA/mm^2. By the powerful high-voltage generator of current of artificial lightning experimental verification of applicability of the offered calculation relations is executed for the choice of critical sections S_{CCi} and amplitudes of current densities δ_{CCi} in wires (cables) at their EE.* ***Originality.*** *First by a calculation way for the specific temporal shapes of pulse currents $i_p(t)$ in the discharge circuits of HHIT, changing in nano-, micro- and millisecond temporal ranges with the wide change of the amplitudes I_{mp} on an aperiodic law or law of attenuation of sine wave, the numeral values of critical sections S_{CCi} and amplitudes of current densities δ_{CCi} are obtained for the uninsulated wires, insulated wires and cables with copper (aluminum) cores (shells), PVC, R and PET insulation.* ***Practical value.*** *Application of the obtained results is in practice of tests of objects of electrical power energy, aviation and space-rocket technique on resistibility to action of pulse currents $i_p(t)$ with different ATPs of natural (currents of the imitated lightning) and artificial (discharge currents of HHIT) origin will be instrumental in the increase of electro-thermal resistibility of the uninsulated wires, and also the insulated wires and cables with PVC, R and PET insulation of HHIT widely applied in power circuits.* References 15, tables 7, figures 6.

Key words: **high-voltage high-current pulse technique, electric wires and cables, calculation choice of critical sections of wires and cables in circuits of pulse technique, experiment.**

Надані результати *розробленого електротехнічного підходу до розрахункового вибору за умовою електричного вибуху (ЕВ) струмопровідних частин кабельно-провідникової продукції критичних перерізів S_{CCi} неізольованих дротів, а також ізольованих дротів і кабелів з полівінілхлоридною (ПВХ), гумовою (Г) і поліетиленовою (ПЕТ) ізоляцією з мідними (алюмінієвими) жилами (оболонками), по яких в колах високовольтної сильнострумної імпульсної техніки (ВСІТ) протікає імпульсний аксіальний струм $i_p(t)$ з довільними амплітудно-часовими параметрами (АЧП).* ***На підставі*** *цього підходу продемонстровані результати вибору критичних перерізів S_{CCi} для вказаних електричних дротів (кабелів) силових кіл ВСІТ з імпульсним струмом, АЧП якого з амплітудами I_{mp}=(0,1-1000) кА змінюються по аперіодичному закону або закону затухаючої синусоїди в нано-, мікро- і мілісекундному часових діапазонах.* ***Представлені*** *результати розрахункової оцінки критичних амплітуд щільностей δ_{CCi} імпульсів струму $i_p(t)$ цих часових форм у вказаних електричних дротах і кабелях кіл ВСІТ.* ***Виконана*** *експериментальна перевірка працездатності запропонованих розрахункових співвідношень для вибору перерізів S_{CCi} і щільностей δ_{CCi} струму в дротах (кабелях) при їх ЕВ.* ***Отримані*** *результати сприятимуть забезпеченню електротермічної стійкості електричних неізольованих дротів, а також ізольованих дротів і кабелів зі ПВХ, Г і ПЕТ ізоляцією, які широко застосовуються у силових колах ВСІТ.* Бібл. 15, табл. 7, рис. 6.

Ключові слова: **високовольтна сильнострумна імпульсна техніка, електричні дроти і кабелі, розрахунковий вибір критичних перерізів дротів і кабелів в колах імпульсної техніки, експеримент.**

Приведены результаты *разработанного электротехнического подхода к расчетному выбору по условию электрического взрыва (ЭВ) токонесущих частей кабельно-проводниковой продукции критических сечений S_{CCi} неизолированных проводов, а также изолированных проводов и кабелей с поливинилхлоридной (ПВХ), резиновой (Р) и полиэтиленовой (ПЭТ) изоляцией с медными (алюминиевыми) жилами (оболочками), по которым в цепях высоковольтной сильноточной импульсной техники (ВСИТ) протекает импульсный аксиальный ток $i_p(t)$ с произвольными амплитудно-временными параметрами (АВП).* ***На основании*** *этого подхода продемонстрированы результаты выбора критических сечений S_{CCi} для указанных электрических проводов (кабелей) силовых цепей ВСИТ с импульсным током, АВП которого с амплитудами I_{mp}=(0,1-1000) кА изменяются по апериодическому закону или закону затухающей синусоиды в нано-, микро- и миллисекундному временных диапазонах.* ***Представлены*** *результаты расчетной оценки критических амплитуд плотностей δ_{CCi} импульсов тока $i_p(t)$ рассматриваемых временных форм в указанных электрических проводах и кабелях цепей ВСИТ.* ***Выполнена*** *экспериментальная проверка работоспособности предлагаемых расчетных соотношений для выбора сечений S_{CCi} и плотностей δ_{CCi} тока в*

проводах (кабелях) при их ЭВ. Полученные данные будут способствовать обеспечению электротермической стойкости электрических неизолированных проводов, а также проводов и кабелей с ПВХ, Р и ПЭТ изоляцией, широко применяемых в силовых цепях ВСИТ. Библ. 15, табл. 7, рис. 6.
Ключевые слова: **высоковольтная сильноточная импульсная техника, электрические провода и кабели, расчетный выбор критических сечений проводов и кабелей в цепях импульсной техники, эксперимент.**

Introduction. In practice, when designing, building and operating high-power electrical installations in the field of high-voltage high-current impulse technology (HHIT), specialists need to be able to determine the critical cross sections S_{CCi} of electrical wires and cables used in their circuits and containing metal wires (i=1) and shells (i=2). The critical sections S_{CCi} of wires (cables) are their cross sections that are not able to withstand the current loads acting on them with one or another amplitude-temporal parameters (ATPs), leading to the appearance of the electric explosion (EE) phenomenon of metal cores (shells) of specified wires and cables and, accordingly, to their failure [1, 2]. Note that the EE phenomenon of current-carrying parts can also be observed in the field of industrial electric power engineering, when wires and cables not reasonably used in power grids are not designed for the flow of high short-circuit (SC) currents through them, reaching at durations of (60-100) ms amplitude values up to (10-100) kA [3]. One of the peculiarities of electrical installations of HHIT, in contrast to electrical installations of industrial electric power engineering, is that pulse currents of various ATPs related to the nano-, micro- and millisecond time ranges can flow through the current-carrying parts of their electrical circuits. In this case, the amplitude values I_{mp} of such pulse currents can reach values that usually vary in the range (0.1–1000) kA [1, 2].

In [4], the author presented a generalized electrical engineering approach that allows for the condition of thermal durability of cable-conductor products (CCP) to carry out an approximate computational choice of the maximum allowable cross sections S_{Cli} of uninsulated wires, insulated wires and cables with copper (aluminum) conductors (shells) with polyvinyl chloride (PVC), rubber (R) and polyethylene (PET) insulation, the current-carrying parts of which are influenced in the adiabatic mode by the direct effect of the axial pulse current $i_p(t)$, the ATPs of which with amplitudes of 0.1 kA$\le I_{mp}\le$1000 kA can vary in nano-, micro- and millisecond time ranges. In this regard, the issues of determining the numerical values of the critical cross sections S_{CCi} of electrical wires and cables in relation to the power circuits of HHIT remain relevant in the world and are subject to their decision.

The goal of the paper is to perform the calculation and experimental determination of critical cross sections S_{CCi} and current densities δ_{CCi} in wires and cables of HHIT circuits characterized by the flow of pulse axial currents $i_p(t)$ along the current-carrying parts of their CCP with different ATPs.

1. Problem definition. Consider the widely used uninsulated copper and aluminum wires in HHIT power circuits, as well as insulated wires and cables with copper (aluminum) inner conductors and outer shells (reverse conductors) with specific electrical conductivity γ_{0i} of their nonmagnetic material, which usually have PVC, R and PET insulation [1-3]. It is assumed that in the round solid or split copper (aluminum) conductors (shells) of the above wires and cables of the HHIT electrical circuits pulse currents $i_p(t)$ flow in their longitudinal direction, the ATPs of which correspond to nano-, micro- or millisecond time ranges with amplitudes I_{mp} varying in the range from 100 A to 1000 kA. We assume that the wires and cables under consideration are placed in the surrounding air environment, the temperature of which corresponds to room temperature and equal to θ_0 = 20 °C [2]. We suppose that the preliminary current load of the current-carrying parts of the CCP of power circuits of HHIT is absent. Therefore, the initial temperature θ_{Ci} (before the affect of the pulse current $i_p(t)$ on the CCP) of the core (shell) material of the wire (cable) will be equal to the ambient air temperature θ_0. We use the assumption that the pulse axial current $i_p(t)$ is almost uniformly distributed over the cross section S_{Ci} of the core and shell (screen) of the wire (cable). At the same time, we remember that the penetration depth $\Delta_i\approx[6t_m/(\pi\mu_0\gamma_{0i})]^{1/2}$ in the quasi-stationary mode, where $\mu_0=4\pi\cdot10^{-7}$ H/m is the magnetic constant [2], of the azimuthal magnetic field pulse with time t_m corresponding to its amplitude, for example, for an aperiodic microsecond current pulse of artificial lightning of the temporal shape τ_f/τ_p=10 μs/350 μs ($t_m\approx1.6\tau_f\approx$16 μs) [5], where τ_f, τ_p are the front duration and the duration of the current pulse at the level of its half-decay, in the studied non-ferromagnetic materials of the core (shell) of the wire (cable) is for copper approximately 0.65 mm, but for aluminum is 0.82 mm [4]. These numerical values Δ_i are often commensurate with the actual radii of the cores and the thicknesses of the shells of the wires (cables) under consideration, in which the EE phenomenon of the current-carrying parts of the CCP may be observed. For millisecond axial current pulses $i_p(t)$, the accepted assumption about the uniform nature of its radial distribution in the studied conductors (shells) of wires and cables becomes even more legitimate. Thus, for example, for an aperiodic millisecond pulse of a long-term *C*- component of artificial lightning current of the temporal shape τ_f/τ_p= = 7 ms/160 ms ($t_m\approx$11 ms), the considered penetration depth Δ_i for copper is about 17 mm, and for aluminum is 22 mm. We use the condition of adiabatic nature of the electrothermal processes taking place at durations of pulsed current $i_p(t)$ of no more than 1000 ms in the materials of the cores (shells) of the CCP under study, at which the influence of heat transfer from the surfaces of their current-carrying parts having the current temperature $\theta_{Ci}\ge\theta_0$ as well as the thermal conductivity of layers of their conductive materials of the core (shell) and insulation on Joule heating of the current-carrying parts of the CCP are neglected.

It is required by calculation in an approximate form to determine the critical sections S_{CCi} of current-carrying parts for uninsulated copper (aluminum) wires, as well as for insulated wires and cables with copper (aluminum)

cores (shells), PVC, R and PET insulation, used in HHIT circuits and influenced by direct effect of axial pulse current $i_p(t)$ of various amplitudes I_{mp}, varying in nano-, micro- and millisecond time ranges. In addition, it is necessary to experimentally verify the operability of the obtained relations for the approximate calculation of the critical sections S_{CCi} of wires (cables) and critical densities δ_{CCi} of the pulse current $i_p(t)$ in them on the operating electrical installations of HHIT.

2. Electrical engineering approach to the calculation selection of the critical sections S_{CCi} and current densities δ_{CCi} in electrical wires and cables of HHIT circuits. For critical cross sections S_{CCi} of conductive cores (shells) of the considered non- and insulated with PVC, R and PET insulation electrical wires and cables in HHIT circuits with pulse axial current $i_p(t)$ of arbitrary ATPs from the equation of their heat balance at the adiabatic Joule heating of current-carrying parts of the CCP the following calculated relation follows [1]:

$$S_{CCi} = (J_{CiA})^{1/2} / D_{Cik}, \quad (1)$$

where $J_{CiA} = \int_0^{\tau_p} i_p^2(t)dt$ – the integral of the action of the pulse current $i_p(t)$ with the duration of its flow τ_p in the CCP and given ATPs, $A^2 \cdot s$; $D_{Cik} = (J_{Cik})^{1/2}$, $A \cdot s^{1/2}/m^2$; J_{Cik} is the critical value of the current integral for the material of the current-carrying cores (shells) of the studied electric wires and cables of the HHIT circuits, $A^2 \cdot s/m^4$.

In Table 1 at θ_0=20 °C known numerical values are given for such basic characteristics of copper and aluminum cores (shells) of the studied wires (cables) of the HHIT power circuits as γ_{0i} and J_{Cik}.

Table 1

Thermophysical characteristics of the material of the considered cores (shells) of electrical wires and cables of power circuits of HHIT before exposure to them of pulse axial current $i_p(t)$ (at θ_0=20 °C) [2]

Material of the core (shell) of the wire (cable)	Numerical value of the characteristic	
	γ_{0i}, 10^7 $(\Omega \cdot m)^{-1}$	J_{Cik}, 10^{17} $A^2 \cdot s \cdot m^{-4}$
Copper	5.81	1.95
Aluminum	3.61	1.09

As for the calculation determination in (1) of the integral of action J_{CiA} of the pulse axial current $i_p(t)$ with arbitrary ATPs, for the case of its change over time t according to the aperiodic law of the form [1]

$$i_p(t) = k_{p1} I_{mp} \left[\exp(-\alpha_1 t) - \exp(-\alpha_2 t)\right], \quad (2)$$

where $\alpha_1 \approx 0.76/\tau_p$, $\alpha_2 \approx 2.37/\tau_f$ are the shape coefficients of the aperiodic current pulse with given ATPs, flowing in the HHIT; $k_{p1}=[(\alpha_1/\alpha_2)^m - (\alpha_1/\alpha_2)^n]^{-1}$ is the normalization factor; $m=\alpha_1/(\alpha_2-\alpha_1)$; $n=\alpha_2/(\alpha_2-\alpha_1)$, the calculation expression for the integral of action J_{CiA} of the current pulse $i_p(t)$ flowing in the HHIT power circuit takes the following approximate analytical form [4, 6]:

$$J_{CiA} \approx k_{p1}^2 I_{mp}^2 \left[0.658\tau_p - 0.633\tau_f\right]. \quad (3)$$

In case of a change in time t of the current pulse $i_p(t)$, acting on the materials of the wire (cable) of the HHIT, according to the law of a damped sinusoid of the form [1]

$$i_p(t) = k_{p2} I_{mp1} \exp(-\delta t) \sin(\omega t), \quad (4)$$

where $\delta=\Delta_p/T_p$ is the current attenuation coefficient; $\omega=2\pi/T_p$ is the current frequency; T_p is the current oscillation period; $\Delta_p=\ln(I_{mp1}/I_{mp3})$ is the logarithmic decrement of pulse current oscillations with the first I_{mp1} and the third I_{mp3} amplitudes in the HHIT circuit; $k_{p2}=[\exp(-\Delta_p/2\pi \cdot \text{arcctg}\Delta_p/2\pi)\sin(\text{arcctg}\Delta_p/2\pi)]^{-1}$ is the normalizing coefficient for the damped sinusoidal current, then the approximate calculation expression for the integral of action J_{CiA} of the pulse axial current $i_p(t)$ flowing in the HHIT power circuit takes the following simplified analytical form [4]:

$$J_{CiA} \approx k_{p2}^2 I_{mp1}^2 [T_p (4\Delta_p)^{-1} - \Delta_p T_p (4\Delta_p^2 + 16\pi^2)^{-1}]. \quad (5)$$

Knowing from normative documents or experimental data the numerical values of the quantities I_{mp}, τ_f, τ_p, Δ_p, T_p and taking into account the estimates of the values of the normalizing coefficients k_{p1} and k_{p2} by (2)-(4) for the two temporal shapes, the changes in the pulse current $i_p(t)$, we can in an approximate form (with an error of no more than 10%) calculate the critical cross sections S_{CCi} of current-carrying cores (shells) of wires and cables used in electrical power circuits of HHIT. Having found the numerical values of the cross sections S_{CCi}, taking into account the accepted assumptions, the critical amplitudes of the densities δ_{CCi} of the pulse current $i_p(t)$ of a given temporal shape in electrical wires and cables of HHIT circuits can be determined as a first approximation from the relation $\delta_{CCi} \approx I_{mp1}/S_{CCi}$.

3. Calculation determination of critical cross-sections S_{CCi} and current densities δ_{CCi} in electrical wires (cables) for nanosecond current pulses in HHIT circuits. Let us consider the case when an aperiodic current pulse of temporal shape τ_f/τ_p=5 ns/200 ns flows through copper (aluminum) cores (shells) of the HHIT, which was used at the time to simulate an electromagnetic pulse (EMP) of a high-altitude nuclear explosion and test of various objects of military and civilian use for resistibility to the damaging effects of the indicated EMP [4, 7, 8]. From (2), we find that for this calculation case, the shape coefficients α_1 and α_2 of the used current pulse $i_p(t)$ take the following numerical values: $\alpha_1 \approx 3.8 \cdot 10^6$ s^{-1}; $\alpha_2 \approx 4.7 \cdot 10^8$ s^{-1}. In this case, the normalizing coefficient k_{p1} is approximately equal to $k_{p1} \approx 1.049$. In Table 2, taking into account (3) for a specific set of values of the current amplitude I_{mp}, the numerical values of the integral of action J_{CiA} are given for the aperiodic nanosecond current pulse of the temporal shape τ_f/τ_p=5 ns/200 ns flowing through the current-carrying copper and aluminum parts of the studied wires and cables [4, 9].

Knowing the numerical values of the integral of action of the current J_{CiA} (see Table 2) and the integral of current J_{Cik} (see Table 1), the critical sections S_{CCi} of the considered electrical wires (cables) can be determined relatively easily from (1). Table 3 shows the calculated by (1) numerical values of the critical sections S_{CCi} for uninsulated wires with copper (aluminum) cores and insulated wires (cables) with copper (aluminum) cores (shells), PVC, R and PET insulation, experiencing the effect of aperiodic nanosecond current pulse of the temporal shape τ_f/τ_p=5 ns/200 ns.

Table 2

Numerical values of the integral of action J_{CiA} for a nanosecond aperiodic current pulse of the temporal shape 5 ns/200 ns, flowing in the current-carrying parts of the considered CCP [4]

Amplitude value I_{mp}= I_{mp1} of the current pulse of the temporal shape 5 ns/200 ns, kA	Value of the integral of action J_{CiA} of the current pulse 5 ns/200 ns, $A^2 \cdot s$
1	0.141
10	14.13
30	$1.27 \cdot 10^2$
50	$3.53 \cdot 10^2$
70	$6.92 \cdot 10^2$
100	$1.41 \cdot 10^3$
200	$5.65 \cdot 10^3$
500	$3.53 \cdot 10^4$
1000	$1.41 \cdot 10^5$

Table 3

Numerical values of the critical sections S_{CCi} for wires (cables) with copper (aluminum) cores (shells) in the HHIT power circuits with a nanosecond current pulse of 5 ns/200 ns, whose amplitude varies from 10 kA to 500 kA

Type of insulation in the wire (cable) of the HHIT power circuit	Material of the core (shell) of the wire (cable)	Value of the section S_{CCi}, mm^2			
		Amplitude I_{mp} of the pulse current 5 ns/200 ns, kA			
		10	50	100	500
Without insulation, PVC, R and PET insulation	Copper	0.008	0.042	0.085	0.425
	Aluminum	0.011	0.057	0.114	0.569

From the data of Table 3 it follows that the estimated critical amplitudes of the densities $\delta_{CCi} \approx I_{mp}/S_{CCi}$ of a nanosecond current pulse of temporal shape 5 ns/200 ns for both uninsulated wires and wires and cables with copper (aluminum) cores (shells) and PVC, R and PET insulation are, respectively, approximately 1176 kA/mm^2 and 878 kA/mm^2.

4. Calculation determination of critical cross-sections S_{CCi} and current densities δ_{CCi} in electrical wires (cables) for microsecond current pulses in HHIT circuits. Figure 1 shows a typical oscillogram of a pulsed *A*- component of an artificial lightning current formed in a high-current discharge circuit of a high-voltage lightning current generator (LCG) for testing objects of aeronautical and rocket technology on lightning resistibility in accordance with US regulations [10, 11]. It can be seen that this component of current pulses $i_p(t)$ of a lightning simulated under laboratory conditions in time t varies according to the law of damped sinusoid. Let us make the choice of critical sections S_{CCi} and densities δ_{CCi} of current in current-carrying cores (shells) of wires and cables for the discharge circuit of the LCG in relation to current pulse $i_p(t)$ of lightning shown in Fig. 1.

From the experimental data presented in Fig. 1, we obtain that for the used in approximate calculations of critical cross sections S_{CCi} a large exponentially decaying sinusoidal pulse current, the decrement of its oscillations is equal to $\Delta_p=\ln(I_{mp1}/I_{mp3})=2.505$. From (4) for this type of current pulse, we find that the coefficient $k_{p2}=1.731$. Table 4 shows the numerical values of the integral of action J_{CiA} calculated by (5) for a microsecond current pulse varying in time t according to the law of a damped sinusoid of the form (4) [12].

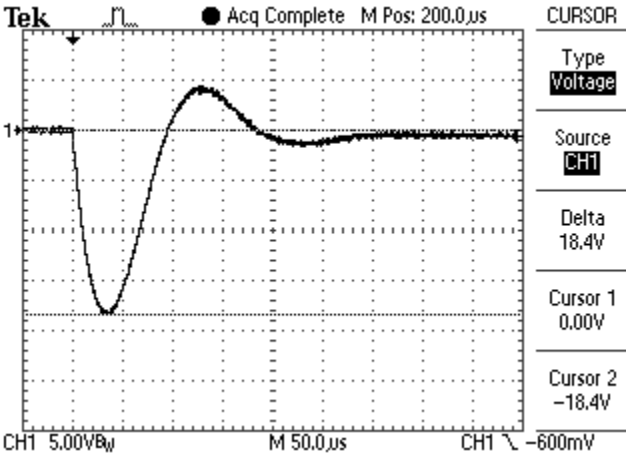

Fig. 1. Typical oscillogram of a microsecond pulsed *A*- component of an artificial lightning current flowing in a high-voltage discharge circuit of a high-voltage LCG ($I_{mp1}\approx-207$ kA; $I_{mp3}\approx-16.9$ kA; $T_p\approx185$ µs; vertical scale - 56.3 kA/division; horizontal scale - 50 µs/division) [12]

Using (1) and summarized in Table 4 the results of the calculation of the integral of action J_{CiA} of the pulse current $i_p(t)$ of the form (4), we find the critical sections S_{CCi} for the wires (cables) under study in the HHIT power circuits, in which the microsecond current pulse of the form (4) with the ATPs corresponding to the experimental data characteristic of Fig. 1 flows. Table 5 presents the results of such a computational determination of the critical sections S_{CCi} for the wires and cables under consideration, which are widely used in HHIT discharge power circuits [1, 2, 12].

Table 4

Values of the integral of action J_{CiA} for current pulse $i_p(t)$, changing in the microsecond time range according to the law of damped sinusoid of the form (4)

Value of the first amplitude I_{mp1} of a damped sinusoidal current pulse, kA	Value of the integral of action J_{CiA} of the current pulse of the form (4), $A^2 \cdot s$
10	$4.77 \cdot 10^3$
30	$4.29 \cdot 10^4$
50	$1.19 \cdot 10^5$
70	$2.34 \cdot 10^5$
100	$4.77 \cdot 10^5$
207	$2.05 \cdot 10^6$
300	$4.29 \cdot 10^6$
500	$11.92 \cdot 10^6$
700	$23.4 \cdot 10^6$
1000	$47{,}7 \cdot 10^6$

From the presented in Table 5 calculated data, it follows that the estimated critical amplitudes of the densities $\delta_{CCi} \approx I_{mp1}/S_{CCi}$ of the microsecond current pulse $i_p(t)$ with ATPs corresponding to the experimental data of Fig. 1, both for uninsulated wires and wires (cables) with copper and aluminum cores (shells), PVC, R and PET insulation are numerically, respectively, about 64 kA/mm^2 and 48 kA/mm^2.

Table 5

Numerical values of critical sections S_{CCi} for wires (cables) with copper (aluminum) cores (shells) in HHIT circuits with a microsecond current pulse of the form (4), the first amplitude of which I_{mp1} varies from 30 kA to 207 kA

Type of insulation in the wire (cable) of the HHIT power circuit	Material of the core (shell) of the wire (cable)	Value of the section S_{CCi}, mm^2			
		The first amplitude I_{mp1} of the current pulse of the form (4), kA			
		30	50	100	207
Without insulation, PVC, R and PET insulation	Copper	0.469	0.781	1.564	3.243
	Aluminum	0.627	1.045	2.092	4.337

5. Calculation determination of critical cross-sections S_{CCi} and current densities δ_{CCi} in electrical wires (cables) for millisecond current pulses in HHIT circuits. Figure 2 shows a typical oscillogram of a long-term *C*- component of the artificial lightning current generated under laboratory conditions according to the requirements of [10] in the LCG discharge circuit for the purpose of experimentally determining the lightning resistibility of aerospace objects under direct lightning conditions. From the data in Fig. 2 it can be seen that the aperiodic current pulse $i_p(t)$ of the artificial lightning of negative polarity of this component of the total current of a thunderstorm discharge varies in the millisecond time range. Its amplitude I_{mp} at t_m≈11 ms is approximately 835 A. At the same time, the duration of the front of the test current pulse is about τ_f≈7 ms, and its duration at the level of $0.5I_{mp}$ is τ_p≈160 ms. In addition, from the data in Fig. 2 it follows that the total duration of the flow of the used component of the current pulse $i_p(t)$ of artificial lightning in the discharge circuit of a high-voltage LCG reaches a value of about 1000 ms. On the basis of the proposed electrical engineering approach, we perform the determination of the critical sections S_{CCi} of wires (cables) for the LCG discharge circuit involved in the formation of the specified current pulse $i_p(t)$.

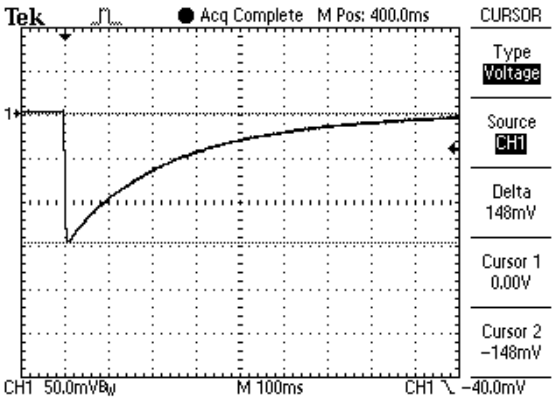

Fig. 2. Typical oscillogram of a millisecond long-term *C*- component of the current of artificial lightning flowing in the discharge circuit of a high-power high-voltage LCG (I_{mp}≈−835 A; τ_f≈7 ms; τ_p≈160 ms; vertical scale − 282 A/division; horizontal scale − 100 ms/division) [12]

From (2) at τ_f≈7 ms and τ_p≈160 ms, we find that α_1≈4.75 s^{-1} and α_2≈3.38·10^2 s^{-1}. Then the normalization coefficient k_{p1} takes a numerical value equal to about k_{p1}≈1.077. Using (3) and varying the amplitude value I_{mp}, one can calculate the numerical values of the integral of action J_{CiA} for the millisecond current pulse $i_p(t)$ used. Table 6 shows the numerical values of J_{CiA} for a series of amplitudes I_{mp} of the current pulse $i_p(t)$ of temporal shape 7 ms/160 ms.

Table 6

Numerical values of the integral of action J_{CiA} for a current pulse $i_p(t)$ varying in a HHIT circuit in the millisecond time range according to the law of the form (2)

Amplitude value I_{mp}=I_{mp1} of an unipolar millisecond aperiodic current pulse 7 ms/160 ms, A	Value of the integral of action J_{CiA} of a millisecond current pulse 7 ms/160 ms, A^2·s
100	1.17·10^3
200	4.68·10^3
300	1.05·10^4
400	1.87·10^4
500	2.92·10^4
700	5.73·10^4
835	8.15·10^4
900	0.95·10^5
1000	1.17·10^5

Then, taking into account the data of Table 6, according to (1) in the accepted approximation, one can find the critical sections S_{CCi} for uninsulated and insulated wires and cables with copper (aluminum) cores (shells), PVC, R and PET insulation, which are affected by an axial millisecond aperiodic current pulse $i_p(t)$, ATPs which correspond to the data in Fig. 2. Table 7 shows the calculated numerical values of the critical sections S_{CCi} for the indicated wires (cables) with a millisecond aperiodic current pulse $i_p(t)$ of the temporal shape 7 ms/160 ms, found as described above. Based on the relation of the form δ_{CCi}≈I_{mp}/S_{CCi}, the data of Table 7 allows us to estimate the numerical values of critical densities δ_{CCi} in wires (cables), along which a millisecond aperiodic current pulse $i_p(t)$ of a temporary shape of 7 ms/160 ms with an amplitude of I_{mp}, varying in a wide range from 100 A to 1000 A, flows in the longitudinal direction.

Table 7

Numerical values of the critical sections S_{CCi} for uninsulated wires and insulated wires (cables) with copper (aluminum) cores (shells), PVC, R and PET insulation in HHIT circuits that are affected by a millisecond current pulse of temporal shape of 7 ms/160 ms varies from 100 A to 1000 A

Type of insulation in the wire (cable) of the HHIT power circuit	Material of the core (shell) of the wire (cable)	Value of the section S_{CCi}, mm^2			
		Amplitude I_{mp} of the current pulse 7 ms/160 ms, A			
		100	500	835	1000
Without insulation, PVC, R and PET insulation	Copper	0.077	0.387	0.647	0.775
	Aluminum	0.103	0.518	0.865	1.036

From the presented in Table 7 quantitative data, it follows that the estimated critical amplitudes of the densities δ_{CCi}≈I_{mp}/S_{CCi} of a millisecond aperiodic current pulse $i_p(t)$ of the shape 7 ms/160 ms with ATPs

corresponding to the oscillogram in Fig. 2, for uninsulated wires with copper and aluminum cores, as well as wires (cables) with copper and aluminum cores (shells) having PVC, R and PET insulation, are approximately equal to 1.29 kA/mm^2 and 0.97 kA/mm^2, respectively.

6. Results of experimental verification of the calculation relations for the determination of the critical sections S_{CCi} and the current densities δ_{CCi} in the wires (cables) of the HHIT circuits. This functional test of the critical sections S_{CCi} of wires (cables) recommended for calculation determination by the relation (1) and the critical amplitudes of the pulse current densities $i_p(t)$ in their cores (shells) calculated by relation $\delta_{CCi}\approx I_{mp}/S_{CCi}$ we carry out using a powerful high-current high-voltage LCG [13] which simulates the normalized by [10] ATPs of the pulsed *A*- components of the artificial lightning current (see Fig. 1) and is equipped with verified by the state metrological service appropriate measuring equipment [15]. To do this, we first realize on the specified generator the effect of this lightning current component with ATPs normalized by requirements [10] ($I_{mp1}\approx-205$ kA; $I_{mp3}\approx-16.9$ kA; $T_p\approx200$ μs; $\Delta_p\approx\ln(I_{mp1}/I_{mp3})\approx2.495$; $t_m\approx38$ μs; $J_{CiA}\approx2.17\cdot10^6$ A^2·s) previously obtained at the load equivalent (cable brand PK 75-17-31 with a copper core of section of 10.2 mm^2), on the test sample (TS) with length of 0.55 m wire of grade ПВ-2.5 with PVC insulation and a cross-section of a split copper core equal to $S_{C1}\approx2.5$ mm^2. According to the above initial data for ATPs of the used damped sinusoidal current pulse of the microsecond range and (1), the critical section for the tested copper wire is approximately equal to $S_{CC1}\approx3.34$ mm^2. At $|I_{mp1}|\approx205$ kA, this critical section corresponds to the critical amplitude of the density of this current pulse, which is numerically equal to $\delta_{CC1}\approx61.4$ kA/mm^2. It is seen that $S_{C1}<S_{CC1}$. In this regard, it was possible to conclude before the planned experiment that the tested wire, when exposed to its copper core with cross section $S_{C1}\approx2.5$ mm^2 of the pulsed *A*- component of the lightning current with normalized ATPs, should undergo the EE and fail. Indeed, this conclusion was confirmed by the corresponding electrophysical experiment carried out on the indicated high-current LCG under the conditions of the high-voltage laboratory, the results of which applied to the nature of the abrupt change in time *t* due to the EE of the copper core with section $S_{C1}\approx2.5$ mm^2 of the tested wire of grade ПВ-2.5 with PVC insulation PVC insulation of the original current pulse $i_p(t)$ are presented in Fig. 3.

From the data in Fig. 3 it follows that the EE in the discharge circuit of the specified LCG of the copper core with cross section $S_{C1}\approx2.5$ mm^2 of grade ПВ-2.5 wire with PVC insulation causes a sharp deformation of the current pulse $i_p(t)$ flowing through it compared to its original shape (see Fig. 1). From the oscillogram in Fig. 3 it follows that the experimental value of the critical amplitude of the density δ_{CC1} of the microsecond current pulse $i_p(t)$ in the conducted electrophysical experiment is approximately $\delta_{CC1}\approx I_{mp}/S_{CC1}\approx205$ kA/3.34 mm$^2\approx61.4$ kA/mm^2. Compared with the calculated value of the critical amplitude density δ_{CC1} used in the experiment the damped sinusoidal current pulse $i_p(t)$ which equals to $\delta_{CC1}\approx I_{mp}/S_{CC1}\approx205$ kA/3.34 mm$^2\approx61.4$ kA/mm^2, the obtained experimental value of the critical current density δ_{CC1} differs from it by about 8 %.

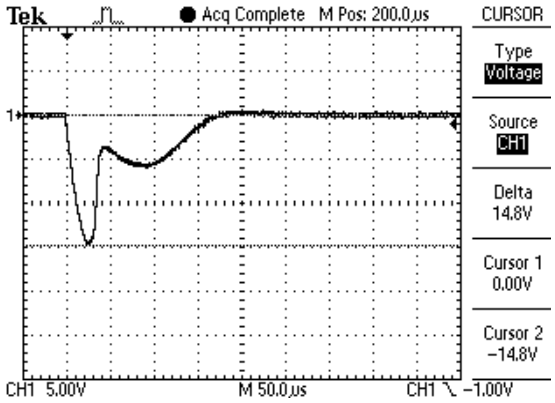

Fig. 3. Oscillogram of the pulsed *A*- component of the artificial lightning current, deformed by the EE process in the LCG discharge circuit of a split copper core with $S_{C1}\approx2.5$ mm^2 section of the tested TS of grade ПВ-2,5 wire, 0.55 m long with PVC insulation ($I_{mp1}\approx-166.7$ kA; $\delta_{CC1}\approx|I_{mp1}|/S_{C1}\approx66.7$ kA/mm^2; vertical scale – 56.3 kA/division; horizontal scale – 50 μs/division) [1, 14]

Figure 4 shows a general view of a desktop of a high-voltage high-current LCG, on which a tested on electrothermal resistibility to the action of pulsed *A*-component of an artificial lightning current with ATPs normalized by [10, 11] ($I_{mp1}\approx-205$ kA; $I_{mp3}\approx-16.9$ kA; $T_p\approx200$ μs; $t_m\approx38$ μs; $\Delta_p\approx\ln(I_{mp1}/I_{mp3})\approx2.495$; $J_{CiA}\approx2.17\cdot10^6$ A^2·s) TS of the radio frequency cable brand PK 75-4-11 with length of 0.55 m with solid copper core with section $S_C=0.407$ mm^2 and copper braid with section $S_{C2}=2.44$ mm^2 is fixed prior to exposure on it of the specified microsecond pulse current $i_p(t)$. The inner copper core and the outer copper shell-braid at the edges of this cable were connected in parallel and connected together to the discharge circuit of a high-current high-voltage LCG [14].

Fig. 4. General view of the desktop of the LCG with 0.55 m length rigidly fixed on its massive aluminum electrodes the tested radio frequency cable brand PK 75-4-11 with a solid copper core with section $S_{C1}=0.407$ mm^2 and a copper shell-braid with section $S_{C2}=2.44$ mm^2 prior to the impact on it of the pulsed *A*- component of the artificial lightning current with normalized ATPs (the core and the shell-braid at the ends of this cable were connected to the high-current discharge circuit of the LCG in parallel) [1, 14]

Figure 5 shows an oscillogram of the pulsed *A*-component of the artificial lightning current used in the experiment deformed by the EE of the copper current-carrying parts of the tested TS of the radio frequency

cable of the PK 75-4-11 brand with a total cross section of the core and braid, equal to $(S_{C1}+S_{C2})\approx 2.85$ mm^2.

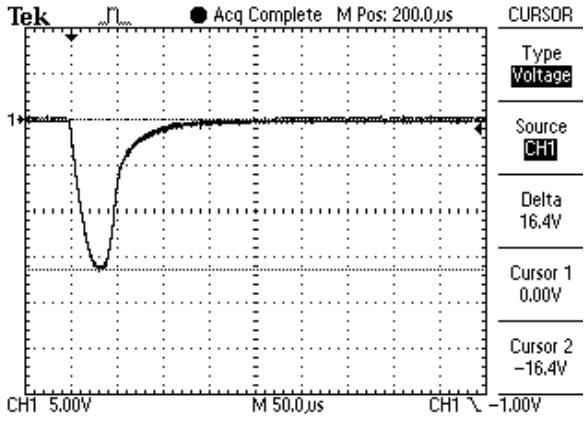

Fig. 5. Oscillogram of a pulsed *A*- component of an artificial lightning current deformed by EE in a discharge circuit of a LCG of a solid copper core with $S_{C1}\approx 0.407$ mm^2 section and a copper braid with $S_{C2}=2.44$ mm^2 section of a tested TS of a 0.55 m in length radio frequency cable PK 75-4-11 brand with PET insulation ($I_{mp1}\approx -184.7$ kA; $\delta_{CCi}\approx|I_{mp1}|/(S_{C1}+S_{C2})\approx 64.8$ kA/mm^2; vertical scale – 56.3 kA/division; horizontal scale – 50 µs/division) [1, 14]

Figure 6 shows the external view of the LCG desktop immediately after the impact of the specified current pulse $i_p(t)$ on the tested in its high-current discharge circuit TS of the cable of the brand PK 75-4-11 with PET insulation and full cross section of its copper current-carrying parts $(S_{C1}+S_{C2})\approx 2.85$ mm^2. Due to the phenomenon of the EE of its solid copper core and hollow copper shell-braid, which occurred in the TS of the cable, sublimation of its copper current-carrying parts occurred with the destruction of the belt and protective PET insulation of the test cable sample. Insulating and metal elements of the LCG were subjected to active metallization with brown-red copper vapor (see Fig. 6). On this desktop in the EE zone of the tested TS of the cable, there is the presence of small melted and charred fragments of its protective PET insulation.

Fig. 6. External view of the desktop of the LCG after the EE of the current-carrying parts of the tested in its high-current discharge circuit TS of 0.55 m long of the RF cable of the PK 75-4-11 brand with PET insulation and connected in the gap of the discharge circuit of a high-voltage generator with total cross section of its copper core and copper braid equals to $(S_{C1}+S_{C2})\approx 2.85$ mm^2 ($I_{mp1}\approx -184.7$ kA; $\delta_{CCi}\approx|I_{mp1}|/(S_{C1}+S_{C2})\approx 64.8$ kA/mm^2) [1, 14]

Due to the fact that for the tested cable of brand PK 75-4-11, the following inequality is fulfilled $(S_{C1}+S_{C2})<S_{CCi}$, its current-carrying copper parts together with PVC insulation were destroyed by the apparent in the carried out experiment the EE of the solid round core and hollow braid-shell of the selected size of the CCP. At the calculated by (1) value of a critical section for this type of cable, equal to $S_{CCi}\approx 3.34$ mm^2, the calculated critical amplitude of the density δ_{CCi} of the used in the experiment a microsecond current pulse $i_p(t)$ for it was numerically $\delta_{CCi}\approx I_{mp}/S_{CCi}\approx 61.4$ kA/mm^2. From the oscillogram in Fig. 5 it follows that the experimental value of the critical density amplitude δ_{CCi} of the specified current pulse $i_p(t)$ is numerically equal in module to $\delta_{CCi}\approx I_{mp}/(S_{C1}+S_{C2})\approx 64.8$ kA/mm^2. It can be seen that the obtained experimental value for the value of the critical amplitude of the density δ_{CCi} of a current pulse of microsecond duration in the cable under study differs from its corresponding calculated value by no more than 6%. Thus, experimental studies for a microsecond current pulse $i_p(t)$ performed on a high-current high-voltage LCG have confirmed the performance of the proposed calculation relations for determining the critical sections S_{CCi} and critical amplitudes of current densities δ_{CCi} for the specified time range in the current-carrying parts of the wires and cables of HHIT power circuits.

Conclusions. 1. The proposed electrical engineering approach allows for the condition of EE in atmospheric air of the current-carrying parts of the CCP to carry out an approximate calculation of the critical cross sections S_{CCi} and amplitudes of current densities δ_{CCi} for uninsulated wires with copper (aluminum) cores, as well as for insulated wires and cables with copper (aluminum) cores (shells) with PVC, R and PET insulation, through which the pulse current $i_p(t)$ flows, the ATPs of which varies in the nano-, micro- and millisecond time ranges.

2. On the basis of the obtained approximate calculated relations, specific capabilities of the proposed electrical engineering approach for selecting critical cross sections S_{CCi} and amplitudes of current densities δ_{CCi} in the indicated wires and cables of HHIT power circuits, in current-carrying parts of which large pulse currents $i_p(t)$ varying in time t according to aperiodic law or damped sinusoid law with the first current amplitude I_{mp1}, are demonstrated.

3. It has been determined by calculation that the critical amplitudes of densities $\delta_{CCi}\approx I_{mp1}/S_{CCi}$ of pulse current $i_p(t)$ for its considered temporal shapes in copper (aluminum) cores of uninsulated wires and insulated wires and cables with copper (aluminum) cores (shells), PVC, R and PET insulation for the nanosecond time range are numerically approximately 1176 (878) kA/mm^2, for the microsecond time range 64 (48) kA/mm^2, and for the millisecond time range 1.29 (0.97) kA/mm^2.

4. Experiments carried out using high-current high-voltage LCG with regard to the effect on the current-carrying parts of the ПВ-2,5 grade wire with PVC insulation and the cable of the PK 75-4-11 grade with PET insulation of a microsecond damped sinusoidal current pulse of artificial lightning with normalized ATPs in accordance with the requirements of acting the field of lightning protection of aerospace technology objects of

the USA SAE ARP 5412: 2013 document confirmed the performance of the recommended calculation relations for determining the critical sections S_{CCi} and amplitudes of current densities δ_{CCi} in indicated wires and cables of the HHIT circuits.

5. The results obtained for the critical cross sections S_{CCi} and current densities δ_{CCi} can also be used in the practice of implementation in the atmospheric air with the help of HHIT electrical installations of the EE phenomena of uninsulated thin metal conductors (wires) used in a number of modern applied electrophysical technologies.

REFERENCES

1. Baranov M.I. *Izbrannye voprosy elektrofiziki. Monografiya v 3 tomah. Tom 3: Teorija i praktika elektrofizicheskih zadach* [Selected topics of Electrophysics. Monograph in 3 vols. Vol. 3: Theory and practice of electrophysics tasks]. Kharkiv, Tochka Publ., 2014. 400 p. (Rus).

2. Knopfel' G. *Sverkhsil'nye impul'snye magnitnye polia* [Ultra strong pulsed magnetic fields]. Moscow, Mir Publ., 1972. 391 p. (Rus).

3. Orlov I.N. *Elektrotehnicheskij spravochnik. Proizvodstvo i raspredelenie elektricheskoj energii. Tom 3, Kn. 1* [Electrical engineering handbook. Production and distribution of electric energy. Vol. 3, Book 1. Ed. I.N. Orlov]. Moscow, Energoatomizdat Publ., 1988. 880 p. (Rus).

4. Baranov M.I. A choice of sections of electric wires and cables in circuits of devices of high-voltage high-current impulse technique. *Electrical engineering & electromechanics*, 2018, no.6, pp. 56-62. **doi: 10.20998/2074-272X.2018.6.08.**

5. Baranov M.I., Rudakov S.V. Electrothermal action of the pulse of the current of a short artificial-lightning stroke on test specimens of wires and cables of electric power objects. *Journal of Engineering Physics and Thermophysics*, 2018, vol.91, no.2, pp. 544-555. **doi: 10.1007/s10891-018-1775-2.**

6. Baranov M.I., Kniaziev V.V., Rudakov S.V. Calculation and experimental estimation of results of electro-thermal action of rationed by the international standard IEC 62305-1-2010 impulse current of short blow of artificial lightning on the thin-walled coverage from stainless steel. *Electrical engineering & electromechanics*, 2017, no.1, pp. 31-38. **doi: 10.20998/2074-272X.2017.1.06.**

7. Baranov M.I. *Izbrannye voprosy elektrofiziki: Monografija v 3-h tomah. Tom 2, Kn. 1: Teorija elektrofizicheskih effektov i zadach* [Selected topics of Electrophysics: Monograph in 3 vols. Vol. 2, book. 1: Theory of electrophysics effects and tasks]. Kharkov, NTU «KhPI» Publ., 2009. 384 p. (Rus).

8. Ricketts L.U., Bridges J.E., Mayletta J. *Elektromahnitnij impul's i metody zashchity* [Electromagnetic pulse and methods of protection]. Moscow, Atomizdat Publ., 1979. 328 p. (Rus).

9. Myrova L.O., Chepizhenko A.Z. *Obespechenie stojkosti apparatury svyazi k ionyzyruyushchim i elektromahnytnim izlucheniyam* [Ensuring stability of communications equipment to the ionizing and electromagnetic of radiations]. Moscow, Radio and Communications Publ., 1988. 296 p. (Rus).

10. SAE ARP 5412: 2013. Aircraft Lightning Environment and Ralated Test Waveforms. SAE Aerospace. USA, 2013. − pp. 1-56.

11. SAE ARP 5416: 2013. Aircraft Lightning Test Methods. SAE Aerospace. USA, 2013. − pp. 1-145.

12. Baranov M.I., Kravchenko V.I., Nosenko M.A. Experimental research into electrothermal stability of aircraft metallic elements against direct action of artificial lightning current. Part 2: stability of copper wires and cables. *Electrical Engineering & Electromechanics*, 2011, no.2, pp. 46-55. **doi: 10.20998/2074-272X.2011.2.11.**

13. Baranov M.I., Koliushko G.M., Kravchenko V.I., Nedzel'skii O.S., Dnyshchenko V.N. A Current Generator of the Artificial Lightning for Full-Scale Tests of Engineering Objects. *Instruments and Experimental Technique*, 2008, no.3, pp. 401-405. **doi: 10.1134/s0020441208030123.**

14. Baranov M.I., Kravchenko V.I. Electrothermal resistance wire and cable to the aircraft to the striking action pulsed current lightning. *Electricity*, 2013, no.10, pp. 7-15. (Rus).

15. Baranov M.I., Buriakovskyi S.G., Rudakov S.V. The metrology support in Ukraine of tests of objects of energy, aviation and space-rocket engineering on resistibility to action of pulses of current (voltage) of artificial lightning and commutation pulses of voltage. *Electrical engineering & electromechanics*, 2018, no.5, pp. 44-53. **doi: 10.20998/2074-272X.2018.5.08**.

Received 12.11.2018

M.I. Baranov, *Doctor of Technical Science, Professor,*
Scientific-&-Research Planning-&-Design Institute «Molniya»,
National Technical University «Kharkiv Polytechnic Institute»,
47, Shevchenko Str., Kharkiv, 61013, Ukraine,
phone +380 57 7076841,
e-mail: baranovmi@kpi.kharkov.ua

How to cite this article:

Baranov M.I. Calculation and experimental determination of critical sections of electric wires and cables in the circuits of devices of high-voltage high-current pulse technique. *Electrical engineering & electromechanics*, 2019, no.2, pp. 39-46. **doi: 10.20998/2074-272X.2019.2.06.**

UDC 621.3 **doi: 10.20998/2074-272X.2019.2.07**

A. Bourzami, M. Amroune, T. Bouktir

ON-LINE VOLTAGE STABILITY EVALUATION USING NEURO-FUZZY INFERENCE SYSTEM AND MOTH-FLAME OPTIMIZATION ALGORITHM

Purpose. In recent years, the problem of voltage instability has received special attention from many utilities and researchers. The present paper deals with the on-line evaluation of voltage stability in power system using Adaptive Neuro-Fuzzy Inference System (ANFIS). The developed ANFIS model takes the voltage magnitudes and their phases obtained from the weak buses in the system as input variables. The weak buses identification is formulated as an optimization problem considering the operating cost, the real power losses and the voltage stability index. The recently developed Moth-Flame Optimization (MFO) algorithm was adapted to solve this optimization problem. The validation of the proposed on-line voltage stability assessment approach was carried out on IEEE 30-bus and IEEE 118-bus test systems. The obtained results show that the proposed approach can achieve a higher accuracy compared to the Multi-Layer Perceptron (MLP) and Radial Basis Function (RBF) neural networks. References 37, tables 3, figures 10.
Key words: **voltage stability, line voltage stability index, Moth-Flame optimization, adaptive neuro-fuzzy inference system.**

В последние годы проблема нестабильности напряжения привлекла особое внимание многих служб эксплуатации и исследователей. Настоящая статья посвящена оценке в режиме онлайн стабильности напряжения в энергосистеме с использованием адаптивной нейро-нечеткой системы вывода (ANFIS). Разработанная модель ANFIS принимает в качестве входных переменных величины напряжения и их фазы, полученные от шин в системе. Идентификация шин сформулирована как задача оптимизации, учитывающая эксплуатационные расходы, реальные потери мощности и показатель стабильности напряжения. Недавно разработанный алгоритм оптимизации методом мотылька и пламени (MFO) адаптирован для решения данной задачи оптимизации. Проверка предложенного подхода к онлайн оценке стабильности напряжения в сети проводилась на тестовых системах IEEE с 30 шинами и IEEE со 118 шинами. Полученные результаты показывают, что предлагаемый подход может обеспечить более высокую точность по сравнению с многоуровневыми нейронными сетями (MLP) и нейронными сетями с радиальными базисными функциями (RBF). Библ. 37, табл. 3, рис. 10.
Ключевые слова: **стабильность напряжения, показатель стабильности напряжения сети, оптимизация методом мотылька и пламени, адаптивная нейро-нечеткая система вывода.**

Introduction. The changes in power systems' parameters such as loading, generator reactive power limits, action of tap changing transformers, load recovery dynamics and line or generator outages may cause a gradually and uncontrolled drop of voltages leading to voltage instability [1]. Several methods have been proposed for voltage stability analysis, such as modal analysis [2], sensitivity analysis [3], continuation power flow [4], and voltage stability indices [5]. However, these methods are inappropriate for on-line voltage stability evaluation due to the time consumption and computational requirement, mostly in the case of large power systems.

In recent years, the application of Artificial Neural Networks (ANNs) in voltage stability assessment has attained increasing importance. The main reasons are its ability to do parallel data processing with high accuracy and fast response [6]. Several ANN architectures have been proposed in the literature for on-line voltage stability monitoring. Debbie, et al. [6] presented an ANN-based Multi-Layer Perceptron (MLP) method for on-line voltage stability monitoring. Chakrabarti [7] developed a new method for on-line voltage stability monitoring using MLP network and regression-based technique of selecting features for training the network. A single ANN trained by the back-propagation algorithm to evaluate the voltage stability of power system incorporating FACTS devices has been proposed in [8]. Further enhancement of ANN performance in an on-line monitoring of voltage stability has been achieved by reducing the input data into an optimal size using Z-score-based algorithm [9]. It is worthwhile to note that the load real and reactive powers are generally used as the input information for the ANN. The application of ANN-based Radial Basis Function (RBF) for on-line voltage stability evaluation has been performed by several researchers [10-13]. Although the ANN has gained attention from researchers as a tool for on-line voltage stability evaluation, it requires an extensive training process and a complex design procedure [14].

The ANFIS is a powerful artificial intelligent technique that combines the advantages of fuzzy logic and neural network. It has been applied to different power system areas such as transmission line faults [15], power quality [16], frequency control [17], and power system stability [18]. One of the first voltage stability approaches in which ANFIS algorithm was applied is reported in [19]. In [20], a novel approach for voltage stability evaluation using ANFIS model has been developed. The developed method is constructed in conjunction with the input information of voltage stability indices termed as the VOSTA, while the MW distance between the operation point and the collapse point is taken as the output vector. Authors in [21] used a subtractive clustering (SC) method and ANFIS to predict the Voltage Stability Margin (VSM), where different voltage stability indices are used as input variables. The ANFIS model has been also adapted to predict the loadability margin of the power system incorporated STATCOM and SVC, the real and reactive powers at all buses are used as the input variables [22, 23]. However, for large power systems, training ANFIS model with large input features consumes large training time.

In this paper, ANFIS soft computing technique is applied with the aim of developing an on-line voltage stability evaluation model. The developed ANFIS model takes the voltage magnitudes and phase angles obtained from the weak buses in the power system as the input features. In order to identify the weak buses in the system,

an optimization problem considering the operating cost, the real power losses and the voltage stability index is formulated. The recently developed Moth-Flame Optimization (MFO) algorithm [24] is adapted to solve the optimization problem. The proposed approach is implemented on IEEE 30-bus and IEEE 118-bus test systems. The results of comparison indicate that the proposed model could achieve more accurate results than the Multi-Layer Perceptron (MLP) and Radial Basis Function (RBF) neural networks techniques.

ANFIS architecture. ANFIS introduced by Jang [25], is a machine learning technique incorporates the advantages of ANN and fuzzy logic system. The ANFIS, which is based on the Sugeno–fuzzy inference model, constructs an input–output mapping according to both fuzzy if–then rules and stipulated input–output data pairs [26]. The fuzzy if–then rules are given by the following equations [25]:

Rule 1: if x is A_1 and y is B_1

$$f_1 = p_1 x + q_1 y + r_1 , \quad (1)$$

Rule 2: if x is A_2 and y is B_2

$$f_2 = p_2 x + q_2 y + r_2 , \quad (2)$$

where x and y are the inputs, A_i and B_i are the fuzzy sets, f_i is the i^{th} output, p_i, q_i and r_i are the design parameters determined by the neural network.

Generally, the ANFIS consists of five layers configured analogously to any multi-layer feed-forward neural network. The functionality of these five layers is given as follows [25]:

- Layer 1 every node in this layer is given by:

$$O_{1i} = \mu_{Ai}(x), \ i = 1, 2; \quad (3)$$

$$O_{2i} = \mu_{Bi}(y), \ i = 1, 2; \quad (4)$$

where $\mu_{Ai}(x)$ and $\mu_{Bi}(y)$ can adopt any fuzzy membership function (MF).

- Layer 2 this second layer is considered as a rule layer. The inputs of this layer are the MFs and the outputs are given as:

$$W_i = \mu_{Ai}(x) \cdot \mu_{Bi}(y), \ i = 1, 2; \quad (5)$$

- Layer 3 the nodes in this layer play a normalization role.

$$W_i = \frac{W_i}{W_1 + W_2}, \ i = 1, 2; \quad (6)$$

- Layer 4 nodes are adaptive with node function given by Layer 1 for a first-order model, and with parameters referred to as defuzzifier of consequent parameters.
- Layer 5 consists of single node, which makes the sum of all the rules' outputs.

In this paper, ANFIS with Subtractive Clustering (SC)-based learning technique [27] has been used. The SC technique has the advantage among others clustering methods that its computation is simply proportional to the number of data points and independent of the dimension of the problem under consideration. This is a very useful feature to benefit from regarding the need of fast calculation time [21]. Details of the algorithm can be found in [28].

Determination of weak buses using Moth-Flame Algorithm MFO Optimization.

Line voltage stability index (L_{mn}). Voltage stability evaluation is currently one of the most important research areas in the field of electrical power system. Several methods have been used for voltage stability evaluation and weak buses identification, such as P-V and Q-V curves [29], continuous power flow [30] and voltage stability indices [5]. In this paper, the line voltage stability index L_{mn} [31] is used for on-line voltage stability evaluation. The L_{mn} index is defined as follows:

$$L_{mn} = \frac{4XQr}{[V_s \sin(\theta - \delta)]^2} \le 1.0 , \quad (7)$$

where X is the line reactance, Q_r is the reactive power at the receiving end, V_s is the sending end voltage, θ is the line impedance angle and δ is the angle difference between the supply voltage and the receiving voltage.

The value of L_{mn} index ranges from 0 (no load) to 1 (voltage collapse) and it must be less than 1 for stable systems.

Problem formulation. In this section the methodology to find the weak buses in an existing power system is presented. The main reason for the voltage collapse is the sag in reactive power at various locations in power system. Therefore, the weak buses in the power system can be identified as the buses which need reactive power support. In this context, the identification of the weak buses can be mathematically formulated as a non-linear optimization problem, where the main objective is the determination of the optimal location for var sources. The objective function, which has been handled by using meta-heuristic algorithms, includes the fuel cost, real power losses and voltage stability index. The general optimization problem can be written in the following form:

$$\min[f] = \sum_{i=1}^{NG} f_i + P_{Loss} + \sum_{i=1}^{NL} L_{mn} , \quad (8)$$

where f_i is the fuel cost of the i^{th} generator, NG is the number of generators in the power system.

The fuel cost curve is modeled by quadratic function as:

$$f_i = a_i + b_i P_{Gi} + c_i P_{Gi}^2 , \quad (9)$$

where P_{Gi} is the actual power produced in the i^{th} generator a_i, b_i, and c_i are the invariant factors.

The active power loss is expressed as follow:

$$P_{Loss} = \sum_{i \in NG} P_{Gi} - \sum_{j \in NL} P_{Lj} . \quad (10)$$

The L_{mn} index is considered as the third part of the objective function. The equality and inequality constraints to be satisfied while searching for the optimal solution can be described by (11) – (15). The equality constraints represent the real and reactive power equations, which are expressed as follows:

$$\begin{cases} P_{gi} - P_{di} = |U_i| \sum_{i=1}^{Nb} |U_j| \left(G_{ij} \cos \delta_{ij} + B_{ij} \sin \delta_{ij} \right); \\ Q_{gi} - Q_{di} = |U_i| \sum_{j=1}^{Nb} |U_j| \left(G_{ij} \cos \delta_{ij} + B_{ij} \sin \delta_{ij} \right) \end{cases} . \quad (11)$$

The system inequality operation constraints include:

$$P_{gi}^{\min} \le P_{gi} \le P_{gi}^{\max} ; \quad (12)$$

$$Q_{gi}^{\min} \le Q_{gi} \le Q_{gi}^{\max} ; \quad (13)$$

$$V_{gi}^{\min} \le V_{gi} \le V_{gi}^{\max};\ i = 1, 2, \ldots, N_b; \quad (14)$$

$$V_{li}^{\min} \le V_{li} \le V_{li}^{\max};\ i = 1, 2, \ldots, N_b, \quad (15)$$

where N_b is the number of buses, P_{gi} and Q_{gi} are the active and reactive power generations at i^{th} bus, P_i and Q_i are the active and reactive power demands at i^{th} bus, P_i and Q_i are the active and reactive power injections at i^{th} bus, G_{ij}, B_{ij} and δ_{ij} are the conductance, the admittance and the phase difference of voltages between the i^{th} and j^{th} bus.

The Moth-Flame Optimization (MFO) algorithm developed by Seyedali Mirjalili [24] is a novel meta-heuristic optimization technique inspired by the navigation of moths in nature called transverse orientation. In this method, moths fly in the night by maintaining a fixed angle with the moon, a very effective mechanism for traveling in a straight line for long distances [24]. However, sometimes these insects are cheated by human-made lights. Since such light is very nearly compared to the moon, using the same navigation method by maintaining an analogous angle with the light leads to a worthless spiral fly path, and the moth ultimately converges to the light as shown in Fig. 1.

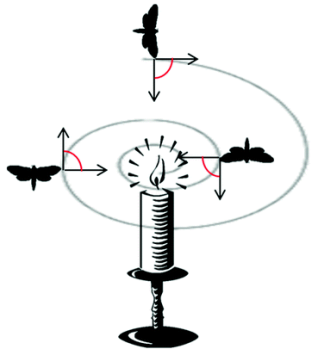

Fig. 1. Spiral flies of moths around a human-made artificial light

Moth-Flame algorithm utilizes this demeanor to achieve the optimal solutions and presumes moths as the candidate solutions and their positions in the space as the optimization problem's variables. The flames are related to the optimal solutions (positions) that moths traversed so far in the optimization process [24].

MFO algorithm is a population-based algorithm, so the set of moths is represented in a matrix M

$$M = \begin{bmatrix} m_{1,1} & m_{1,2} & \cdots & m_{1,d} \\ m_{2,1} & m_{2,2} & \cdots & m_{2,d} \\ \vdots & \vdots & \vdots & \vdots \\ m_{n,1} & m_{n,2} & \cdots & m_{n,d} \end{bmatrix}. \quad (16)$$

The set of flames can be also represented by

$$F = \begin{bmatrix} F_{1,1} & F_{1,2} & \cdots & F_{1,d} \\ F_{2,1} & F_{2,2} & \cdots & F_{2,d} \\ \vdots & \vdots & \vdots & \vdots \\ F_{n,1} & F_{n,2} & \cdots & F_{n,d} \end{bmatrix}, \quad (17)$$

where n is the number of moths and d is the number of variables.

For evaluating each moth, the fitness function should be given during optimization process, and the matrix OM and OF are employed to store the fitness value of moths and flames, respectively

$$OM = \begin{bmatrix} OM_1 \\ OM_2 \\ \vdots \\ OM_n \end{bmatrix}; \quad (18)$$

$$OF = \begin{bmatrix} OF_1 \\ OF_2 \\ \vdots \\ OF_n \end{bmatrix}, \quad (19)$$

where n is the number of moths and d is the number of variables.

In order to mathematically model the transverse orientation, the position of each moth is updated with respect to a flame using the equation

$$M_i = S\left(M_i, F_j\right) = D_i \cdot e^{bt} \cdot \cos\left(2\pi \cdot t\right) + F_j, \quad (20)$$

where M_i indicates the i^{th} moth; F_j indicates the j^{th} flame; and S is the spiral function; D indicates the distance of i^{th} moth for j^{th} flame, b is a constant for determining the shape of the logarithm spiral, and t is a random number in [–1, 1].

D_i is calculated as follows

$$D_i = \left|F_i - M_i\right|. \quad (21)$$

Another concern here is that updating the position of moths with respect to n different locations in the search space may degrade the exploitation of the best promising solutions. To resolve this concern, an adaptive mechanism is used to provide the number of flames. The following formula is utilized in this regard:

$$\text{flameno} = \text{round}\left(N - l \cdot \frac{N-1}{T}\right), \quad (22)$$

where iter is the current number of iteration, N is the maximum number of flames and max_iter is the maximum number of iterations.

The gradual decrement in number of flames balances the exploration and exploitation of the search space.

Weakest buses identification. The implementation of MFO optimization algorithm in weak locations identification is represented in Fig. 2 and summarized into the following steps:

- Step 1. Read power system data (bus data, line data, and generator data);
- Step 2. Set the values of MFO parameters such as:
  - the number of moths;
  - the maximum number of iterations;
  - the number of variables;
  - the upper and the lower bounds of variables (the real power outputs and the location of reactive power support). The candidate locations are in the range [1 N_{lb}], where N_{lb} is the number of load buses in the system;
- Step 3. Initialize the position of moths and the number of flames;
- Step 4. Update the flame number;
- Step 5. Input the positions of moths into the power flow program and compute the fitness value of each moth according to the objective function;
- Step 6. The population of moths with the optimal fitness values will be selected as the flames;
- Step 7. Update the position of moth with respect to its corresponding flame or one flame;

- Step 8. Obtain the best moth and fitness value;
- Step 9. If the stop criterion is achieved, go to the Step 10. Otherwise, repeat steps 4 to the 9;
- Step 10. The best moth comprised the best fitness value was selected and the best location for reactive power support was obtained.

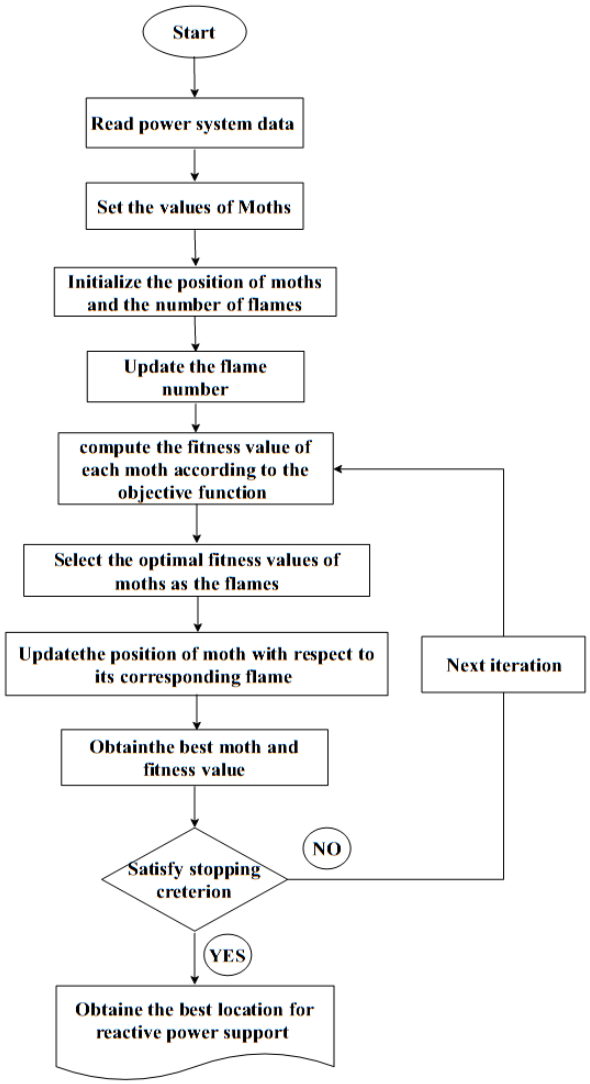

Fig. 2. Flowchart of the proposed weak buses identification method

Voltage stability Assessment Using ANFIS Model. In this section, the proposed methodology to assess the voltage stability using ANFIS model is described. The main idea of the proposed method is presented in Fig. 3. The first step in the off-line phase involves the data preparation for the training and testing steps of the ANFIS model. The training and testing data sets are generated by varying both of the real and reactive powers at all system buses. The load is increased from the base value until the system achieves the maximum loading point leads to the collapse in a power system operation. Simultaneously, the L_{mn} is calculated corresponding to the different operating points.

The voltage magnitudes and phase angles extracted from the weak buses in the system are taken as the input variables of the ANFIS model. While the maximum corresponding values of L_{mn} are considered as the output variables. In order to evaluate the performance of the proposed ANFIS model, the difference between the predicted and the actual output values was assessed according to the correlation coefficient (R), the root mean square error (*RMSE*) and the mean absolute percentage error (*MAPE*). These indices are represented by the following equations [27, 28].

$$R = \frac{\sum_{i=1}^{n}\left(a_i - \bar{a}\right)\left(P_i - \bar{P}\right)}{\sqrt{\sum_{i=1}^{n}\left(a_i - \bar{a}\right)^2 \sum_{i=1}^{n}\left(P_i - \bar{P}\right)^2}}; \quad (23)$$

$$RMSE = \sqrt{\frac{1}{n}\sum_{i=1}^{n}\left(a_i - P_i\right)^2}; \quad (24)$$

$$MAPE = \frac{100}{n}\sum_{i=1}^{n}\left|\frac{a_i - P_i}{a_i}\right|, \quad (25)$$

where a and P denote the actual output and predicted output sets, respectively, n is the total number of data.

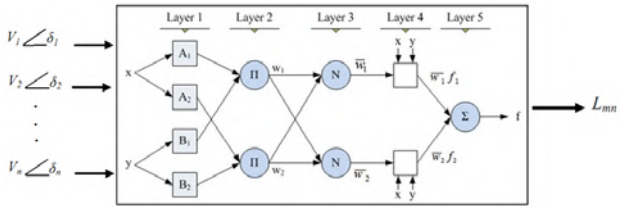

Fig. 3. Schematic of the proposed on-line voltage stability evaluation method

Simulation and results. This section presents the details of the simulation studies carried out on IEEE 30-bus and 118-bus test systems. The IEEE 30-bus power system consists of 6 generators, 41 branches, 4 tap changing transformers and 2 capacitors as shown in Fig. 4. The IEEE 118-bus system consists of 54 generators, 186 transmission lines, 9 tap changing transformers and 14 capacitors as shown in Fig. 5. The data of the generators, loads, and transmission lines for both test systems are given in [32]. The simulation was done using the computer with specification Intel® Core™ I5-2328MCPU@2.20GHz.

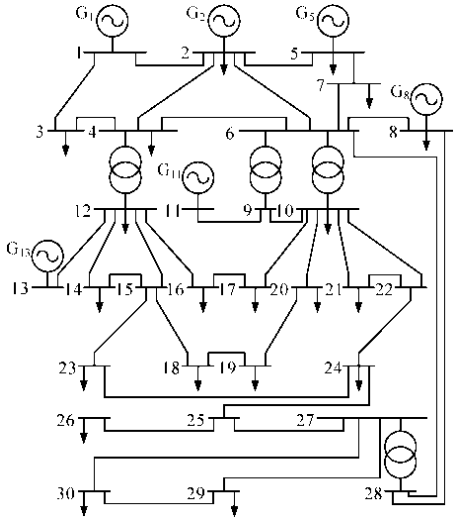

Fig. 4. Line diagram of the IEEE 30-bus system

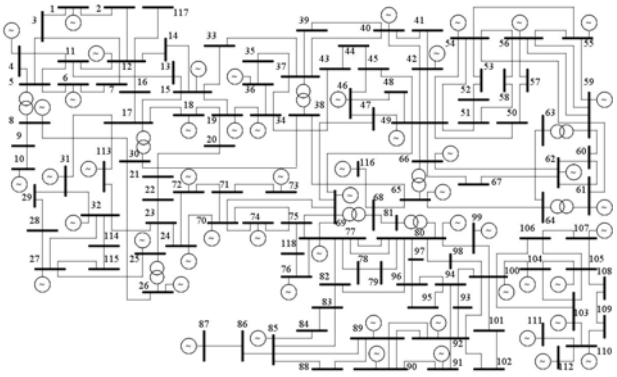

Fig. 5. Line diagram of the IEEE 118-bus system

Weak Buses Identification and Ranking. As it is mentioned above, the proposed method to find the weak buses is based on the determination of the optimal location for Var sources. The identification and the ranking of the first five weak buses in the system are performed using the MFO optimization technique where the buses are ranked starting with the most critical bus. The obtained results in the case of IEEE 30-bus system are tabulated in Table 1. This Table shows also a comparison between the results obtained by using the proposed method and the results found by other existing methods in the literature. It is clearly shown form this Table that the buses 30, 26 and 29 are identified as the weakest locations in the IEEE 30-bus test system.

Table 1

Weak buses ranking for IEEE 30-bus system

Ref [33]	30, 26, 29, 25, 27
Ref [34]	30, 26, 29, 14, 23
Ref [35]	30, 26, 29, 19, 20
Ref [36]	30, 26, 29, 21, 24
Proposed method	30, 26, 29, 28, 7

The proposed method is applied also to determine the weak buses in the 118-bus system. This power system can be regarded as a realistic transmission level power network in terms of number of buses and branches. It consists of 118 bus and 186 branches. By using the proposed method, the first five weakest buses in the 118-bus system are fond to be 118, 88, 57, 16 and 117.

Application ANFIS model in voltage stability assessment. In this section, the ANFIS-based Subtractive Clustering SC method has been developed to estimate the L_{mn} index. The input variables of ANFIS model are the voltage magnitudes and the phase angles of weak buses, while the output is the corresponding highest value of L_{mn} index. The dataset is generated, using conventional power flow, by varying the load at all buses from the base case to the collapse point. 80 % of the generated data are used as the training samples, while the rest 20 % are used to test the ANFIS model. Afterward, to evaluate the performance of ANFIS model, the difference between the predicted and actual output values were evaluated according to the correlation coefficient (*R*), the root means square error (*RMSE*) and the mean absolute percentage error (*MAPE*).

In order to generate fuzzy rules, using SC technique, it is critical to determine the adequate value of cluster radius. According to [37], good values for cluster radius are usually between 0.2 and 0.5. Table 2 presents the ANFIS model performance for different cluster radius values. It is clear from the results that the best value of cluster radius was 0.2 for both test systems.

Table 2

RMSE results under different cluster radius

Power system	Cluster radius values			
	0.2	0.3	0.4	0.5
IEEE 30-bus	$5.2437 \cdot 10^{-4}$	$8.6545 \cdot 10^{-4}$	$13 \cdot 10^{-4}$	$14 \cdot 10^{-4}$
IEEE 118-bus	$1.4285 \cdot 10^{-4}$	$2.1324 \cdot 10^{-4}$	$2.6604 \cdot 10^{-4}$	$2.5255 \cdot 10^{-4}$

Based on the above settings, the ANFIS model was trained for the base case and for the different operating conditions. Fig. 6,*a*,*b* depict the training curves of ANFIS model in the case of the IEEE 30-bus and IEEE 118-bus systems. Fig. 7, 8 shows the comparison between the calculated L_{mn} index using conventional load flow and the estimated ones in the case of IEEE 30-bus and IEEE 118-bus test systems, respectively. It is clearly seen that the ANFIS predictions are in good.

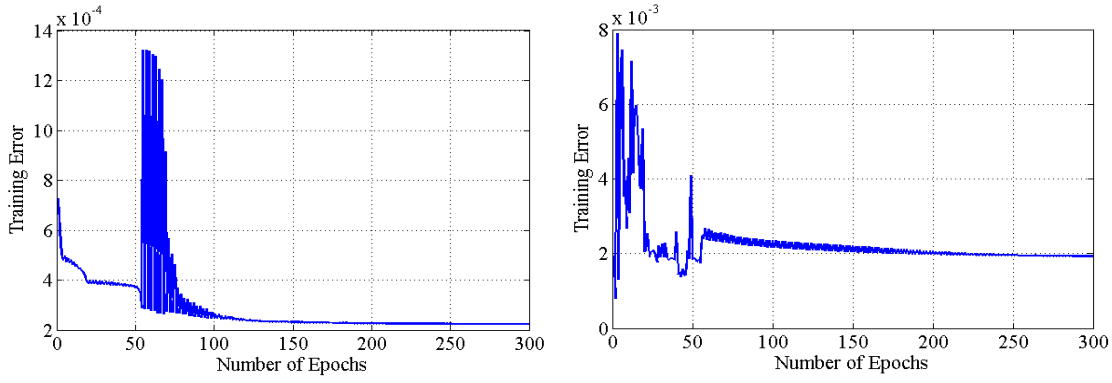

a *b*

Fig. 6. Training curves of ANFIS models in the case of IEEE 30-bus system (*a*) and IEEE 118-bus system (*b*)

Accordance with the load flow values in both steps. Fig. 9,*a*,*b* shows the testing absolute error between the L_{mn} index predicted using the ANFIS model and the L_{mn} index computed by the conventional load flow in the case of IEEE 30-bus and IEEE 118-bus test systems, respectively. It is clearly shown from this Figure that the ANFIS output values are very close to the target values with maximum absolute error equal to $0.81 \cdot 10^{-3}$ in the case of IEEE 30-bus and $1.39 \cdot 10^{-3}$ in the case of IEEE 118-bus system.

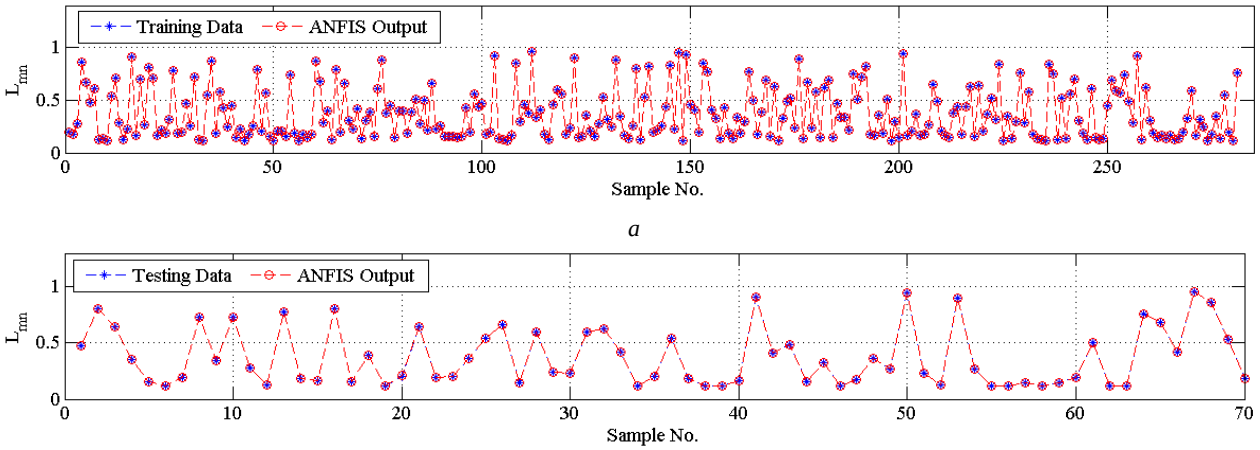

Fig. 7. Comparisons between the actual and the predicted values of L_{mn} in the case of IEEE 30-bus system, (*a*) training phase, (*b*) testing phase

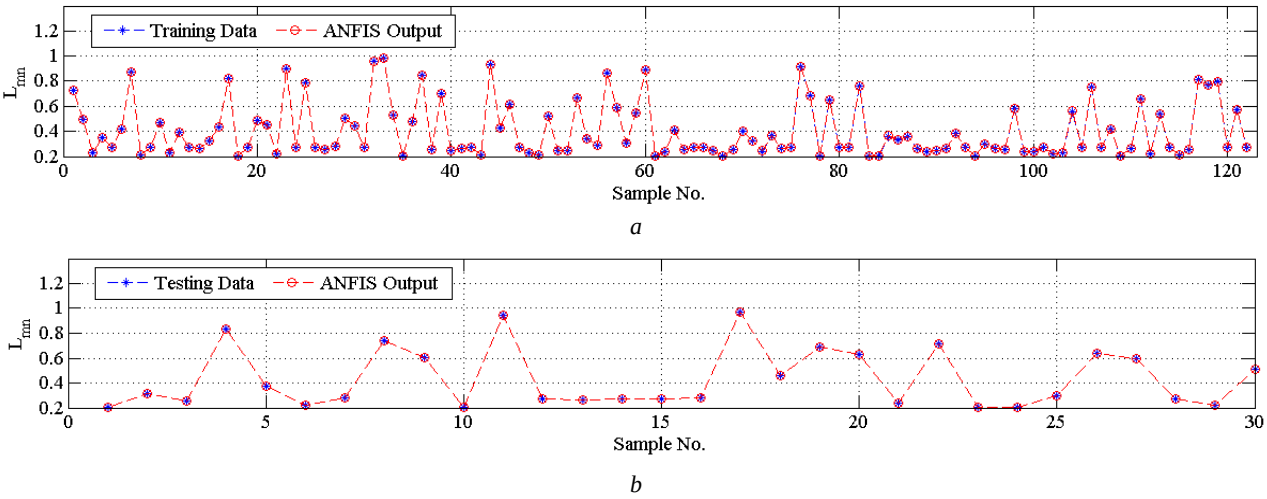

Fig. 8. Comparisons between the actual and the predicted values of L_{mn} in the case of IEEE 118-bus system, (*a*) training phase, (*b*) testing phase

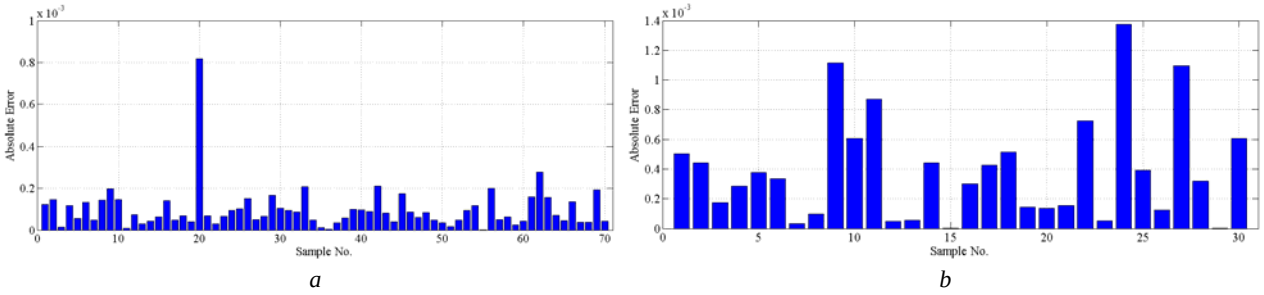

Fig. 9. Absolute error in the case of IEEE 30-bus system (*a*), IEEE 118-bus system (*b*)

Fig. 10 shows the Linear fits between the actual and the predicted values of L_{mn} index for both test systems. The ANFIS predictions yield a correlation coefficient of 0.9823 and 0.9573, in testing phase, for both the IEEE 30-bus and IEEE 118-bus cases, respectively. The obtained results revealed that the ANFIS model has a good prediction capability.

In order to further assess the performance of the ANFIS model in the prediction of the L_{mn} index, the obtained results are compared, using the same dataset, with that of Multi-Layer Perceptron (MLP) and Radial Basis Function (RBF) neural network [9, 13]. A comparison of the statistical indicators values and computation time, for the different models, is listed in Table 3. It is clearly seen, for both case studies of IEEE 30-bus and IEEE 118-bus systems, that the ANFIS model acquired relatively lower values of *RMSE* and *MAPE*, this means that the trained ANFIS model has a superior performance compared to the MLP and RBF networks.

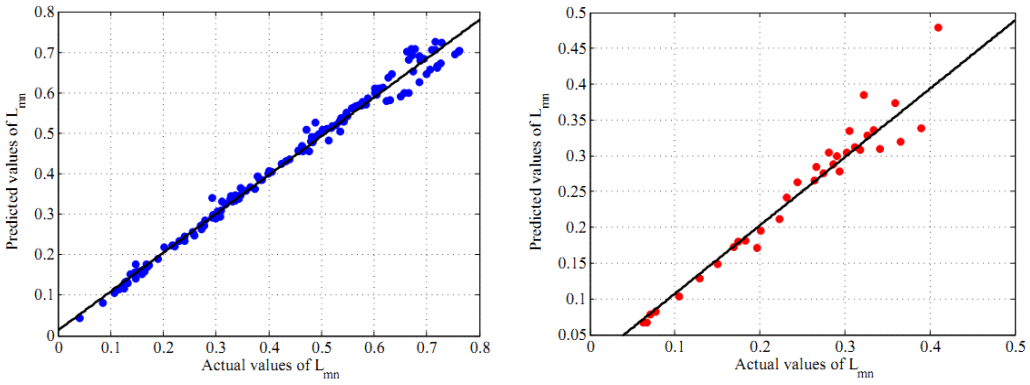

a *b*

Fig. 10. Linear fits between the actual and the predicted values of L_{mn} in testing phase for IEEE 30-bus system (*a*), IEEE 118-bus system (*b*)

Table 3

Performance Comparison of ANFIS, MLP and RBF

Power system	Performance indices	Training			Testing		
		ANFIS	MLP	RBF	ANFIS	MLP	RBF
IEEE 30-bus	RMSE	$3.01 \cdot 10^{-4}$	0.0029	0.0020	$5.24 \cdot 10^{-4}$	0.004	0.0032
	MAPE	0.0748	0.6504	0.3238	0.1090	0.9657	0.6004
	Time (s)	6.989	1.9940	0.6470	0.0800	0.0060	0.0040
IEEE 118-bus	RMSE	$9.38 \cdot 10^{-5}$	0.0025	0.0015	$1.42 \cdot 10^{-4}$	0.0025	0.0015
	MAPE	0.02700	0.8410	0.4552	0.04030	0.8833	0.4542
	Time (s)	6.2018	3.5690	1.1384	0.07980	0.0065	0.0088

Conclusion. This paper presented the application of an Adaptive Neuro-Fuzzy Inference System (ANFIS) in on-line voltage stability assessment. The input features of the developed ANFIS model were the voltage magnitudes and phase angles obtained from the weak buses in the system. The problem of weak buses identification is formulated as an optimization problem and solved using Moth-Flam Optimization (MFO) algorithm. The ability of the developed ANFIS model to predict the voltage stability margin was carried out on IEEE 30-bus and IEEE 118-bus test systems. Three statistical performance indices of correlation coefficient (*R*), root mean square error (*RMSE*) and mean absolute percentage error (*MAPE*) were considered to further assess the modeling performance. Through the comparison with MLP and RBF neural networks, the ANFIS model shows superiority in the accuracy of estimating the L_{mn} index.

REFERENCES

1. Modi P.K., Singh S.P., Sharma J.D. Voltage stability evaluation of power system with FACTS devices using fuzzy neural network. *Engineering Applications of Artificial Intelligence*, 2007, vol.20, no.4, pp. 481-491. **doi: 10.1016/j.engappai.2006.08.003**.

2. Larki F., Joorabian M., Meshgin Kelk H., Pishvaei M. Voltage Stability Evaluation of The Khouzestan Power System in Iran Using CPF Method and Modal Analysis. *2010 Asia-Pacific Power and Energy Engineering Conference*. **doi: 10.1109/appeec.2010.5448825**.

3. Xue Y., Manjrekar M., Lin C., Tamayo M., Jiang J.N. Voltage stability and sensitivity analysis of grid-connected photovoltaic systems. *2011 IEEE Power and Energy Society General Meeting*, Jul. 2011. **doi: 10.1109/pes.2011.6039649**.

4. Kojima T., Mori H. Development of nonlinear predictor with a set of predicted points for continuation power flow. *Electrical Engineering in Japan*, 2008, vol.163, no.4, pp. 30-41. **doi: 10.1002/eej.20297**.

5. Modarresi J., Gholipour E., Khodabakhshian A. A comprehensive review of the voltage stability indices. *Renewable and Sustainable Energy Reviews*, 2016, vol.63, pp. 1-12. **doi: 10.1016/j.rser.2016.05.010**.

6. Zhou D.Q., Annakkage U.D., Rajapakse A.D. Online Monitoring of Voltage Stability Margin Using an Artificial Neural Network. *IEEE Transactions on Power Systems*, 2010, vol.25, no.3, pp. 1566-1574. **doi: 10.1109/tpwrs.2009.2038059**.

7. Chakrabarti S., Jeyasurya B. On-line voltage stability monitoring using artificial neural network. *2004 Large Engineering Systems Conference on Power Engineering (IEEE Cat. No.04EX819)*. **doi: 10.1109/lescpe.2004.1356271**.

8. Jayasankar V., Kamaraj N., Vanaja N. Estimation of voltage stability index for power system employing artificial neural network technique and TCSC placement. *Neurocomputing*, 2010, vol.73, no.16-18, pp. 3005-3011. **doi: 10.1016/j.neucom.2010.07.006**.

9. Ashraf S.M., Gupta A., Choudhary D.K., Chakrabarti S. Voltage stability monitoring of power systems using reduced network and artificial neural network. *International Journal of Electrical Power & Energy Systems*, 2017, vol.87, pp. 43-51. **doi: 10.1016/j.ijepes.2016.11.008**.

10. Chakraborty K., De A., Chakrabarti A. Voltage stability assessment in power network using self organizing feature map and radial basis function. *Computers & Electrical Engineering*, 2012, vol.38, no.4, pp. 819-826. **doi: 10.1016/j.compeleceng.2012.03.012**.

11. Devaraj D., Preetha Roselyn J. On-line voltage stability assessment using radial basis function network model with reduced input features. *International Journal of Electrical Power & Energy Systems*, 2011, vol.33, no.9, pp. 1550-1555. **doi: 10.1016/j.ijepes.2011.06.008**.

12. Moghavvemi M., Yang S.S. ANN Application Techniques for Power System Stability Estimation. *Electric Machines & Power Systems*, 2000, vol.28, no.2, pp. 167-178. **doi: 10.1080/073135600268441**.

13. Hashemi S., Aghamohammadi M.R. Wavelet based feature extraction of voltage profile for online voltage stability assessment using RBF neural network. *International Journal of*

Electrical Power & Energy Systems, 2013, vol.49, pp. 86-94. **doi: 10.1016/j.ijepes.2012.12.019**.
14. Bedoya D.B., Castro C.A., da Silva L.C.P. A method for computing minimum voltage stability margins of power systems. *IET Generation, Transmission & Distribution*, 2008, vol.2, no.5, p. 676. **doi: 10.1049/iet-gtd:20070194**.
15. Reddy M.J., Mohanta D.K. Adaptive-neuro-fuzzy inference system approach for transmission line fault classification and location incorporating effects of power swings. *IET Generation, Transmission & Distribution*, 2008, vol.2, no.2, p. 235. **doi: 10.1049/iet-gtd:20070079**.
16. Senthil Kumar A., Rajasekar S., Raj P.A.-D.-V. Power Quality Profile Enhancement of Utility Connected Microgrid System Using ANFIS-UPQC. *Procedia Technology*, 2015, vol.21, pp. 112-119. **doi: 10.1016/j.protcy.2015.10.017**.
17. Pappachen A., Fathima A.P. Load frequency control in deregulated power system integrated with SMES–TCPS combination using ANFIS controller. *International Journal of Electrical Power & Energy Systems*, 2016, vol.82, pp. 519-534. **doi: 10.1016/j.ijepes.2016.04.032**.
18. Sree Varshini G.Y., Raja S.C., Venkatesh P. Design of ANFIS Controller for Power System Stability Enhancement Using FACTS Device. *Power Electronics and Renewable Energy Systems*, 2014, pp. 1163-1171. **doi: 10.1007/978-81-322-2119-7_113**.
19. Yabe K., Koda J., Yoshida K., Chiang K.H., Khedkar P.S., Leonard D.J., Miller N.W. Conceptual designs of AI-based systems for local prediction of voltage collapse. *IEEE Transactions on Power Systems*, 1996, vol.11, no.1, pp. 137-145. **doi: 10.1109/59.485995**.
20. Berizzi A., Bovo C., Delfanti M., Merlo M., Pozzi M. A Neuro-Fuzzy Inference System for the Evaluation of Voltage Collapse Risk Indices. *Bulk Power System Dynamics and Control*, 2004, pp. 22-27.
21. Torres S.P., Peralta W.H., Castro C.A. Power System Loading Margin Estimation Using a Neuro-Fuzzy Approach. *IEEE Transactions on Power Systems*, 2007, vol.22, no.4, pp. 1955-1964. **doi: 10.1109/tpwrs.2007.907380**.
22. Modi P.K., Singh S.P., Sharma J.D. Voltage stability evaluation of power system with FACTS devices using fuzzy neural network. *Engineering Applications of Artificial Intelligence*, 2007, vol.20, no.4, pp. 481-491. **doi: 10.1016/j.engappai.2006.08.003**.
23. Modi P.K., Singh S.P., Sharma J.D. Fuzzy neural network based voltage stability evaluation of power systems with SVC. *Applied Soft Computing*, 2008, vol.8, no.1, pp. 657-665. **doi: 10.1016/j.asoc.2007.05.004**.
24. Mirjalili S. Moth-flame optimization algorithm: A novel nature-inspired heuristic paradigm. *Knowledge-Based Systems*, 2015, vol.89, pp. 228-249. **doi: 10.1016/j.knosys.2015.07.006**.
25. Jang J.-S.R. ANFIS: adaptive-network-based fuzzy inference system. *IEEE Transactions on Systems, Man, and Cybernetics*, 1993, vol.23, no.3, pp. 665-685. **doi: 10.1109/21.256541**.
26. Reddy M.J., Mohanta D.K. A Wavelet-neuro-fuzzy Combined Approach for Digital Relaying of Transmission Line Faults. *Electric Power Components and Systems*, 2007, vol.35, no.12, pp. 1385-1407. **doi: 10.1080/15325000701426161**.
27. Chiu S.L. Fuzzy Model Identification Based on Cluster Estimation. *Journal of Intelligent and Fuzzy Systems*, 1994, vol.2, no.3, pp. 267-278. **doi: 10.3233/IFS-1994-2306**.
28. Chiu S. Method and software for extracting fuzzy classification rules by subtractive clustering. *Proceedings of North American Fuzzy Information Processing*, 1996, pp. 19-22. **doi: 10.1109/nafips.1996.534778**.
29. Alizadeh Mousavi O., Cherkaoui R. Investigation of P–V and V–Q based optimization methods for voltage and reactive power analysis. *International Journal of Electrical Power & Energy Systems*, 2014, vol.63, pp. 769-778. **doi: 10.1016/j.ijepes.2014.06.060**.
30. Milano F. *Continuation Power Flow Analysis. In Power System Modeling and Scripting*. Springer, Power Systems, 2010, pp. 103-130. **doi: 10.1007/978-3-642-13669-6_5**.
31. Moghavvemi M., Faruque M.O. Estimation of voltage collapse from local measurement of line power flow and bus voltages. *PowerTech Budapest 1999*. Abstract Records. (Cat. No.99EX376). **doi: 10.1109/ptc.1999.826508**.
32. Zimmerman R.D., Murillo-Sanchez C.E., Thomas R.J. MATPOWER: Steady-State Operations, Planning, and Analysis Tools for Power Systems Research and Education. *IEEE Transactions on Power Systems*, 2011, vol.26, no.1, pp. 12-19. **doi: 10.1109/tpwrs.2010.2051168**.
33. Chih-Wen Liu, Chen-Sung Chang, Mu-Chun Su. Neuro-fuzzy networks for voltage security monitoring based on synchronized phasor measurements. *IEEE Transactions on Power Systems*, 1998, vol.13, no.2, pp. 326-332. **doi: 10.1109/59.667346**.
34. Hong Y.-Y. Voltage stability indicator for identification of the weakest bus/area in power systems. *IEE Proceedings – Generation, Transmission and Distribution*, 1994, vol.141, no.4, p. 305. **doi: 10.1049/ip-gtd:19949985**.
35. Qin W., Zhang W., Wang P., Han X. Power system reliability based on voltage weakest bus identification. *2011 IEEE Power and Energy Society General Meeting*, Jul. 2011. **doi: 10.1109/pes.2011.6039270**.
36. Amroune M., Bourzami A., Bouktir T. Weakest Buses Identification and Ranking in Large Power Transmission Network by Optimal Location of Reactive Power Supports. *TELKOMNIKA Indonesian Journal of Electrical Engineering*, 2014, vol.12, no.10. **doi: 10.11591/telkomnika.v12i10.6508**.
37. Gopalakrishnan K., Ceylan H., Attoh-Okine N.O. (Eds.) *Intelligent and Soft Computing in Infrastructure Systems Engineering*. Studies in Computational Intelligence, Springer-Verlag BerlinHeidelberg, 2009. **doi: 10.1007/978-3-642-04586-8**.

Received 24.10.2018

Arif Bourzami[1],
Mohammed Amroune[1],
Tarek Bouktir[1],
[1] Department of Electrical Engineering,
University of Ferhat Abbes Setif,
1, 19000 Setif, Algeria.
phones +213658484840,
e-mail: arif.bourzami@yahoo.com,
mohammed_amroune@univ-setif.dz,
tarek.bouktir@esrgroups.com

How to cite this article:
Bourzami A., Amroune M., Bouktir T. On-line voltage stability evaluation using neuro-fuzzy inference system and Moth-Flame optimization algorithm. *Electrical engineering & electromechanics*, 2019, no.2, pp. 47-54. **doi: 10.20998/2074-272X.2019.2.07.**

UDC 621.316 **doi: 10.20998/2074-272X.2019.2.08**

V.V. Kyryk, O.S. Bohomolova

JUSTIFICATION OF OPTIMAL LOCATION OF CONNECTION OF THE DISTRIBUTED GENERATION SOURCE AND VALUE OF ITS POWER

Goal. To analyze the options for the development of the 110 kV electricity network with sources of distributed generation. Establishing the relationship between power of the source of distributed generation with the voltage changes in the nodes and transformer active power losses change. To provide the minimum value of network active power loss the authors justify the conditions for optimal connection of the source of distributed generation and value of its power. Methodology. The authors have used the DigSilent Power Factory software environment to create a 110 kV network model and have made a series of simulation of the network operating modes with solar power plants. Results. Based on the operational parameters it is established that the change in power generation in the accepted limits normally does not lead to abnormal voltage variations in the nodes, with power losses having characteristic changes due to alterations in the network of power flows. In the network with solar power plants, the transformer losses of active power is reduced with increasing generation power, except for the most remote nodes from the balancing point, in which losses reduction takes place with load of transformers approximately up to 60 %. At significant overloads of transformers (up to 130 %) there is reactive power losses increasing in comparison with losses in the network without solar power plants. The dependence of active power losses in the network on the load of transformers has a nonlinear character). For each node at one value of transformer load the active losses are different. Less reactive power losses occur at lower load ratios of transformer. When increasing the load of transformers, the rate of increase in reactive losses is higher than the active ones. Also for closed networks with voltage of 110 kV it has been found that the optimal node for connecting the distributed generation is a node with a flow division of power. If there are several such nodes in the network, the optimal one for connecting is the node with the maximum load. The optimal power of the solar station in the node should not exceed 110 % of the installed transformer's power. Originality. For the first time the dependence between the place of the best connection source of the distributed generation with the point of flow distribution with the greatest current fraction from network balancing point was established. In this case the power of the source of distributed generation must not exceed 10 % of the total power of the transformers in this node. Practical significance. We have obtained reasonable conditions for connecting source of distributed generation to a closed electric network of 110 kV without performing large volumes of mode calculations. Namely, the optimal connection point is the point of flow distribution with the greatest current fraction from network balancing point. References 8, tables 3, figures 5.

Key words: **source of distributed generation, flow distribution, load factor of transformer, power losses, voltage, power factory, solar power station.**

Висвітлено підхід до визначення потужності джерела розосередженого генерування (ДРГ) та оптимального місця його підключення для забезпечення мінімального значення втрат активної потужності в замкненій електричній мережі напругою 110 кВ. Виконано аналіз впливу потужності сонячної електростанції на режимні параметри мережі. Запропоновано критерій визначення значення потужності ДРГ в вузлах можливого підключення. Розроблено рекомендації до визначення оптимального вузла підключення джерела розосередженого генерації відповідної потужності. Бібл. 8, табл. 3, рис. 5.

Ключові слова: **джерела розподіленої генерації, потокорозподіл, коефіцієнт завантаження трансформатора, втрати потужності, напруга, сонячна електростанція .**

Освещено подход к определению мощности источника рассредоточенной генерации (ИРГ) и оптимального его подключения для обеспечения минимального значения потерь активной мощности в замкнутой электрической сети напряжением 110 кВ. Выполнен анализ влияния мощности солнечной электростанции на режимные параметры сети. Предложен критерий определения значения мощность ИРГ в узлах возможного подключения. Разработаны рекомендации к определению оптимального узла подключения источника рассредоточенного генерации соответствующей мощности. Бібл. 8, табл. 3, рис. 5.

Ключевые слова: **источники распределенной генерации, потокораспределение, коэффициент загрузки трансформатора, потери мощности, напряжение, солнечная электростанция.**

Introduction. In the united power grid of Ukraine, which is a system-forming branch, significant changes are taking place. The centralized way of functioning of the electric power system has exhausted its reserves. The cost-extensive principle of raw materials (primarily carbon and uranium) energy has led the industry to inevitably increasing costs to maintain the parameters of electrical equipment and networks within their operational reliability.

Positive changes in the development of traditional energy are undoubtedly at the minimum and further functioning can take place in the direction of: the final collapse and the achievement of the point of non-recovery and destruction of the power system; or in the direction of qualitative reformatting of the structure and philosophy of functioning of the electric power industry, orientation to the resourceless generation of renewable energy sources (RES) on the principles of virtualization, with the introduction of self-guided on the local levels «Smart Grids», with the development of distribution networks based on the introduction of new levels of voltage to reduce power losses, improvement and development of network topology.

World experience shows that with the increase of the share of distributed generation, including on the basis of

renewable energy sources, there is a need to solve a number of problems: the stochastic nature of electricity production, ensuring the reliable operation of distributed generation (DG) objects in the composition of the electricity system with a change of approach to mode-technological design, planning and management, regulation of frequency and voltage of DG objects, ensuring the reliability and quality of power supply of consumers, secured stable operation of distributed generation sources (DGS). In Ukraine, these problems are connected, on the one hand, with the state, operation and features of the construction of electric networks, on the other one – with the peculiarities of the functioning of the DGS itself in normal and emergency conditions. The introduction of DGS has a significant impact on the operation of the united power grid and requires the coordinated operation of system operators of trunk, district and distribution networks in the planning and monitoring of real-time operation modes [1].

Another problem that arises during the design phase is the choice of the optimal place for connecting the DGS to the electrical network, since this factor greatly affects the power losses in the network as a whole. The desire of the consumer to enter the power of DGS does not always coincide with the technical capabilities of the network. The difference between power losses, in the case when the DGS is connected in the optimal and least optimal nodes, may exceed 10 % [2].

In recent decades, many authors have proposed new methods for optimizing the search for the location and power of the DG source. Researchers [5] considered the problem of finding a place for the installation of DGS using a genetic algorithm to minimize the active power flow across the network. In [6], two methods for locating sources search are combined with a mix of the genetic algorithm and the simulation meta-heuristic method of selection. The authors of [7] applied the algorithm of the search tab (local search) to simultaneously search for the location of the DG source installation with the installation of a source of reactive power in the network. In [8], an optimization method based on colony of ants was proposed as a means of solving the search for places and power of DGS. For this method, the target function was minimized based on the total cost of the network.

However, determination of the optimal place of installation and power of DGS sources is not an end to the investigated issue, because in many cases, instead of the expected improvement of the parameters of the electric network, their deterioration is observed. In this regard, in the paper two important tasks are considered in the course of the introduction of DRG, namely, the search for optimal power and location of the source.

The goal of the work is to substantiate the choice of the optimal location of the source of distributed generation connection and the value of its power to provide the minimum value of active power losses in the network.

In distribution networks, the voltage drop goes along the direction of electricity supply to customers, from the main section of the power transmission line (PTL) to its end. After the DGS is installed, in such an electrical network the load on the feeder is reduced, and the voltage along the PTL may increase. Important in this case is the power factor of the DGS. The value of the voltage change depends on the location of the DGS installation, its power and $\cos\varphi$ (generation or consumption) [3].

It should also be noted that the active and reactive load of nodes varies with time, which in turn causes certain fluctuations in the voltage level in the network. In the direction from the main section to the end of the PTL, the voltage fluctuations tend to increase. If the load is concentrated mainly at the end of the PTL or remote from the balancing point, the voltage level will fluctuate more intensively [4].

The introduction of DGS into the electrical network leads to changes in its mode parameters: there is a redistribution of power over the PTL and, accordingly, change the profile of the voltage in the network. Important is the place, that is, the node of the connection of the DGS, and its power.

The installation of DGS in a closed district electrical network (DEN) with random power generation change can change the direction of power flows. In the preliminary determination of the DGS connection node and its power, it is necessary to take into account three possible situations with regard to the nodal load and the power of the DGS in the district electric network:

1. The own load of each node in the network is greater than or equal to the output power of the DGS connected to this node.

2. In DEN there is at least one node where the output power of the DGS is greater than the own load of this node, but the total power of the DGS of this DEN is in general less than its total load.

3. There is at least one node in the network where the output power of the DGS is greater than the own load of this node and the total power of the DGS of this network in general is larger than its total load.

In the first case, the installed DGS in the network will affect the reduction of power losses in the network. In the second case, DGS can permanently increase power losses in some PTLs, but overall, total power losses in DEN are reduced. In the third case, the total power losses of the entire network will be greater than before the installation of the DGS.

Thus, the installation of DGS can both increase and decrease power losses in DEN, which mainly depends on the connection nodes in the network, the power of the DGS in the network, their power factor, as well as the network topology.

To justify the expediency of optimal input of DGS power at the nodes of a closed electric network, a startup project was developed, the main idea of which is to improve an existing electricity network by connecting a new substation to provide a service for reliable electricity supply to consumers and compare possible circuits for connecting a substation to a network with competitive variants with similar technical and economic indicators. Thus, calculations of the mode parameters of five test 8-node closed networks with voltage of 110 kV of different configurations were carried out and the analysis of the

influence of distributed generation sources on the network operation mode was performed. In this case, variants of connection of DGS with possible generation power in the range from 13 to 31 MW with a 2 MW step for each of the nodes of the circuit are considered. As a conditional source of distributed generation, a solar photovoltaic station (SPS) is selected on condition of acceptable weather and territorial factors of its operation in the network, that is, the influence of generation on the system operating parameters such as voltage in nodes and power losses in the lines are considered, without taking into account the stochastic nature of the power.

The analysis of the mode parameters was performed within 80 steady operating modes, calculated in the software environment DigSilent Power Factory, for each of the five electrical networks.

Figure 1 shows one of five circuits of the electrical network, for which the analysis of the mode parameters was performed at the input of distributed generation in the network nodes.

Table 1 shows the values of the nominal voltages and powers of the transformers installed in the network nodes of the presented circuit.

Table 1

Parameters of transformers in the nodes of the network

Node No.	1	2	3	4
U_{tr}, kV	110/35/10	110/35/10	110/35/10	110/35/10
S_{tr}, MVA	25	10	10	16
Node No.	5	6	7	8
U_{tr}, kV	110/10	110/35/10	110/35/10	110/35/10
S_{tr}, MVA	10	16	10	16

Table 2 shows for the selective capacities (13, 23 and 31 MW) of the solar power plant at the network nodes the calculated voltage levels at the voltage value of 115 kV level at the balancing point «0» (BP).

From Table 2 it is shown that the change in generation power in the accepted limits does not cause excessive voltage deviations in the nodes in the normal mode, and network losses due to change in power flows have characteristic changes.

Based on the simulation data of the modes, the following graphic dependencies of the active (Fig. 2) and reactive (Fig. 3) power losses on the load of transformers in the network nodes were obtained, as well as the dependence of the losses of active power on generation power (Fig. 4).

In Fig. 2, 3 in the first node there is an uncharacteristic for other nodes decline of power losses curve. This type of curve is due to the fact that at the highest power of the transformer at this point of the network (through the power lines of the node significant power flows are flowing) at the increase in SPS power there is a significant unloading of the transformer and the reduction of power flows along the lines and, consequently, reducing the power losses in them and increase the voltage level in the node.

Table 3 shows the values of active and reactive power losses in the network when the transformers are loaded in the nodes for selective power values of the SPS.

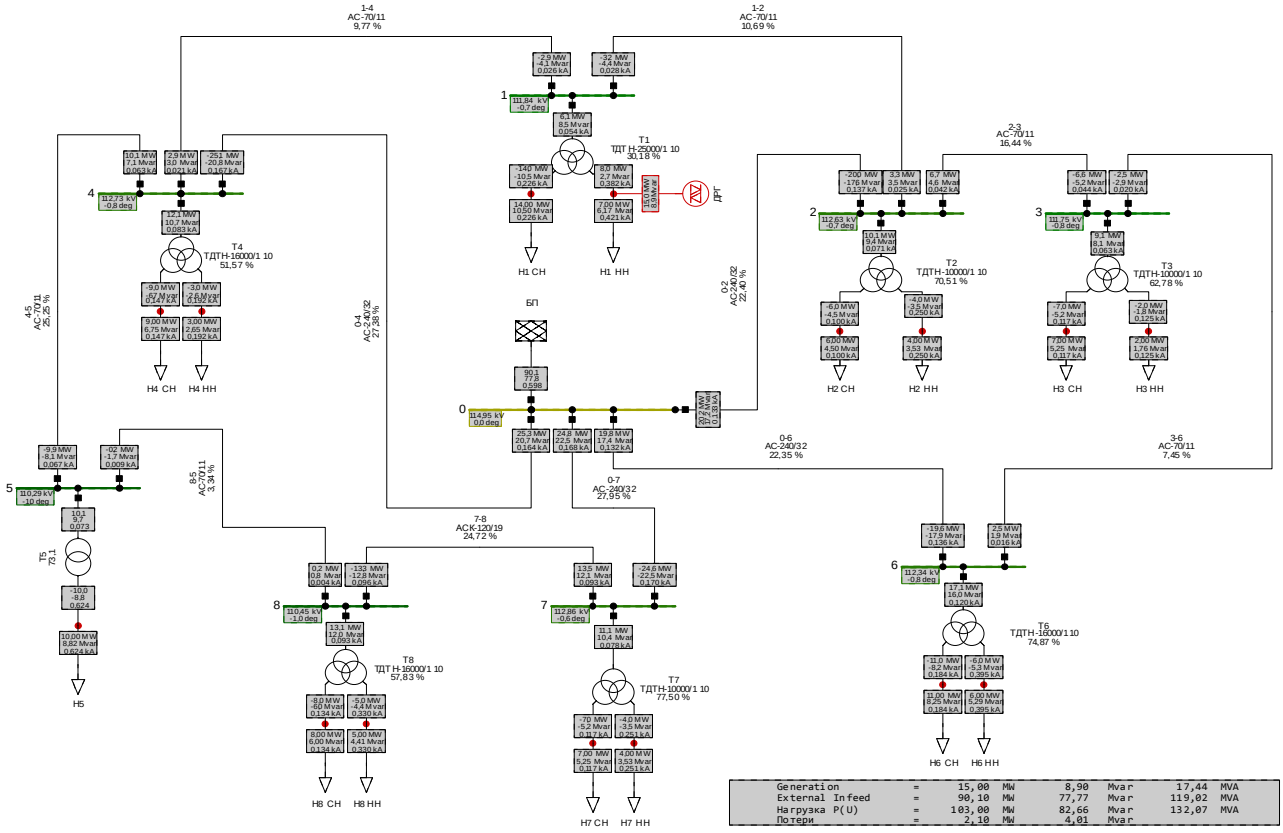

Fig. 1. Calculation model of the circuit of the electric network with DGS in the first node in the software environment DigSilent Power Factory

Table 2

Voltage values in the nodes of the circuit 110 kV

P_{SPS}	Point in which SPS is connected	U_1, kV	U_2, kV	U_3, kV	U_4, kV	U_5, kV	U_6, kV	U_7, kV	U_8, kV
1	2	3	4	5	6	7	8	9	10
0 MW	–	109.6	111.91	111.24	112.2	109.95	112.17	112.8	110.27
13 MW	1	111.56	112.54	111.68	112.67	110.25	112.32	112.85	110.43
	2	110.2	112.84	111.9	112.32	110.03	112.39	112.81	110.31
	3	110.01	112.55	112.84	112.28	110.00	112.75	112.81	110.29
	4	110.04	112.03	111.32	113	110.47	112.19	112.89	110.54
	5	109.88	111.98	111.29	112.72	112.21	112.18	113.22	111.54
	6	109.75	112.14	111.86	112.22	109.97	113.41	112.9	110.28
	7	109.64	111.92	111.24	112.28	110.37	112.17	113.64	110.93
	8	109.75	111.95	111.26	112.48	111.24	112.18	113.48	112.32
23 MW	1	112.9	112.95	112	112.98	110.45	112.41	112.88	110.53
	2	110.54	113.4	112.3	112.4	110.07	112.5	112.82	110.32
	3	110.24	112.92	113.84	112.32	110.03	113.07	112.81	110.3
	4	110.32	112.1	111.37	113.54	110.8	112.2	112.94	110.71
	5	110.06	112.03	111.32	113.05	113.74	112.2	113.48	112.36
	6	109.8	112.28	112.26	112.23	109.97	114.21	112.8	110.28
	7	109.67	111.92	111.24	112.32	110.61	112.17	114.12	111.32
	8	109.84	111.97	111.27	112.65	112.08	112.18	113.9	113.68
31 MW	1	113.9	113.27	112.19	113.2	110.59	112.48	112.9	110.6
	2	110.77	113.77	112.54	112.42	110.09	112.57	112.82	110.33
	3	110.39	113.16	114.52	112.34	110.04	113.28	112.81	110.31
	4	110.51	112.15	111.4	113.9	111.03	112.21	112.97	110.83
	5	110.18	112.08	111.34	113.29	114.85	112.19	113.67	112.98
	6	109.89	112.37	112.53	112.34	109.98	114.76	112.8	110.28
	7	109.68	111.92	111.24	112.35	110.76	112.17	114.44	111.58
	8	109.9	111.98	111.28	112.77	112.66	112.18	114.2	114.6

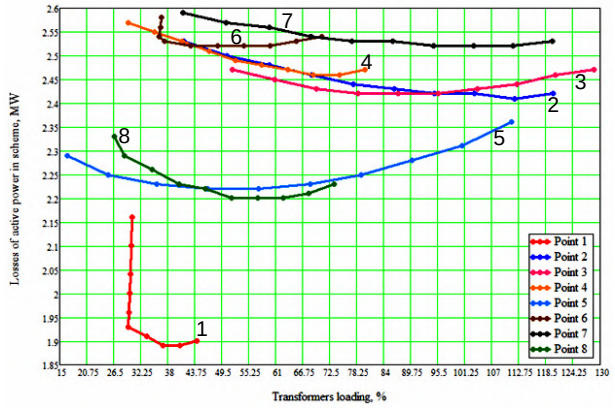

Fig. 2. Dependence of active power losses on the load of the transformer

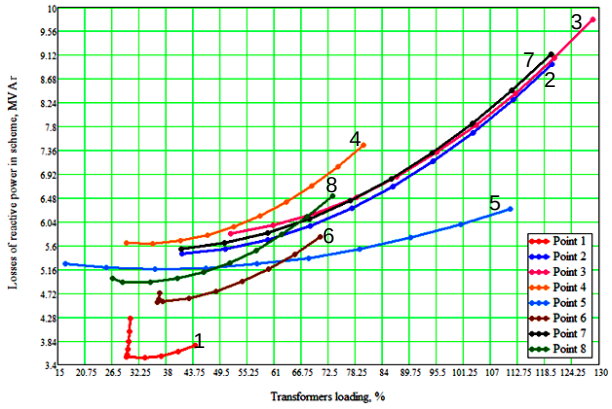

Fig. 3. Dependence of reactive power losses on the load of the transformer

In the presence of the SPS in the network, the active power losses is reduced with increasing generation power, except for the most remote nodes from the balancing point BP «0», in which the losses decrease of approximately up to 60 % of the load of transformers takes place. At significant overloads of transformers (up to 130 %) there is an increase in reactive power losses in comparison with losses in the network without power of the SPS. The dependence of active power losses in the network on the load of transformers has a nonlinear character. For each node at one value of the load of the transformer, the active losses are different. At lower load ratios, less reactive power loss occurs. When increasing the load of transformers, the rate of increase in reactive losses is higher than the active ones.

Regardless of the connection place and the generation power of the SPS, the active power losses in the network are unequivocally reduced compared to the losses in the network without the introduction of the SPS. In presented in Fig. 1 network there are two nodes 1 and 5 in which there is flow distribution of power, that is, power flows along the lines feeding the nodes are directed to them from the balancing point.

In node 1, the load is greatest compared to other nodes and is 21 % of the network load (Fig. 5). In this case, the optimum power of generation of SPS, which can be introduced into a node, should be about 29 MW at power losses at the level $\Delta S = 1.89 - j3.64$ MVA, the values of which are the smallest in comparison with losses when connecting SPS to other nodes. In the calculated

mode without the introduction of generation in the network power losses are at the level $\Delta S = 2.81 - j7.23$ MVA.

At node 5, the load is 10.2 % of the total network load. The optimal generation power of the SPS, which can be introduced into node 5, should be approximately 19 MW, with power losses at the level $\Delta S = 2.22 - j5.18$ MVA.

Table 3

Power losses in the network and load of transformers

P_{SPS}	Point in which SPS is connected	Power losses in the circuit		Load of transformers, %							
		ΔP_Σ, MW	ΔQ_Σ, MVAr	1	2	3	4	5	6	7	8
0 MW	–	2.81	7.23	59.78	71.01	63.09	51.83	73.3	75	77.55	57.93
13 MW	1	2.16	4.26	30.35	70.58	62.82	51.6	73.1	74.89	77.51	57.85
	2	2.53	5.45	59.43	41.42	62.69	51.77	73.3	74.84	77.54	57.91
	3	2.47	5.82	59.54	70.57	51.75	51.79	73.3	74.58	77.54	57.92
	4	2.57	5.65	59.53	70.93	63.04	29.65	73	74.96	77.48	57.78
	5	2.29	5.27	59.62	70.96	63.06	51.58	16.6	74.99	77.23	57.23
	6	2.58	4.72	59.69	70.85	62.71	51.82	73.3	36.68	77.54	57.93
	7	2.59	5.54	59.75	71.01	63.09	51.79	73.0	75	41.31	57.57
	8	2.33	4.99	59.69	70.99	63.07	51.69	72.4	75	77.03	26.6
23 MW	1	1.93	3.54	29.63	70.29	62.64	51.46	73	74.82	77.5	57.79
	2	2.43	6.68	59.23	86.15	62.46	51.74	73.3	74.75	77.53	57.9
	3	2.42	7.32	59.41	70.31	95.57	51.77	73.3	74.34	77.54	57.92
	4	2.48	6.15	59.36	70.88	63	58	72.7	74.97	77.44	57.89
	5	2.23	5.37	59.5	70.93	63.04	51.42	68.3	74.98	77	56.78
	6	2.52	4.75	59.64	70.75	62.48	51.81	73.3	48.64	77.54	57.93
	7	2.53	6.83	59.74	71	63.1	51.77	72.9	75	85.95	57.35
	8	2.2	5.28	59.64	70.1	63.07	51.61	71.9	74.99	76.72	51.61
31 MW	1	1.9	3.76	44.19	70.08	62.52	51.35	72.9	74.77	77.47	57.75
	2	2.42	8.95	59.1	120.06	62.31	51.72	73.2	74.71	77.53	57.9
	3	2.48	9.77	59.32	70.15	128.7	51.76	73.3	74.19	77.54	57.91
	4	2.47	7.45	59.25	70.84	62.99	79.96	72.6	74.97	77.42	57.62
	5	2.36	6.28	59.44	70.91	63.03	51.31	111.1	74.98	76.89	56.46
	6	2.54	5.76	59.61	70.69	82.32	51.81	73.3	70.79	77.55	57.93
	7	2.53	9.13	59.74	71	68.08	51.76	72.8	75	119.81	27.21
	8	2.23	6.52	59.61	70.96	63.06	51.56	71.5	74.99	76.5	73.38

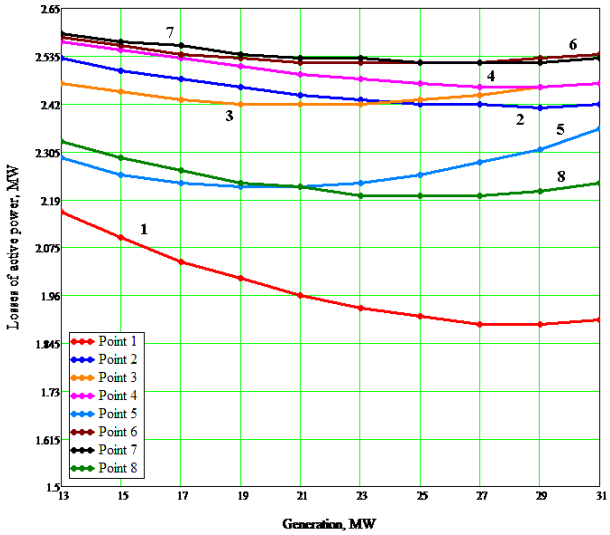

Fig. 4. Dependence of active power losses on generation power

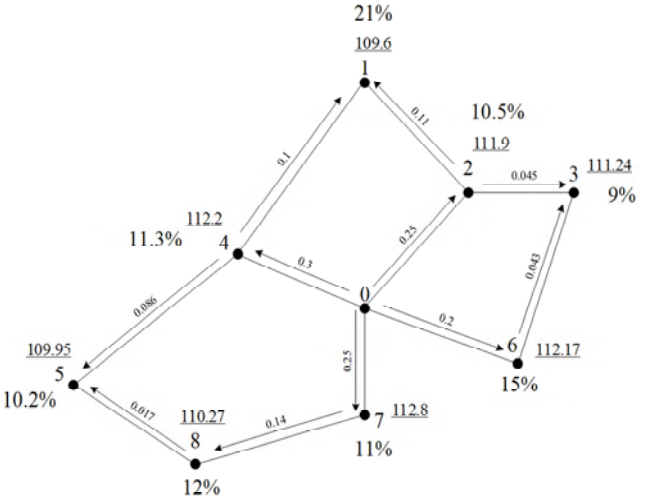

Fig. 5. The circuit of the electric network 110 kV with coefficients of flow distribution of power

Thus, for the investigated eight-node closed networks with voltage of 110 kV, a regularity has been found which confirms that the optimal node for connecting the DGS is the node in which the flow distribution of the power takes place. If there are several such nodes in the network, the optimal one for connecting is the node with the maximum load. The optimal power of the SPS in the node should not exceed 110 % of the installed transformer's power.

Conclusions.

As an optimal place to connect a source of distributed generation in a closed electric network with voltage of 110 kV, to provide the minimum value of active power losses, a node of flow distribution of power

with the largest part of its current from the balancing point can be considered.

As the optimum value of the power of the DGS in a specific node, it is possible to accept power exceeding not more than 10 % the total power of the transformers installed there.

The proposed approach will allow to perform a preliminary assessment of the location of the DGS installation and the value of its power without spending too much time for the large volumes of multivariate calculations of network operation modes.

REFERENCES

1. Pepermans G., Driesen J., Haeseldonckx D., Belmans R., D'haeseleer W. Distributed generation: definition, benefits and issues. *Energy Policy*, 2005, vol.33, no.6, pp. 787-798. **doi: 10.1016/j.enpol.2003.10.004**.

2. Kyrylenko O.V., Pavlovskyi V.V., Lukianenko L.M. Technical aspects of adoption of distributed generation sources in electric mains. *Technical Electrodynamics*, 2011, no.1, pp. 46-53. (Ukr).

3. Haesen E., Espinoza M., Pluymers B., Goethals I., Thong V.V., Driesen J., Belmans R., De Moor B. Optimal placement and sizing of distributed generator units using genetic optimization algorithms. *Electrical Power Quality and Utilisation*, 2005, vol.11, iss.1, pp. 97-104.

4. Gandomkar M., Vakilian M., Ehsan M. A combination of genetic algorithm and simulated annealing for optimal DG allocation in distribution networks. *Canadian Conference on Electrical and Computer Engineering*, 2005, pp. 645-648. **doi: 10.1109/ccece.2005.1557013.**

5. Golshan M.E.H., Ali Arefifar S. Optimal allocation of distributed generation and reactive sources considering tap positions of voltage regulators as control variables. *European Transactions on Electrical Power*, 2007, vol.17, no.3, pp. 219-239. **doi: 10.1002/etep.130.**

6. Falaghi H., Haghifam M.-R. ACO Based Algorithm for Distributed Generation Sources Allocation and Sizing in Distribution Systems. *2007 IEEE Lausanne Power Tech*., Jul. 2007. **doi: 10.1109/pct.2007.4538377.**

7. Kyrylenko O.V., Trach I.V. The technical features of the power systems functioning with integrating sources of distributed generation. *Works of the Institute of Electrodynamics of the National Academy of Sciences of Ukraine*, 2009, no.24, pp. 3-7. (Ukr).

8. Keane A., O'Malley M. Optimal Allocation of Embedded Generation on Distribution Networks. *IEEE Transactions on Power Systems*, 2005, vol.20, no.3, pp. 1640-1646. **doi: 10.1109/tpwrs.2005.852115.**

Received 14.02.2019

V.V. Kyryk[1], *Doctor of Technical Science, Professor,*
O.S. Bohomolova[1], *Assistant Lecturer,*
[1] National Technical University of Ukraine «Igor Sikorsky Kyiv Polytechnic Institute»,
37, Prosp. Peremohy, Kyiv, Ukraine, 03056,
phone +380 44 4068234;
e-mail: vkyryk@ukr.net, BohomolovaOS@ukr.net

How to cite this article:
Kyryk V.V., Bohomolova O.S. Justification of optimal location of connection of the distributed generation source and value of its power. *Electrical engineering & electromechanics*, 2019, no.2, pp. 55-60. **doi: 10.20998/2074-272X.2019.2.08.**

UDC 621.314 **doi: 10.20998/2074-272X.2019.2.09**

V.G. Yagup, E.V. Yagup

RESEARCH OF THE MODES OF FULL COMPENSATION OF REACTIVE POWER IN A THREE-PHASE POWER SUPPLY SYSTEM

Introduction *The article is devoted to the issues of current balancing and reactive power compensation in a three-phase power supply system. Optimal in all these respects is the mode of full compensation of reactive power, by which we mean such a symmetrical mode, in which only active power is consumed from the source. The task of calculating the mode of full reactive power compensation is non-linear and can be solved using non-linear optimization methods based on the adopted parameters and optimization criteria. The objective of the article is to develop a visual model of the power supply system with an unbalanced load, in which current balancing and reactive power compensation is performed using a symmetrical-compensating device, which parameters are determined using search non-linear optimization tools and modern computer mathematics software packages. The purpose of the article is to research the modes of full compensation of reactive power in a three-phase power supply system with a linear asymmetric load in order to identify the ambiguity of solving the problem of synthesizing parameters of a reactive power compensator. Methodology of research consists in the development of a visual model of a power supply system that feeds unbalanced load. As a symmetrical compensating device, capacitors connected between the phases of the transmission line are used. The model is controlled by a program that launches the model and performs optimization and selection of optimization variable values. The optimization values are the capacitors of the symmetry-compensating device. The optimization criterion is a spherical metric consisting of the reactive powers of each source of electricity. Results lead depending on the choice of the initial values of the optimization variables, the optimization process enters two modes of full compensation of reactive power – main and additional. The main mode is characterized by small values of capacitors and small values of currents, and in the additional mode, these values of the system and operational parameters reach extremely large values that are unacceptable for practical use. Originality lies in the fact that in terms of optimization theory this means that there is no global optimum in the solution of the problem of full compensation, however, there are two local optimums. Both modes are stable, as evidenced by modeling on the SPS-model of the system in the time domain in the space of state variables. Practical significance of the work lies in the fact that when designing a microprocessor system that optimizes the operating mode of the power supply system, it is necessary to envisage the situation of additional mode.*** References 10, tables 1, figures 6.

Key words: **reactive power, reactive power compensator, search optimization, visual model, three-phase power supply system.**

Розглядається рішення задачі визначення параметрів режимів повної компенсації реактивної потужності для трифазної системи з лінійним несиметричним навантаженням. Дослідження, проведені за допомогою SimPowerSystems-моделі і методу деформованого багатогранника, показали, що в залежності від початкових умов для змінних оптимізації, процес оптимізації може призводити до двох різних рішень. Основний режим повної компенсації характеризується істотним зменшенням втрат в системі. Другий же, додатковий режим повної компенсації може характеризуватися неприйнятними на практиці зростанням струмів і напруг в системі електропостачання. Бібл. 10, табл. 1, рис. 6.

Ключові слова: **реактивна потужність, компенсатор реактивної потужності, пошукова оптимізація, візуальна модель, трифазна система електропостачання.**

Рассматривается решение задачи определения параметров режимов полной компенсации реактивной мощности для трехфазной системы с линейной несимметричной нагрузкой. Исследования, проведенные с помощью SimPowerSystems-модели и метода деформируемого многогранника, показали, что в зависимости от начальных условий для переменных оптимизации, процесс оптимизации может приводить к двум различным решениям. Основной режим полной компенсации характеризуется существенным уменьшением потерь в системе. Второй же, дополнительный режим полной компенсации может характеризоваться неприемлемыми на практике возрастаниями токов и напряжений в системе электроснабжения. Библ. 10, табл. 1, рис. 6.

Ключевые слова: **реактивная мощность, компенсатор реактивной мощности, поисковая оптимизация, визуальная модель, трехфазная система электроснабжения**.

Introduction. Problem definition and justification of its relevance. Balancing currents and voltages in three-phase systems is one of the most important means of improving the quality of power supply and is an urgent task at the present stage [1, 2]. Due to balancing, the amplitudes of the currents in the feeders of the power supply system are equalized, which contributes to a uniform loading of the sources of electrical power. In addition, the amplitudes of the currents in power transmission lines are reduced, which in turn means a decrease in power transmission losses, and, consequently, an increase in efficiency is ensured [3]. Optimal in all these respects is the mode of full compensation of reactive power, by which we mean such a symmetrical mode, in which only active power is consumed from the source. In this case, the reactive component of the power consumed from the source becomes zero, which is possible when a sinusoidal current is taken from the source that coincides in phase with the sinusoidal wave generated by the sinusoidal voltage source. Thus, in the mode of full compensation of reactive power, the power factor reaches the maximum unit value [6]. For a three-phase power supply system, the full reactive power compensation mode should be extended to all three sources of electrical energy simultaneously.

Overview of recent publications on the topic. The results of solving the problem of balancing do not lead to the optimal mode, and it can be solved in the space of linear operators [1, 2]. When solving the problem of full

compensation of reactive power, the conditions of full compensation of reactive power in sources are added to the system of linear equations, and these conditions are non-linear. Therefore, in [1, 2], as well as in other sources [3-5], this problem did not find a complete solution. In the general case, the solution of the problem of full compensation of reactive power under the specified conditions is possible only with the help of optimization methods, as shown in [6]. The method of search optimization used in [6] allows to find mode parameters for the case of full compensation of reactive power using the visual model and the method of a deformable polyhedron [7]. Such a general approach opens up the possibility of studying reactive power compensation modes for power supply systems of any configuration and variations in network and load parameters.

The goal of the paper is study of modes in a three-phase power supply system with a linear asymmetric load to identify the ambiguity of solution of the problem of synthesizing parameters of the compensator in the modes of full compensation of reactive power.

Presentation of the original material of the paper. A generalized three-phase power supply system, shown in Fig. 1 is considered.

The network of infinite power (NIP) is represented by the sources of sinusoidal voltage e_a, e_b and e_c. Power transmission lines (PTL) in the form of complex resistances z_a, z_b and z_c bring energy to an asymmetrical load (AL) in the form of a star of complex resistances of an inductive nature z_{na}, z_{nb} and z_{nc}. The reactive power compensator (RPC) is represented by capacitors C_{ab}, C_{bc}, C_{ca}, connected in parallel with the load.

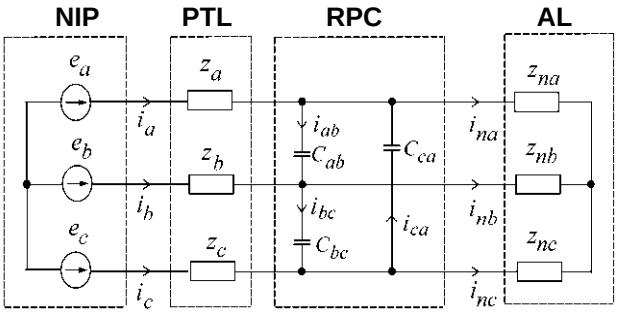

Fig. 1. Schematic circuit of a generalized three-phase power supply system

Determination of the capacitances of these capacitors is the task of synthesizing the parameters of the compensator, provided that the reactive power is fully compensated.

Main research material. The solution of the defined problem is feasible with the use of a visual model and search optimization in the SimPowerSystem (SPS) extension of the computer mathematics system MATLAB. Figure 2 shows a visual model of the power supply system.

Its appearance when using elements of the library of SimPowerSystem components practically coincides with the concept of the schematic circuit (Fig. 1).

Virtual current meters i_a, i_b and i_c are additionally introduced in PTL. The amplitudes of the voltage sources are assumed to be 100 V, the frequency of voltages is 50 Hz, $\omega = \omega = 100\pi$.

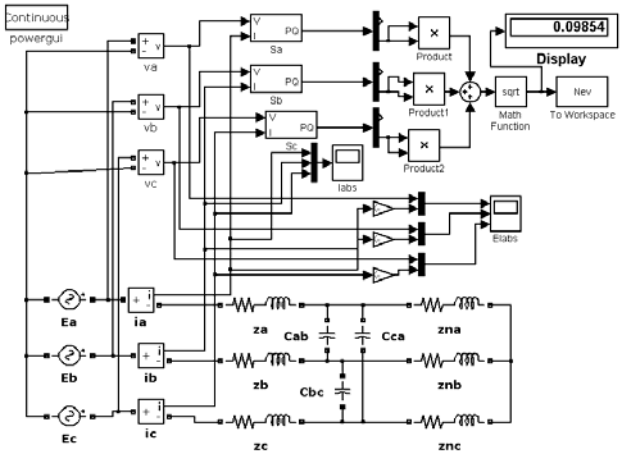

Fig. 2. Visual model of a three-phase power supply system

The complex resistances of all PTLs are assumed to be $z_a = z_b = z_c = 0.1 + j\omega 0.001$ Ω. Complex load resistances: $z_{na} = (0.7 + j\omega 0.005)$ Ω; $z_{nb} = (1 + j\omega 0.01)$ Ω; $z_{nc} = (2 + j\omega 0.04)$ Ω. With the specified parameters, the power supply mode of asymmetric load is characterized by asymmetric currents flowing in PTL:

$$i_a = 19.156 - j24.99 = 31.494e^{j(-52.536°)}\ A;$$

$$i_b = -25.84 + j17.11 = 30.995e^{j(146.495°)}\ A;$$

$$i_c = 6.69 + j7.89 = 10.342e^{j(49.705°)}\ A.$$

Virtual meters of active and reactive power, measuring the mode of the sources, give the following indicators for the total power given by the sources:

$$S_a = (957.82 + j1249.88)\ VA;$$

$$S_b = (-94.75 + j1546.84)\ VA;$$

$$S_c = (174.35 + j486.81)VA.$$

These indicators determine the following values of power factors for each of the sources of electricity:

$$\cos\varphi_a = 0.608; \quad \cos\varphi_b = -0.061; \quad \cos\varphi_c = 0.337.$$

The task mode for the first mode of full compensation of reactive power is carried out using a visual model, which is complemented by computational elements to determine the value of the objective function. The choice of the objective function itself is dictated by the formulation of the problem of complete compensation of reactive power for each of the sources of electricity.

The expression for the objective function is a spherical metric [8] composed of the reactive powers of each source of electricity:

$$N = \sqrt{Q_a^2 + Q_b^2 + Q_c^2}$$

This value is calculated in the model itself (Fig. 2), where only reactive powers are taken from the virtual *PQ* meters, which are then squared, summed, and the square root is extracted from the sum, as shown on the model.

The resulting value of the objective function is transferred to the MATLAB system workspace using the To WorkSpace virtual block, from where it becomes available for program modules.

The first program module (Fig. 3,*a*) is the main program. The optimization variables are C_{ab}, C_{bc}, C_{ca},

representing the values of the capacitances of the compensator. These variables are declared global variables in the main program. Next the call of the built-in function of unconditional nonlinear optimization fminsearch() according to the deformable polyhedron method [8] comes. As the actual parameters, it is enough to specify two parameters: the name of the file function that provides the calculation of the value of the objective function, and the array of initial values of the optimization variables.

```
global Cab Cbc Cca Nst MN XX
Nst=1
Y=fminsearch('func_s3fnesim',[1 1 1])
```

a

```
function Nev=func_s3fnesim(x)
global Cab Cbc Cca Nst MN XX
Cab=abs(x(1)*1E-6);
Cbc=abs(x(2)*1E-6);
Cca=abs(x(3)*1E-6);
sim s3fnesim2
x
Nev
Nst=Nst+1
```

b

Fig. 3. Program codes:
a – of the main program; *b* – of file functions

The text of the second program module is shown in Fig. 3,*b*. The first line repeats the declaration of global variables. Next the operators are placed expressing the actual values of the capacitances of the compensator through the elements of the array of optimization variables. It is advisable to use the scale factor that converts the values of x optimization variables, expressed in microfarads, to the values of capacitances C_{ab}, C_{bc}, C_{ca}, expressed in farads. This ensures that it is possible to avoid optimization on a set of optimization variables whose values approach zero.

After scaling, the sim operator follows, calling the visual model of the power supply system with a compensator to be executed. For the linear system under consideration, it is enough to run the model for only one period of the supply voltage, since for linear SPS-models, the default is a preliminary calculation of the steady state. During the SPS-model run, the value of the objective function is found during the period, which is then used by the optimization program itself.

The selection of the initial values of the optimization variables influences the progress of the optimization process. In the first variant, the vector $\boldsymbol{x}$ = [1, 1, 1] was adopted as the initial values of the variables of the optimization of the vector of initial values, that is, the capacitances of the capacitors were taken at the beginning of optimization $C_{ab} = C_{bc} = C_{ca} = 1$ μF.

Such a choice is explained by the desire to start optimization from the depicting point of the trajectory of the optimization process, separated from the initial asymmetrical mode at an insignificant distance. Indeed, the connection of such small capacitances does not have a significant impact on the original mode, and thus ensures a smooth transition from the initial mode to the optimization process. In this case, the optimization process ended after 268 runs of the SPS-model and led the solution to the following capacitor values of the compensator capacitances:

C_{ab} = 562.2 μF; C_{bc} = 182.3 μF; C_{ca} = 34.4 μF.

The amplitudes of the currents in PTLs with this became equal:

$$I_{am} = I_{bm} = I_{cm} = 7.754 \text{ A}.$$

Thus, the mode of full compensation of reactive power allowed to reduce active losses in phases A, B, C, respectively, by 16.5, 2.16 and 21.78 times in comparison with the asymmetric mode.

The progress of the optimization process when the first mode is found clearly reflects the dependence of the value N of the objective function on the sequence number k of the SPS-model call per run (Fig. 4). Here you can clearly see the intervals of the graph, which are characterized by minor changes in the objective function, namely:

a) interval k = 0 … 40;
b) interval k = 60 ... 180;
c) interval k = 230 ... 268.

Obviously, the first interval k = 0 ... 40 is due to the increase in the values of the capacitances of the compensator from insignificant unit initial values to values at which they begin to significantly affect the reduction of reactive power in the power supply system.

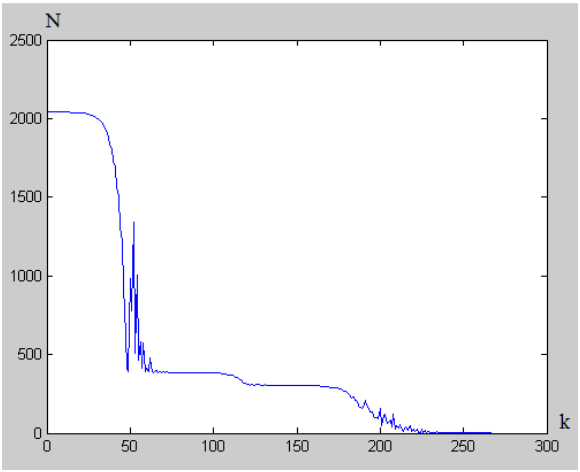

Fig. 4. Dependence of the objective function N on the number of optimization step k when finding the main mode of full compensation

The second interval is likely due to the peculiarities of the multidimensional surface, which reflects the behavior of the objective function on the set of values of the optimization variables. This interval takes about 120 calls to the SPS-model. The third interval for k = 230 ... 268 is due to bringing the already small value of the objective function to a value that satisfies the conditions of a given accuracy of reaching the solution. It can be changed by the option of running the fminsearch() optimization program itself. The analysis of the peculiarities of the considered optimization process led to the search for other initial values of the optimization variables that would shorten the solution time, providing a more favorable trajectory of the decision representation point.

The solution of the problem for the second mode of full compensation of reactive power is carried out with the setting of significant initial values of the optimization variables. At the same time, the possibility of an accelerated arrival to the optimal solution from the practically short-circuit mode of the system with a reactive power compensator was expected.

For this purpose, the vector $\boldsymbol{x}$ = [4000, 4000, 4000] was selected as the initial one, which corresponds to the capacitance values $C_{ab} = C_{bc} = C_{ca} = 4000$ μF.

The corresponding plot of the value N of the objective function versus the sequence number k of the call to the SPS-model is shown in Fig. 5.

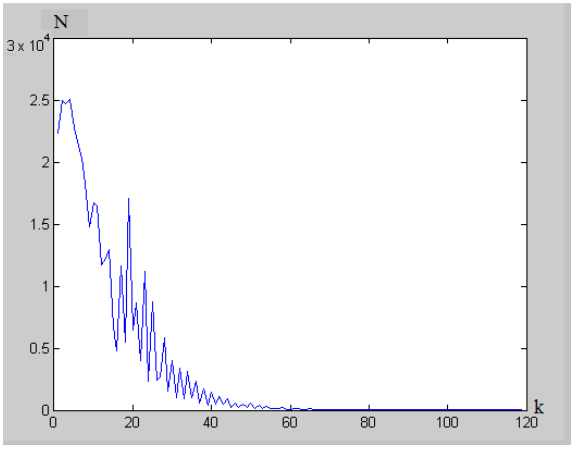

Fig. 5. Dependence of the objective function N on the number of optimization step k when finding the additional full compensation mode

As can be seen from the graph, the number of calls to the SPS-model has decreased by more than 2 times. Over 120 calls, a solution was reached in which the value of the objective function N = 0.212. In fact, already over 60 calls, a small value of N was reached and the interval for k = 0 ... 60 is characterized by a continuous decrease in the objective function and the absence of horizontal sections in the plot, as observed in the previous case. The solution obtained under these conditions, however, is characterized by relatively large values of the optimization variables at the solution point, which correspond to the following values of the compensator capacitances:

C_{ab} = 3935.3 μF; C_{bc} = 3555.5 μF; C_{ca} = 3407.7 μF.

Figure 6 shows the temporal diagrams of currents in PTL with the specified parameters of the compensator. Here you can see that the currents are really balanced in amplitude and shifted by 120 electrical degrees relative to each other at a zero phase angle for phase A. Therefore, the power factors characterizing the operation of each source of electricity constitute the maximum unit value, which corresponds to the mode of full compensation of reactive power in the system.

The found second mode of full compensation of reactive power can be called additional, since it is characterized by extremely large values of the amplitudes of consumed currents. The amplitudes of the currents in PTL amount to 928.4 A. This is more than two orders of magnitude greater than the amplitudes of 7.754 A for the first main mode.

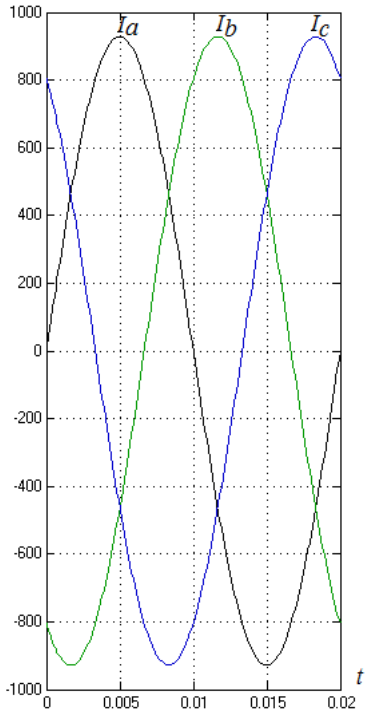

Fig. 6. Temporal diagrams of currents in PTL in the additional mode

The summarizing Table 1 presents a comparison of system and mode parameters characterizing both modes of full compensation of reactive power for the considered generalized three-phase system.

Table 1

Values of system and mode parameters in the main and additional modes

Parameters	Main mode of full reactive power compensation	Additional mode of full reactive power compensation
Capacitor capacitance C_{ab} (μF)	562.2	3935.3
Capacitor capacitance C_{bc} (μF)	182.3	3555.5
Capacitor capacitance C_{ca} (μF)	34.1	3407.7
Current amplitude in PTL (A)	7.754	928.4
Load voltage amplitude (V)	99.25	291.8
Power supplied by each source of electricity (W)	387.7	46420

Regarding the question of the adequacy of the results obtained, it can be noted that the existence of an additional mode of full compensation, as well as its stability, is fully proved by modeling on the SPS-model in the time domain, where the system, being dissipative [9], is described by differential equations in the space of state variables [10]. The question of the implementation of this mode for the considered option in practice will be complicated by the need to install very large capacitances of the compensator, to ensure the flow of large currents in the system, etc. However, with certain parameters of the

system, the points characterizing both modes of full compensation may not be so separated by system and mode parameters. In such cases, the practical significance of the proposed approach will be that the implementation of both modes can be quite feasible in practice. Then the question of choosing the full compensation mode, which is characterized by more rational technical and economic indicators, will certainly arise.

Conclusions.

The studies performed suggest that the search optimization method using the SPS-model showed the possibility of the existence of two modes of full compensation of reactive power in a three-phase power supply system. In terms of optimization theory, this means that there is no global optimum in the solution of the full compensation problem, but there are two local optima. Physically, this is due to the ambiguity of the solution of the problem of synthesizing the parameters of the compensating device. Modeling in the state space confirms the stability of both modes, which are characterized by the maximum value of the power factor.

REFERENCES

1. Arrillaga J., Watson N.R., Chen S. *Power system quality assessment*. John Wiley, 2000. 300 p.

2. Acha E., Agelidis V.G., Anaya-Lara O., Miller T.J.E. *Power Electronic Control in Electrical Systems.* Newnes, 2002. 443 p. **doi: 10.1016/B978-0-7506-5126-4.X5000-7**.

3. Hofmann W., Schlabbach J., Just W. *Reactive Power Compensation: A Practical Guide*. John Wiley & Sons, 2012. 274 p.

4. Azzam M., Mousa A.A. Using genetic algorithm and TOPSIS technique for multiobjective reactive power compensation. *Electric Power Systems Research*, 2010, vol.80, no.6, pp. 675-681. **doi: 10.1016/j.epsr.2009.10.033**.

5. Jeon S.-J., Willems J.L. Reactive power compensation in a multi-line system under sinusoidal unbalanced conditions. *International Journal of Circuit Theory and Applications*, 2011, vol.39, no.3, pp. 211-224. **doi: 10.1002/cta.629**.

6. Yagup V.G., Yagup E.V. *Primenenie optimizatsionnykh metodov dlia resheniia zadach uluchsheniia pokazatelei elektricheskikh sistem* [The use of optimization methods for solving problems of improving the performance of electrical systems]. Kharkiv, KNAME of A.N. Beketov Publ., 2017. 170 p. (Rus).

7. Chapra S.C., Canale R.P. *Numerical methods for engineers*. McGraw Hill, Higher Education, 2006. 926 p.

8. Nathews J.H., Fink K.D. *Numerical methods*. Prentice Hall, Upper Saddle River, 2001. 720 p.

9. Friedland B. *Control system design: an introduction to state-space methods (Dover Books on Electrical Engineering)*. Dover Publications Inc. Mineols, New York, 2005. 620 p.

10. Chernykh I.V. *Modelirovanie elektrotekhnicheskikh ustroistv v MATLAB, SimPowerSystems i Simulink* [Modeling of electrical devices in MATLAB, SimPowerSystems and Simulink]. Moscow, Peter Publ., 2008. 288 p. (Rus).

Received 21.01.2019

V.G. Yagup[1], *Doctor of Technical Science, Professor,*
E.V. Yagup[1] *Doctor of Technical Science, Associate Professor,*
[1] O.M. Beketov National University of Urban Economy in Kharkiv,
17, Marshal Bazhanov Str., Kharkiv, 61002, Ukraine,
phone +380 57 7073114,
e-mail: kata3140@gmail.com

How to cite this article:
Yagup V.G., Yagup E.V. Research of the modes of full compensation of reactive power in a three-phase power supply system. *Electrical engineering & electromechanics*, 2019, no.2, pp. 61-65. **doi: 10.20998/2074-272X.2019.2.09.**

UDC 621.315 **doi: 10.20998/2074-272X.2019.2.10**

Yu.N. Shumilov, V.I. Bondarenko

INVESTIGATION OF EXPLOSION SAFETY OF DC POLYMER SURGE ARRESTERS 3.3 KV FOR TRACTION NETWORK OF RAILWAY TRANSPORT

In the testing laboratories of Ukraine, there is no high-voltage equipment of the necessary energy for testing surge arresters for explosion safety, which does not allow to estimate this indicator at the stage of development of prototypes. In view of this test, the polymer prototypes of the DC surge arresters in polymer case (SAp) 3.3 kV were tested under the operating conditions of the equipment of the operating substation with short-circuit currents of 8.3 kA and a current time of 0.02 seconds, close to the recommended by Standard of IEC 60099-4:2014 values. 8 samples of surge arresters were tested. A sample of the surge arrester was mounted on one of the metal supports at a height of 5.5 m located in the substation and connected to the 3.3 kV traction substation buses through disconnectors and a high-speed switch. After the short-circuit breaker was closed through a column with a pre-punched or shunted copper wire varistor, a short-circuit current flowed to form an electric arc inside the arrester samples. During the tests video samples were recorded using a video recorder installed in close proximity to the test sample. The frame of the SAp samples in which the varistors were enclosed was performed either by winding the fiberglass tape on a varistor column, or from rods arranged in the form of a squirrel cage, or in the form of a fiberglass tube with a hole for gas ejection during a short circuit inside the SAp. The destruction of the hull occurred without scattering of the fragments in seven cases from the eight samples tested. In seven samples, a local rupture of the silicone shell occurred in the varistor zone, a gas ejection and an arc discharge occurred through this gap. The exception was sample No. 2, made by a continuous winding of a glass-banding tape on a varistor column, in which, during the explosion, the upper electrode exploded with the simultaneous expansion of fragments of the varistor in a radius of 3-5 m. Due to the white smoke accompanying the explosion, it was not possible to fix on the frame whether the arc output from the case to the outside, despite the fact that on the next frame (in 33 ms.) the arc was no longer fixed. In the tests of eight of the presented designs, none of them ignited the hull. If the tests were carried out on the surge arresters assembled with pre-punched varistors (electrothermal breakdown), the varistors during the tests split, remaining inside the frame. From the action of the arc in the contact zone of the aluminum electrodes with varistors, a deep burn-out of the electrodes was observed, in some cases, the burnup was up to 7 mm deep and up to 8 mm wide. If the varistors were shunted by a copper wire, they remained intact. If the varistors were shunted by a copper wire, they remained intact und melting and burning out a part of the aluminum electrodes in the area of connection with the copper wire were smaller sizes. The samples showed a completely satisfactory ability to withstand large pulse currents without dispersing dangerous fragments for personnel and surrounding equipment. However, polymer designs, the frame of which is made by continuous winding, require reinforcement of the connection zone of the carcass with electrodes to exclude the break-out of electrodes during the accumulation of gases during a short circuit inside the shell of the SAp. For such designs, an additional test for mechanical strength in the longitudinal direction with a predetermined norm is required in the acceptance test program. References 11, tables 1, figures 5.

Key words: **electrical equipment of traction network, direct current, overvoltage protection, surge arrester, explosion safety, test procedure, explosive destruction, fragment separation.**

Проведено випробування полімерних зразків ОПН-3,3 кВ в експлуатаційних умовах на обладнанні діючої підстанції, при токах короткого замикання 8,3 кА і часу впливу струму 0,02 с, близьких за величиною до рекомендованих стандартом IEC 60099-4:2014 значень. Випробувано 8 шт. обмежувачів перенапруг. Каркас, в якому були укладені варистори, виконувався або шляхом намотування склопластикової стрічки на варисторну колонку, або стрижнів, розташованих у вигляді «білячої клітини», або склопластикової труби з отвором для викиду газів при короткому замиканні всередині ОПН. Зразки показали цілком задовільну здатність витримувати великі імпульсні струми без розльоту небезпечних для персоналу і навколишнього обладнання фрагментів. Полімерні конструкції, каркас яких виконаний суцільним намотуванням, вимагають посилення зони з'єднання каркаса з електродами для виключення вильоту електродів при скупченні газів при короткому замиканні всередині корпусу ОПН. Для таких конструкцій потрібне введення в програму приймально-здавальних випробувань додаткової перевірки на механічну міцність в поздовжньому напрямку з заздалегідь встановленої нормою міцності. Бібл. 11, табл. 1, рис. 5.

Ключові слова: **електрообладнання тягових пристроїв, постійний струм, захист від перенапруг, обмежувачі перенапруг, вибухобезпечність, методика випробувань, вибухове руйнування, розліт фрагментів.**

Проведены испытания полимерных образцов ОПН-3,3 кВ в эксплуатационных условиях на оборудовании действующей подстанции, при токах короткого замыкания 8,3 кА и времени воздействия тока 0,02 с, близких по величине к рекомендуемым стандартом IEC 60099-4:2014 значениям. Испытано 8 шт. ограничителей перенапряжений. Каркас, в котором были заключены варисторы, выполнялся либо путём намотки стеклопластиковой ленты на варисторную колонку, либо из стержней, расположенных в виде «беличьей клетки», либо в виде стеклопластиковой трубы с отверстием для выброса газов при коротком замыкании внутри ОПН. Образцы показали вполне удовлетворительную способность выдерживать большие импульсные токи без разлёта опасных для персонала и окружающего оборудования фрагментов. Полимерные конструкции, каркас которых выполнен сплошной намоткой, требуют усиления зоны соединения каркаса с электродами для исключения вылета электродов при скоплении газов при коротком замыкании внутри корпуса ОПН. Для таких конструкций требуется введение в программу приёмо-сдаточных испытаний дополнительной проверки на механическую прочность в продольном направлении с заранее установленной нормой прочности. Библ. 11, табл. 1, рис. 5.

Ключевые слова: **электрооборудование тяговых устройств, постоянный ток, защита от перенапряжений, ограничители перенапряжений, взрывобезопасность, методика испытаний, взрывное разрушение, разлёт фрагментов.**

Introduction. To protect against overvoltages the electrical equipment of traction devices, electric locomotives and electric trains dischargers or surge arresters (SA) are used.

Currently, in most cases, dischargers РМВУ-3,3; РВКУ-3,3 А 01 [1-3] on electrical equipment are installed, made of vilite disks and spark gaps, as well as

surge suppressors in porcelain cases. Vilite dischargers are morally obsolete and are in fact out of production; porcelain surge arresters have several disadvantages: insufficient tightness of the connection between a porcelain tire and a metal flange, high explosion hazard, large dimensions and weight. To eliminate the above disadvantages, for the replacement of porcelain structures for the DC railroad surge arresters in a polymer case (SAp) are designed and mastered. When developing new SAp, it is taken into account that their most important indicator is explosion safety. Surge arresters, like any apparatus, can be damaged in operation, for example, due to internal breakdown of varistors, which can lead to short circuit and electric arcs inside the case, a sharp increase in internal gas pressure from thermal decomposition of materials caused by an electric arc. If damage to the SA is accompanied by an explosive destruction of the case, then this is a danger to the substation personnel and the equipment located near it, since the explosion can fragment the varistors and the hard parts of the exploded case at high speed. Metal flanges can also escape from the SAp case. When installing the SAp on electric locomotives and electric trains, the danger of explosive destruction of the SA is aggravated by the fact that the fragmentation of fragments can occur in crowded places. According to [4], for all types of SA, explosion safety is defined as the absence of an explosive destruction of a case with fragmentation in the normalized zone when tested, and the absence of case ignition during destruction and, if it occurs, followed by flame attenuation during a time not longer than 30 s.

For a SA of a DC network, test modes for confirming the explosion safety are defined in [5]. In the Ukrainian testing laboratories there is no high-voltage equipment for high currents for testing the SA for explosion protection in short-circuit modes. At the same time, when preparing the Specifications for these products, confirmation of compliance with the requirements of [6] is required, in which the explosion safety of the apparatus is the most important indicator.

The goal of the work is the determination of the explosion safety of SAp-3.3 kV samples with a polymer case on the equipment of an operating DC traction substation under conditions as close as possible to operation.

Samples for testing. 8 samples of surge arresters SAp-3.3/4.5 /10/550 of the contact network, consisting of a column «varistor + aluminum inserts + aluminum electrodes», fiberglass frame and silicone organic ribbed protective shell passed the necessary electrical and mechanical tests, were tested.

In samples No. 1-3, the frame is made by continuous winding of a glass band tape impregnated with a thermosetting binder. In samples No. 4-6, the frame is made by winding glass band tape, providing for the presence of sections with incomplete closure by the glass band tape of the lateral (cylindrical) surface of the varistor column. After the tape was applied, the frame was baked at temperature of 165 °C, then its surface was sanded and coated with a special primer for strong bonding of silicone rubber with glass tape before applying the silicone shell.

In sample No. 7, the frame is made in the form of a «squirrel cage» consisting of thin fiberglass rods located around the varistor and firmly fixed by molding in aluminum electrodes.

In sample No. 8, the frame is assembled from a prefabricated fiberglass pipe with two holes in the side surface, designed to release gas pressure during the breakdown of SAp; the flanges were fixed on a fiberglass pipe using a glue-thread connection.

To create a short circuit in samples No. 3-6, 8, the varistor was shunted by copper wire with cross section of 0.62 mm^2; in samples No. 1, 2, 7, the varistor experienced preliminary electrothermal breakdown, but was not destroyed.

Figure 1 shows schematically columns of samples with varistors prepared for the application of a silicone protective shell.

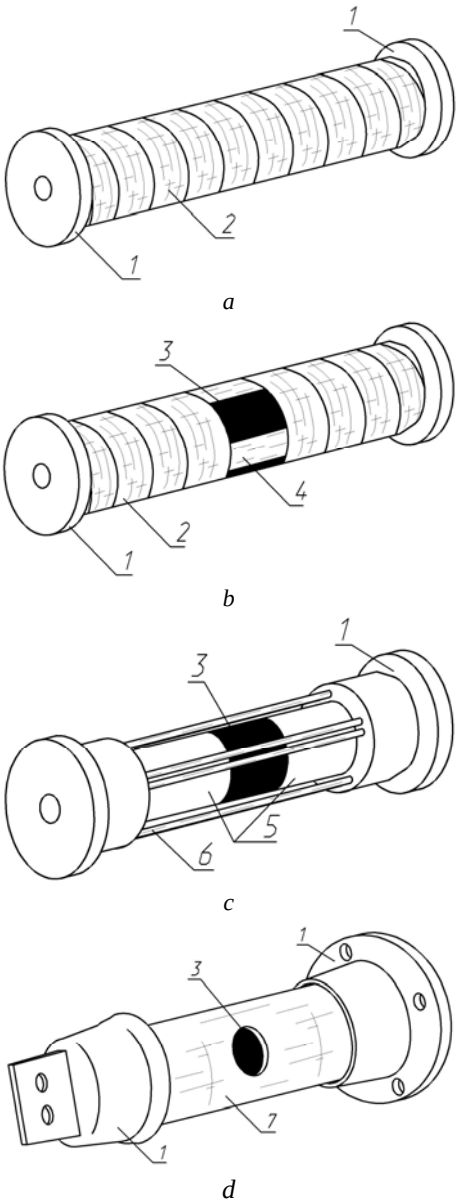

Fig. 1. Column sketches: *a* – with winding; *b* – with winding and with a hole; *c* – with rods; *d* – with a pipe and two holes (1 – aluminum flange, 2 – hardened fiberglass tape, 3 – metal oxide varistor, 4 – longitudinally positioned glass band tape, 5 – aluminum inserts, 6 – fiberglass rod, 7 – fiberglass pipe with holes)

A technique of testing for explosion safety. Tests for explosion safety of surge suppressors were carried out on the basis of the Slavyansk traction substation according to the program agreed with the JSC «Ukrainian Railways». The electrical circuit of tests is shown in Fig. 2.

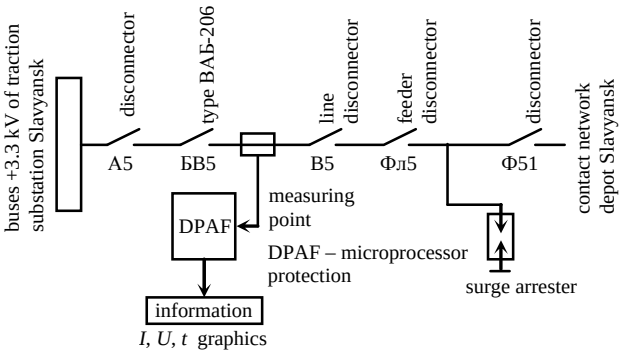

Fig. 2. Electrical circuit of testing sections of the SAp on the traction substation of Slavyansk city

The sample of the surge arrester was mounted on one of the metal poles at height of 5.5 m located on the territory of the substation and connected to the traction substation buses of 3.3 kV via disconnectors A5, B5, Фл5 and high-speed circuit breaker ВАБ-206 (Fig. 3).

Fig. 3. Sample of SAp prepared for testing

The test circuit was separated from the contact network by a Ф51 disconnector. After the ВАБ-206 circuit breaker was closed, a short circuit current flowed through a column with a experienced preliminary breakdown or shunted by a copper wire varistor with the formation of an electric arc inside the SAp section.

The process associated with the flow of short-circuit current was monitored using the control complex of the digital protection and automation of feeder (DPAF) 3.3, the instantaneous values of the current and voltage in the circuit were recorded and current and voltage oscillograms through the arc were recorded.

During the tests, samples were video-recorded using a DVR installed in close proximity to the sample under test. After the tests, each SAp sample was inspected, the samples were photographed, the weight of the sample was determined after the tests and, if the shell ruptured, the dispersion of the SAp fragments was evaluated.

Figure 4 shows the oscillogram of current and voltage at the moment of arc discharge inside the case of the sample No. 2.

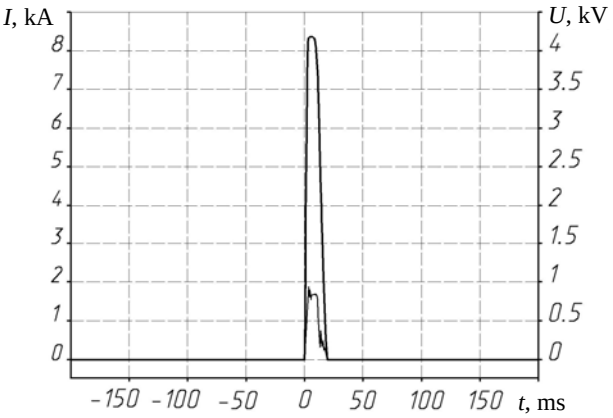

Fig. 4. Oscillogram of current and voltage at the moment of arc discharge inside sample case No. 2: a high peak corresponds to the arc current; lower peak – to voltage; abscissa – time in ms

The test results for SAp-3.3 kV for explosion safety are presented in Table 1.

For the evaluation of explosion safety of the SA, the Standard [4] establishes the following criteria:

1. A surge arrester is considered to be explosion-proof if fragments of a structure that fell to the ground after the destruction of the SA are left in a circle with a diameter of not more than $D = 1.2 \cdot (2 \cdot H_{sa} + D_{sa})$, where H_{sa}, D_{sa} are the height and diameter of the Sa, respectively; for devices of small height, it is assumed that $D = 1.8$ m.

2. It is considered permissible to depart from a circle of fragments of a damaged structure weighing up to 60 g each.

The area of hot gases coming from the SA is not standardized.

Additionally, we note that if, as indicated in [7-11], the electric arc from the SA case will come out, then explosive destruction will not occur over the entire period of arc burning. However, if the arc remains inside the case, explosion proof cannot be guaranteed.

From Table 1 it follows that of the 8 tested structures in 7 cases, the destruction of the case occurred without scattering of the fragments. In the area of placement of the varistor, there was a local break of the silicone shell with the release of gas and exit to the outside of the arc discharge. The exception was sample No. 2, in which, during an explosion, the upper electrode was broken out with simultaneous scattering of fragments of a split varistor within a radius of 3-5 m.

Analysis of research results.

1. From Table 1 it is seen that from 8 tested structures in 7 cases the destruction of the case occurred without scattering of the fragments. In 7 samples, in the zone of the varistor placement, there was a local break of the silicone shell with the release of gas and exit of the arc discharge. The exception was sample No. 2, which was made by continuous winding of the frame with a glass banding tape, which had a tearing out of the upper electrode during the explosion and simultaneous scattering of fragments of a split varistor within a radius of 3-5 m. Because of the white smoke accompanying the explosion, it was failed to record on the frame whether the arc exit from the case to the outside, despite the fact that in the next frame (after 33 ms) the arc was no longer recorded.

Table 1

Test results of SAp-3.3 kV for explosion safety

SA No.	short-circuit current through SA (A); maximum voltage fixed by DPAF (V); full time of the short circuit switching off (s)	Type of damage to the case	Varistor state after testing	State of aluminum liners adjacent to varistors
1	I = 8130; U = 800; t = 0.02	Shell rupture in the varistor placement zone without fragmentation	Varistor cracking	Deep erosion of aluminum liners in the zone of cracks in the varistor
2	I = 7178; U = 1120; t = 0.02	Tearing the top electrode; destruction and expansion of varistor fragments for 3-5 m	Varistor cracking	Erosion of aluminum liners in the zone of cracks in the varistor
3	I = 8640; U = 800; t = 0.02	Shell rupture in the varistor placement area without fragmentation	Varistor cracking	Erosion of aluminum liners in the zone of cracks in the varistor
4	I = 7890; U = 1000; t = 0.02	The rupture of the shell in the zone of placement of the weakened place in the winding of glass band tape	Varistor, shunted by copper wire, without destruction	Erosion of aluminum liners in the zone of copper wire
5	I = 7245; U = 800; t = 0.02	2 tears and 3 shell punctures	Varistor, shunted by copper wire, without destruction	Erosion of aluminum liners in the zone of copper wire
6	I = 8153; U = 800; t = 0.02	8 point punctures	Varistor, shunted by copper wire, without destruction	Erosion of aluminum liners in the zone of copper wire
7	I = 7238; U = 900; t = 0.02	Shell rupture in the varistor placement area without fragmentation	Varistor cracking	Erosion of aluminum liners in the zone of cracks in the varistor
8	I = 7890; U = 1000; t = 0.02	The rupture of the shell in the zone of the location of the round hole in the fiberglass pipe, glue-threaded connection of aluminum flanges with fiberglass pipe is not broken	Varistor, shunted by copper wire, without destruction	Erosion of aluminum liners in the zone of copper wire

2. In two other samples No. 1 and No. 3, made similarly by a continuous winding with a glass banding tape, a local gap of the frame and the silicone coating was observed with the arc going out. Scattering of dangerous fragments was absent. In about 100 ms, the electric arc reached the surface was completely extinguished, this can be seen on the freeze frames received every 33 ms (Fig. 5). For the remaining 5 samples, the observed arc burning pattern was similar, as for samples No. 1 and No. 3 (Fig. 5).

3. When testing the 8 presented structures, in none of them the case did not ignite.

4. If the tests were carried out on SAp, assembled with experienced preliminary breakdown varistors (electrothermal breakdown), the varistors during the tests broke apart, remaining inside the frame (except sample No. 3). From the action of the arc in the zone of contact between aluminum electrodes and varistors, a deep burnout of the electrodes was observed; in some cases the burnup was up to 7 mm deep and up to 8 mm wide.

5. If the varistors were shunted with copper wire, they remained intact, while melting and burning out part of the aluminum electrodes also occurred in the zone of connection with the copper wire, but in smaller sizes.

arc in 33 ms | arc in 66 ms | arc in 99 ms | sample No. 1 after voltage off

Fig. 5. Freeze frames of the arc exit from the SAp case after ВАБ-206 switching on

Conclusions.

1. Conducted tests of polymer samples of SAp-3.3 kV under operating conditions on the equipment of the operating substation, with short circuit currents of 8.3 kA and current exposure time of 0.02 s, close in value to ones recommended by IEC 60099-4:2014 Standard, showed quite satisfactory ability to withstand large pulse short-circuit currents without scattering fragments dangerous to personnel and the surrounding equipment.

2. Polymer structures, the frame of which is made of continuous winding, require strengthening the zone of connection between the frame and the electrodes. For

such structures, it is required to introduce an additional test for mechanical strength in the longitudinal direction with a predetermined strength limit into the acceptance test program of the SAp.

REFERENCES

1. Radchenko V.D. *Tekhnika vysokikh napriazhenii ustroistv elektricheskoi tiagi* [High voltage technique for electric traction devices]. Moscow, Transport Publ., 1975. 359 p. (Rus).

2. Grubar L.O, Pertsovskiy L.M, Trofimov V.I. *Ustroistvo, montazh i ekspluatatsiia tiagovykh podstantsii* [Design, installation and operation of traction substations]. Moscow, Transport Publ., 1971. 359 p. (Rus).

3. Radchenko V.D, Farafonov A.V. *Vysokovol'tnye apparaty zashchity postoiannogo toka* [DC high voltage protection devices]. Moscow, Transport Publ., 1971. 142 p. (Rus).

4. *IEC 60099-4. Ed.3.0 b: 2014.* Surge arresters – part 4: Metal-oxide surge arresters without gaps a.c. systems. 2014. 168 p.

5. *GOST R 55167-2012. Ogranichiteli perenapryajeniy nelineynyie dlya tyagovoy seti zheleznyh dorog. Obschie tehnicheskie usloviya*. [GOST R 55167-2012. Surge arresters for power supply systems of electrified railways. General specifications]. Moscow, Standartinform Publ., 2013. 15 p. (Rus).

6. *GOST 12.2.007.0-75. Sistema standartov bezopasnosti truda. Izdeliya ehlektrotekhnicheskie. Obshchie trebovaniya bezopasnosti* [GOST 12.2.007.0-75. Occupation safety standards system. Electrical equipment. General safety requirements]. Moscow, Standartinform Publ., 2008. 10 p. (Rus).

7. Golubev P., Dmitriev V., Dmitriev M. Questions of the choice of the current explosion hazard of surge arresters 6-750 kV. *Electrical engineering news*, 2009, no.4(58). Available at: http://www.news.elteh.ru/arh/2009/58/13.php (Accessed 22 September 2017). (Rus).

8. Kapustin D. Pressure relief device in surge arrester. Test statistics. *Electrical engineering news*, 2004, no.1(25). Available at: http://www.news.elteh.ru/arh/2004/25/06.php (Accessed 08 May 2017). (Rus).

9. Bernhard A., Shmidt W. Surge arrester configuration with direct on moulded silicone insulation. *Proceedings of World conference and exhibition on insulators, arresters and bushings: optimizing reliability, availability and cost through optimal selection of these components*. Spain, 2003, pp. 97-106.

10. Hinrichen V. Latest designs and service experience with station-class polymer housed surge arresters. *Proceedings of World conference and exhibition on insulators, arresters and bushings: optimizing reliability, availability and cost through optimal selection of these components*. Spain, 2003, pp. 85-96.

11. Steinfeld K. Design of metal-oxide surge arresters. *Proceedings of World conference and Exhibition on insulators, arresters and bushings: optimizing reliability, availability and cost through optimal selection of these components*. Spain, 2003. pp. 137-146.

Received 01.10.2018

Yu.N. Shumilov[1], *Doctor of Technical Science, Professor,*
V.I. Bondarenko[2], *Candidate of Technical Science, Associate Professor,*
[1] PSC «Slavyansk High Voltage Insulators Works»,
79, Kramatorskaya Str., Slavyansk, Donetsk Reg., 84105, Ukraine,
phone +380 95 1813515, e-mail: sumilovurij2@gmail.com
[2] Donbass State Pedagogical University,
19, G. Batyuka Str., Slavyansk, Donetsk Reg., 84116, Ukraine,
phone+380 50 9084005, e-mail: nv1287@ukr.net

How to cite this article:
Shumilov Yu.N., Bondarenko V.I. Investigation of explosion safety of DC polymer surge arresters 3.3 kV for traction network of railway transport. *Electrical engineering & electromechanics*, 2019, no.2, pp. 66-70. **doi: 10.20998/2074-272X.2019.2.10.**

Матеріали приймаються за адресою:
Кафедра "Електричні апарати", НТУ "ХПИ", вул. Кирпичова, 21, м. Харків, 61002, Україна
Електронні варіанти матеріалів по e-mail: a.m.grechko@gmail.com

Довідки за телефонами: +38 050 653 49 82 Клименко Борис Володимирович
+38 067 359 46 96 Гречко Олександр Михайлович

Передплатний індекс: 01216